

Experimental Demonstration and System Analysis for Plasmonic Force Propulsion

NASA Innovative Advanced Concepts
Phase II Final Report
Grant Number NNX16AL26G

September 27th, 2019

By:

PI: Joshua L. Rovey
University of Illinois at Urbana-Champaign
104 S. Wright St., 317 Talbot Lab
Urbana, Illinois 61801
rovey@illinois.edu 217-300-7092

Co-I's: Jie Gao, Henry Pernicka, Xiaodong Yang
Graduate Students/Post-docs: P. Galchenko, J. Maser, W. Liu
Missouri University of Science and Technology
Rolla, Missouri 65409

Executive Summary

This project developed a higher-fidelity model of a recently envisioned small spacecraft propulsion system for precision pointing and proximity control. Plasmonic force propulsion harnesses solar light focused onto plasmon reactive subwavelength nanostructures to accelerate and expel nanoparticle propellant via strong optical forces. The goal of the project was to show that plasmonic space propulsion can provide the level of proximity and attitude control envisioned for future NASA nano/picosatellite missions, a level that is better than state-of-the-art approaches. We achieved this goal by showing that plasmonic force thrusters are feasible for a range of advanced mission concepts requiring swarm formations in a deep space environment. We performed three case studies that evaluated the performance of the plasmonic force propulsion thruster in a deep space, microsatellite swarm formation. These case studies assumed the propulsion system could generate thrust at the level predicted from our Phase 1 study (1.6 μN). Through these cases we were able to analyze the concept within a mission specific context through detailed orbital dynamics calculations. Results indicate that, with the Phase 1 estimated thrust level, the approach is promising for providing attitude control to swarm formation spacecraft.

Further, we achieved goals related to technology development. Specifically, we experimentally demonstrated nanoparticle acceleration due to plasmonic forces with asymmetric nanostructures excited by focused *laser* light. Additionally, we investigated the thrust sensitivity and nanoparticle propellant injection dependencies upon thermal effects. As a result of our study, plasmonic force propulsion is at an early TRL 3. Active research and design has been conducted analytically and in the laboratory. Furthermore, practical applications such as the three case studies have been identified for the scientific basic principles that were observed. Future efforts related to fundamental understanding of these techniques should focus on 1) developing a standalone array

of asymmetric nanostructures that can effectively interact with a stream or reservoir of particles or 2) experimentally evaluate a dielectrophoretic injector for nanoparticle propellant.

The main limitation discovered about plasmonic propulsion regards performance estimates significantly below the Phase 1 estimations. Specifically, original assumptions in the Phase 1 project (notably, a linear array of asymmetric nanostructures) is not a viable approach to achieving significant acceleration, high exhaust velocity, of nanoparticles. More specifically, we assumed in Phase 1 that nanoparticles would be accelerated in series by a long linear array of asymmetric nanostructures. That is, the acceleration of the nanoparticle would build and increase with the kick received by each subsequent nanostructure. This is fundamentally flawed. The potential profile of a single nanostructure is such that it prohibits this phenomenon. The potential energy associated with the plasmon-generated dielectrophoretic force is a potential well, which is good for trapping nanoparticles, but cannot provide significant acceleration of particles to expel them out and away from the nanostructure. Further, a nanoparticle expelled from the first nanostructure would need to overcome the potential barrier for entry into the next nanostructure accelerating stage. Fundamentally, this effect means that a linear array of nanostructures is not a viable accelerating structure. Correspondingly then, acceleration can, or should, only be provided by one nanostructure, and the net acceleration and thrust force of a single nanostructure is small (\sim cm/s exhaust velocities, sub-nN level thrust vs. the 100's m/s, μ N originally envisioned). While our experiments demonstrated acceleration and manipulation of a nanoparticle using laser light in aqueous environment, the achievable energy and momentum addition to the nanoparticle from a single nanostructure stage is too low for useful propulsion. In terms of thrust prediction, the estimated thrust of 1.6 μ N in Phase 1 is reduced to a few nN of thrust with this new insight and understanding of the concept. This thrust level is too small to achieve attitude control of swarms as originally envisioned.

Table of Contents

Executive Summary.....	i
Table of Contents.....	iii
1 Introduction.....	1
1.1 The concept.....	1
1.2 Motivation.....	2
1.3 Goal, Objectives, and Approach of the Study.....	3
2 Results of the Study.....	4
2.1 Specific Objective 1: Comparison of Experimentally Measured and Numerically Predicted Plasmonic Force on a Nanoparticle	4
2.1.1 Fabrication and measurement of asymmetric nanostructures for plasmonic propulsion	4
2.1.2 Building optical tweezers setup based on a microscope for particle trapping and transport	8
2.1.3 Demonstration of optical transport of particles by 3D Weber beams	9
2.1.4 Demonstration of optical transport of particles by using 3D cusp beams	14
2.1.5 Experimental observation of the plasmonic force propulsion of particles	17
2.2 Specific Objective 2: Off-axis Illumination and Equilibrium Temperature of the Nanostructures	20
2.2.1 Thermal stability.....	20
2.2.2 Electromagnetic response for different materials.....	22
2.3 Specific Objective 3: Nanoparticle Propellant Injection using the Dielectrophoretic Forcing	26
2.3.1 Theory of dielectrophoresis.....	27
2.3.2 Dielectrophoretic injector design.....	28
2.3.3 Parametric analysis of the dielectrophoretic injector	33
2.3.4 Finite Element Analysis.....	36
2.3.5 Particle dynamics in the DEP injector.....	38
2.3.6 DEP Injector Conclusions	42
2.4 Specific Objective 4: Precision Pointing Capabilities Applied to the Control of Microsatellite Swarms	42
3 Conclusions.....	43
4 Future Work	43
5 List of Publications Related to this Work	44
5.1 Journal.....	44
5.2 Conference	44

6	References	44
	Appendix: Specific Objective 4.....	47

1 Introduction

1.1 The concept

The surface electrons in a metal oscillate when optical radiation strikes the surface of the metal. A group of oscillating electrons is known as a plasmon. When the metal is reduced in dimensions to the nanoscale regime, the plasmon oscillation length becomes comparable to the nanostructure length-scale, and the plasmons are able to resonate with the incident radiation. This resonance creates an intense, localized electromagnetic field distributed about the region of the nanostructure. The electromagnetic field can be tuned by changing the size and shape of the metallic nanostructures and used to control the motion of particles within the vicinity of the nanostructure. The nanoparticle manipulation and acceleration enabled by the enhanced plasmonic forces is well-known and often referred to as “optical tweezers.”¹ These plasmon-generated forces have been demonstrated to optically trap particles beyond the diffraction limit.

Our research extends this idea of plasmonic nanoparticle manipulation from trapping to acceleration and is specifically aimed at propulsion for small (nano, pico) satellites. Our work focuses on harnessing the nanoscale light-metal interaction for net-neutral nanoparticle acceleration.

In the particle trapping experiments of the “plasmon nano-optical tweezers,” symmetric nanostructures are employed² because they create symmetric trapping volumes, or potential wells. Therefore, in order to create an asymmetric potential and strong particle acceleration, we investigate asymmetric nanostructures. An asymmetric, V-groove type structure was developed by Shalin and Sukhov in 2012³ for the one dimensional acceleration and ejection of nanoparticles out of V-shaped grooves in a nanocannon fashion. They propose that ejection of nanoparticles from the V-shaped grooves will occur due to the gradient force of the E -field in the grooves and a negative real part of the polarizability of the nanoparticles. They estimated particle velocities on the order of 1 m/s with optical excitation between 300 – 400 nm.⁴ Our asymmetric nanostructures are grouped by two’s into a nano-unit as shown in Figure 1 (a). They resonate with a small, tunable range of incident light that is polarized perpendicularly to their nanoparticle acceleration axis, along the width of the nano-unit. We have found that the asymmetric, trapezoidal nanostructures resonate strongly within the visible spectrum at a wavelength of $\lambda = 770$ nm when dimensions are $w = 110$ nm, $l = 400$ nm, and $g = 30$ nm.⁵

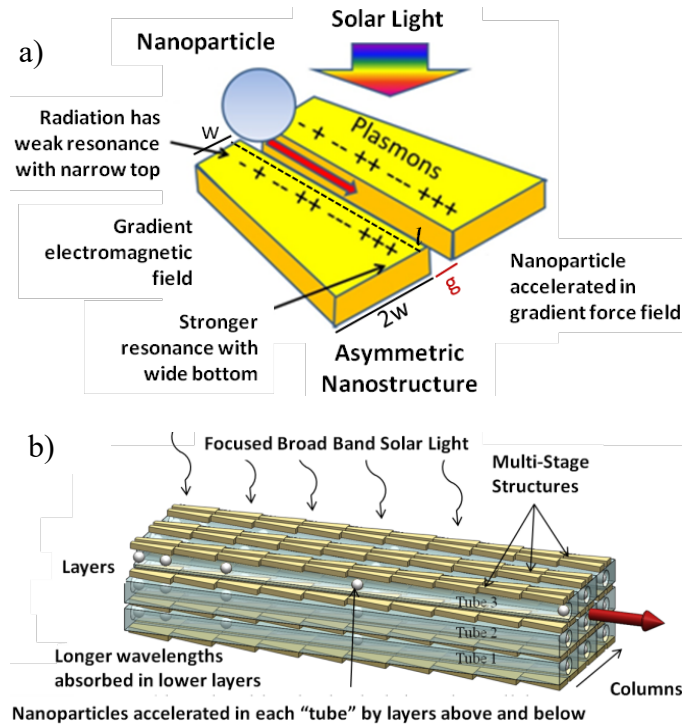


Figure 1: Plasmon force propulsion concept

A schematic of the relevant plasmonic physics and how it might be employed for propulsion is shown in Figure 1 (b). Sunlight is directly focused onto subwavelength metallic nanostructures through a lens (not shown). The resonant interaction and coupling of the light with the nanostructures excite surface plasmon polaritons that generate a strong gradient optical force field. Nanoparticles (e.g., glass beads) are accelerated by the gradient force field and are expelled. Because the optical force field is coupled to the nanostructure through the strong light-matter interaction with surface plasmon polaritons, thrust is generated through momentum exchange with the expelled particles.

Careful examination of Figure 1 (b) reveals a major benefit of plasmonic propulsion: little to no electric or spacecraft power is required. Solar energy is directly converted into propulsive thrust, additional solar cells, batteries, or other energy storage is not required. This has distinct advantages for the mass and power budget of a spacecraft, especially small satellites where mass and power are already severely limited. However, unlike other direct energy conversion propulsion technologies, plasmonic propulsion is not due to photon pressure, but rather the strong gradient optical force field generated by surface plasmon polaritons excited in the designed metallic nanostructures by the strongly resonant light-matter interaction.

1.2 Motivation

Nanosatellites are defined as spacecraft with a mass of 1-10 kg. The demand for and use of these and other small satellites is widespread and is projected to continue increasing according to numerous SpaceWorks reports on the nano/microsatellite market ^{6,7,8}. The 2018 SpaceWorks report ⁷ also makes note that most nano/microsatellites are launched in large clusters and that large constellations of small satellites for communications/observations purposes will make up ~70 % of the market over the next five years. Satellites within sizeable constellations will need the ability

to maneuver and orient themselves precisely in relation to the other satellites of the cluster. In spite of the intense and exploding interest in small spacecraft, their full potential remains untapped because they lack maneuverability. The major challenge remains propulsion. Micci and Ketsdever⁹ compiled micropropulsion state-of-the-art in 2000 and many of those micropropulsion systems have been or are being investigated for small spacecraft (e.g., microresistojets, microcavity discharge thrusters, mini ion/Hall, pulsed plasma thrusters, and electrospray MEMS). New concepts have also been investigated (e.g., nanoparticle field extraction, laser ablation, free molecule resistojets). While significant advances have been made, small spacecraft still lack propulsion for the same reasons outlined by Micci and Ketsdever: mass, power, and volume constraints. The need remains for a propulsion system that can fit on ever-shrinking small satellite platforms. We investigate the feasibility of a plasmonic force propulsion system to fit this niche.

Plasmonic force propulsion provides attitude control capability for small spacecraft with no power penalty and minimal mass and volume penalty. This creates new capabilities for small spacecraft enabling NASA science and exploration missions that were previously impossible. Examples of new capabilities of small spacecraft include precise orientation for imaging, sample collection, and/or data collection, alignment of spacecraft clusters/formations, orbit adjustment/control around asymmetric bodies (e.g., asteroids), at Lagrange points, and at inter-space staging locations.

One of NASA's strategic goals is expanding scientific understanding of the Earth and the universe.¹⁰ One specific mission related to that goal and enabled by the concept is detailed asteroid mapping. A small satellite (e.g., cubesat) deployed from a mother satellite could use its plasmonic force propulsion system to orbit the asteroid investigating its 3D shape, composition, rotation, etc., information that can elucidate the early solar system and potential for asteroid mining. Another NASA goal is to identify and investigate exoplanets, planets outside our solar system.¹⁰ The measurements necessary to study exoplanets are quite challenging and require extremely sensitive instruments that must be precisely pointed at the region of interest. The Astrophysics Strategic Mission Concept Studies most stringent requirement is 0.1 milliarcseconds for the ACCESS mission¹¹, which is 50 times more precise than the state-of-the-art 5 milliarcseconds for Hubble. The proposed plasmonic propulsion concept can enable and enhance these types of missions by providing very small thrust and impulse bits to precisely orient a spacecraft or align a constellation of satellites.

Nanoparticle manipulation using strong optical forces generated by surface plasmon polaritons is well-known within the plasmonics community. Ushering this widely accepted concept into the realm of spacecraft propulsion will break new ground because it is the first investigation of plasmonic forces generated directly from sun light to control small satellites with high precision. Our study investigates the gradient plasmonic force which provides a new concept to manipulate nanoparticles with tapered metallic nanostructures excited by sun light.

1.3 Goal, Objectives, and Approach of the Study

The **goal** of our study is to show that plasmonic space propulsion can provide the level of proximity and attitude control envisioned for future NASA nano/picosatellite missions, a level that is better than state-of-the-art approaches. Our **objective** is to compare higher fidelity proximity/translational and attitude control predictions for plasmonic space propulsion with state-of-the-art approaches. Our **specific objectives** are to (1) compare the experimentally measured plasmonic force on a nanoparticle with numerical predictions, (2) analyze the effect of Earth shadow and off-axis illumination on thrust capability, (3) quantify and explore the nanoparticle

propellant injection technology of dielectrophoretic forcing through a porous membrane including power requirements, nanoparticle concentration manipulation, and corresponding nanoparticle injection rate, (4) evaluate the effects of thrust noise, throttleability, plasmonic sensitivity, and thermal effects on precision pointing capability, and (5) create a technology development roadmap.

2 Results of the Study

In the following sections we present results from experimental procedures of plasmonic force fields, propulsion robustness evaluations, propellant transport properties, and mission specific case studies with orbital dynamics calculations. Additionally, we expand upon the conceptual design of a plasmonic force propulsion thruster and related concepts.

2.1 Specific Objective 1: Comparison of Experimentally Measured and Numerically Predicted Plasmonic Force on a Nanoparticle

2.1.1 Fabrication and measurement of asymmetric nanostructures for plasmonic propulsion

We have worked on the fabrication process of plasmonic nanostructures, which will be used for accelerating and expelling nanoparticles in aqueous solution. At first, symmetric plasmonic nanostructure arrays with straight bars and holes are fabricated. The fabrication process includes the following steps. A 50 nm thick gold film is deposited on a quartz substrate using the electron-beam evaporation process. Then a focused ion beam is used to directly etch into the gold film to form the designed plasmonic nanostructure pattern array. After several rounds of fabrication and optimization, high quality nanoscale plasmonic nanostructure arrays can be fabricated. Figure 2 (a) shows a scanning electron microscope (SEM) image of the fabricated plasmonic straight bar array, with the bar dimensions of 75 nm by 230 nm and period of 410 nm. It shows that the etched area around the straight bar pattern is quite clean and a uniform bar array has been achieved. Figure 1(b) shows an SEM image of the fabricated plasmonic hole array, with hole dimensions of 50 nm by 205 nm and period of 330 nm. The hole array has been etched sharply with great uniformity. These results demonstrate that we have successfully developed the capability to fabricate plasmonic nanostructures for both positive and negative patterns with high quality features down to 50 nm size.

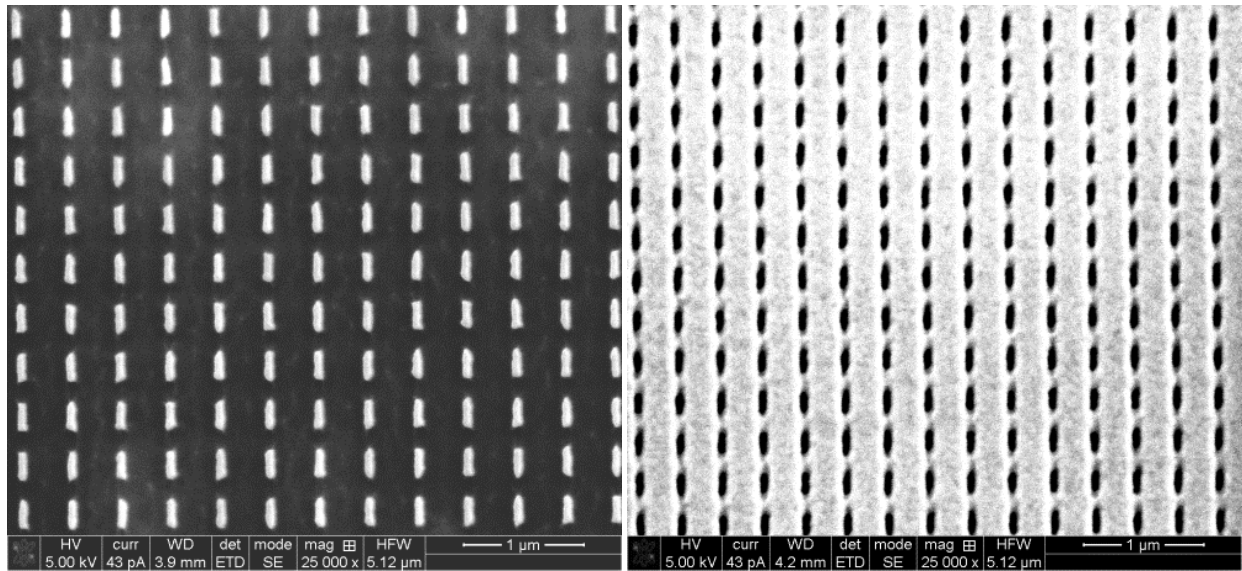


Figure 2: SEM images of the fabricated (a) plasmonic straight bar array and (b) plasmonic hole array on 50 nm thick gold film deposited on quartz substrate.

We also measured the optical transmission spectrum through the fabricated plasmonic straight bar array with our previously developed spectrum measurement setup. A white light source is used to provide broadband excitation covering the whole solar spectrum. The fabricated samples mounted on a microscope will be excited by the white light through a microscope. The optical transmission through the samples is then coupled out from the microscope and collected by a spectrometer for the optical transmission spectrum analysis. Figure 3 shows our measured optical transmission spectrum for the bar array sample from the wavelength range of 500 nm to 900 nm. It is shown that there is a strong plasmonic resonance mode around 850 nm. The numerically simulated transmission spectrum matches the measured data well.

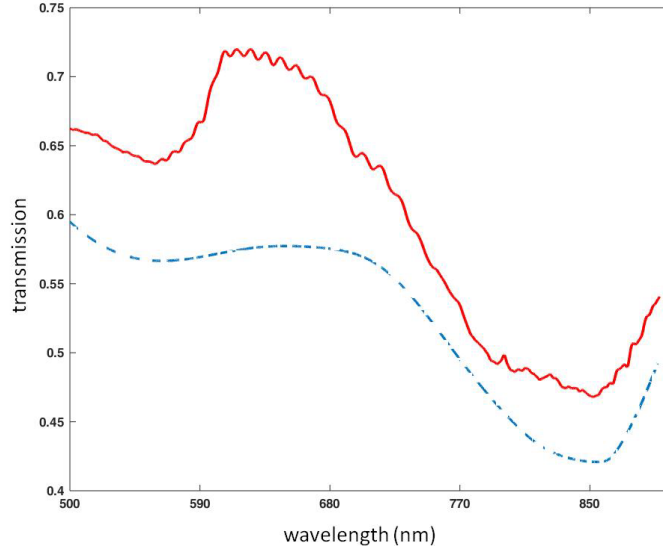


Figure 3: The measured optical transmission spectrum for the plasmonic bar array sample. Solid red curve is for measurement and dashed blue curve is for simulation.

With the successful fabrication and measurement of symmetric plasmonic nanostructure arrays with straight bars and holes in gold film, we then fabricated and optimized the designed asymmetric plasmonic nanostructures, which will be used for accelerating and expelling nanoparticles in aqueous solution. We also characterized optical and physical properties of the fabricated samples. The fabrication process includes the following steps. A 50 nm thick gold film is deposited on a quartz substrate using the electron-beam evaporation process. Then a focused ion beam is used to directly etch into the gold film to form the designed plasmonic nanostructure pattern array. By optimizing the fabrication process, high-quality asymmetric plasmonic nanostructure arrays are fabricated.

Figure 4 (a) presents our design of asymmetric plasmonic nanostructures with trapezoid-cut geometry. One SEM image of the fabricated plasmonic trapezoid-cut array is shown with gap size of 50 nm and period of 625 nm. The fabrication process has been greatly improved and it is shown that the trapezoid-cut array has been etched through the gold thin film with smooth side walls. It also shows that the etched area around the trapezoid-cut pattern is quite clean and uniform trapezoid-cut array has been achieved. The high-quality asymmetric trapezoid-cut patterns will produce strong gradient optical fields for plasmonic propulsion application. We also measured the optical transmission spectrum through the fabricated plasmonic trapezoid-cut array with our developed spectrum measurement setup. Figure 4 (b) shows our measured optical transmission spectrum for the trapezoid-cut array sample from the wavelength range of 450 nm to 950 nm for horizontal polarization. It is shown that there is a strong plasmonic resonance mode around 825 nm. The numerically simulated transmission spectrum matches the measured data very well.

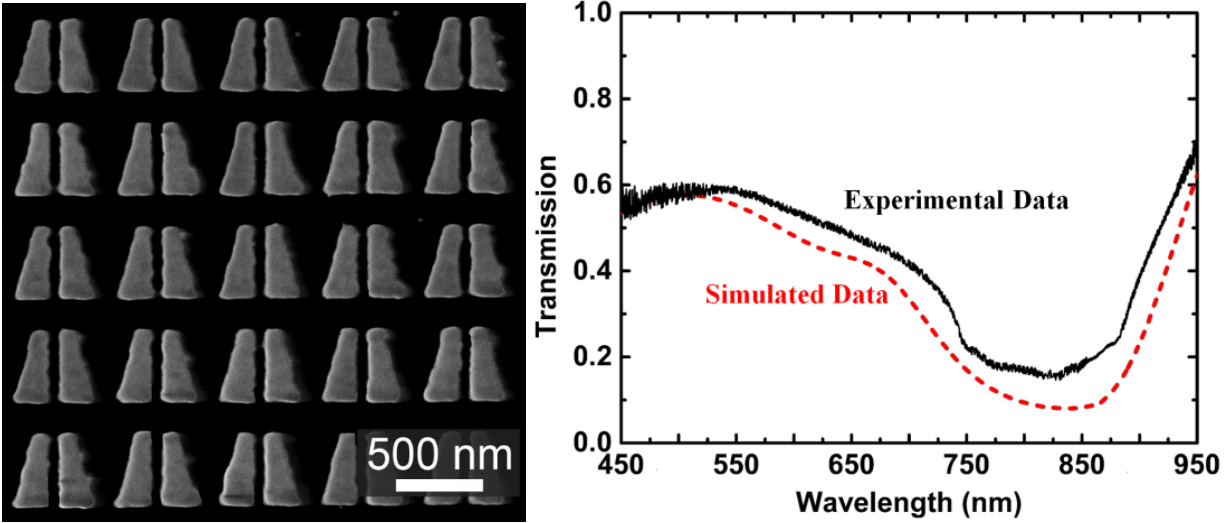


Figure 4: (a) SEM images of the fabricated asymmetric plasmonic trapezoid-cut array in a 50 nm thick gold film deposited on a quartz substrate. (b) The simulated and measured optical transmission spectrum for the plasmonic trapezoid-cut array sample.

Figure 5 (a) shows another design of asymmetric plasmonic nanostructures, the triangle-hole array. One SEM image of the fabricated plasmonic triangle-hole array is given with side-wall dimension of 145 nm and period of 290 nm. The triangle-hole array has been etched through the gold thin film with good quality. The asymmetric triangle-hole negative patterns will provide strong gradient optical fields for plasmonic propulsion. The optical transmission through the sample is further measured by a spectrometer for the optical transmission spectrum analysis. Figure 5 (b) shows the measured optical transmission spectrum for the plasmonic triangle-hole array sample from the wavelength range of 500 nm to 1000 nm, where horizontal polarization is used to excite the structures. A strong plasmonic resonance mode around the visible wavelength of 600 nm is observed in the experimentally obtained data. The simulated plasmonic resonance is located around 650 nm. By scaling the triangle-hole sizes, the plasmonic resonance wavelength can be further adjusted to cover the whole solar light spectrum. With the fabricated asymmetric plasmonic nanostructures, plasmonic force propulsion effects acting on particles in aqueous solution will be further studied.

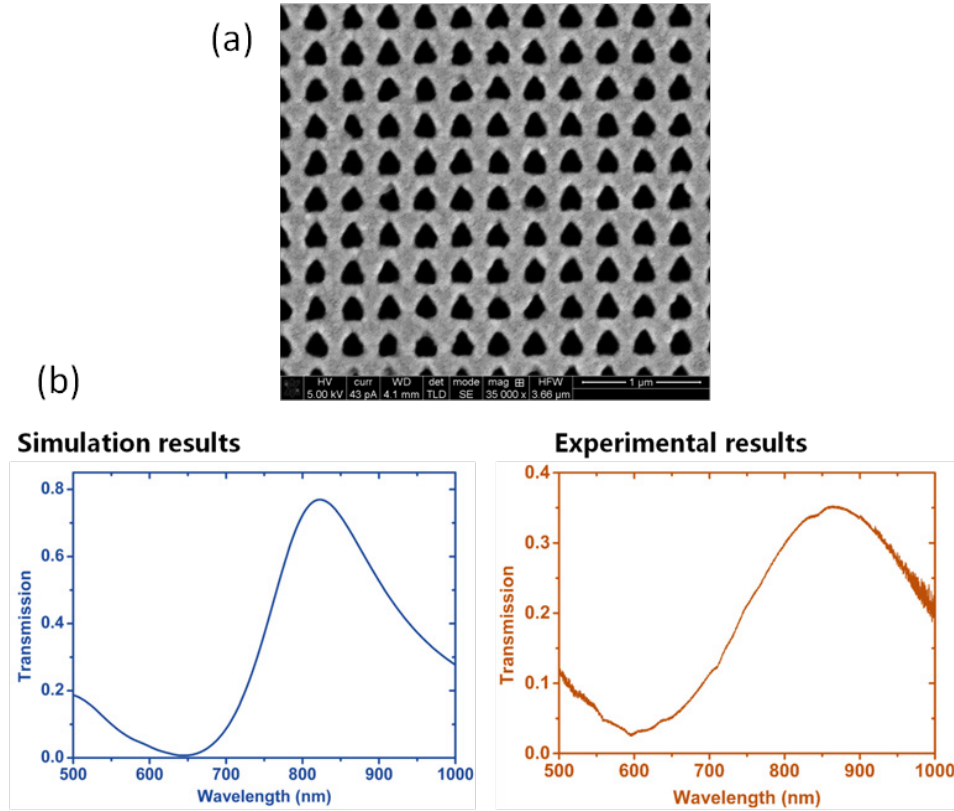


Figure 5: (a) SEM images of the fabricated asymmetric plasmonic triangle-hole array in a 50 nm thick gold film deposited on a quartz substrate. (b) The simulated and measured optical transmission spectrum for the plasmonic triangle-hole array sample.

2.1.2 Building optical tweezers setup based on a microscope for particle trapping and transport

The optical force field produced by asymmetric plasmonic nanostructures for accelerating and expelling nanoparticles will be investigated with an optical tweezer setup for trapping and transporting nanoparticles in aqueous solution. Before we test the asymmetric plasmonic nanostructure samples, the optical trapping and the optical transport of particles by using 3D optical beams are demonstrated. Figure 6 gives our optical setup for particle trapping and transport in aqueous solution. The 532 nm laser is expanded and modulated by a spatial light modulator (SLM) for generating the desired 3D optical beam, and the 3D beam is focused by the microscope objective lens into the water chamber to trap and transport the 3 μm-diameter polystyrene spherical particles. The SLM is programmed by a computer to modulate the input laser light into the 3D Weber beam or the 3D cusp beam. Other 3D beams can also be generated using SLM. Here, Weber beam and cusp beam are just two examples for us to demonstrate our capability to trap and transport particles. With the illumination of a white light lamp, the CCD camera on the microscope is used to observe and record the motion and trapping scene of polystyrene spherical particles in the water chamber.

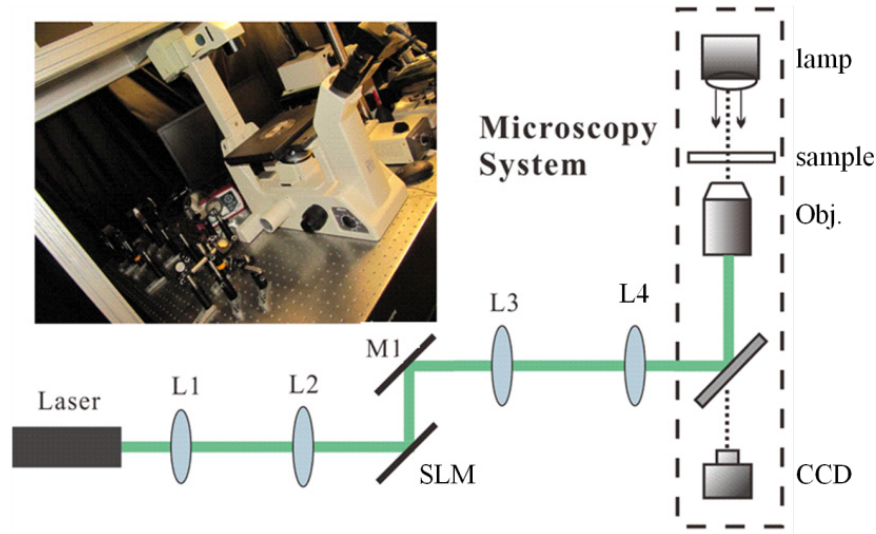


Figure 6: Our optical tweezer setup based on a microscope for particle trapping and transport.

Figure 7 shows the CCD images of the particle trapping. One $3\mu\text{m}$ -diameter polystyrene spherical bead is stably trapped with the focused 532nm laser beam. With the bright illumination of a white light lamp, we use the CCD camera on the microscope to observe and record the motion of the polystyrene bead. From Figure 7 (a), we can see that one polystyrene bead is trapped by the laser beam (cross mark), while an untrapped reference polystyrene bead is also shown (circle mark) in the same CCD image view. In Figure 7 (b), we then move the stage of water chamber along the black arrow direction, the trapped bead stays in the same location but the untrapped reference bead is shifted away from its original position. In Figure 7 (c), we move the stage even faster, and the trapped bead is released from the optical trap.

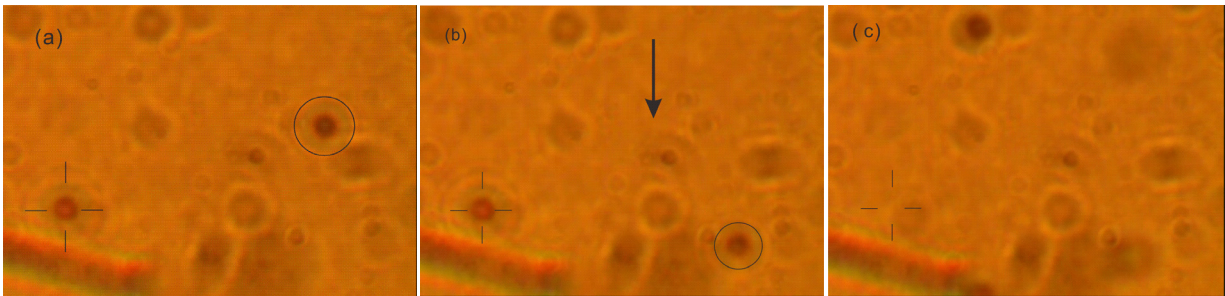


Figure 7: Optical trapping of $3\mu\text{m}$ polystyrene bead by the 532nm laser beam.

2.1.3 Demonstration of optical transport of particles by 3D Weber beams

Before we test the asymmetric plasmonic nanostructure samples, the optical transport of particles by using 3D non-diffracting Weber beams are demonstrated. We present the optical transportation of solid polystyrene particles along the main lobes of the non-diffracting Weber beams with different parabolic shapes. The Weber beams are generated from the complex field modulation based on the spatial light modulator (SLM) in the optical tweezer setup. It is shown that there exists an array of in-line vortices in the phase profile of the Weber beam, and the beam

energy flow presents an interesting parabolic twisting behavior for transporting micro-particles along different parabolic tracks. In the experiment, the solid particle size is larger than the laser wavelength and the particles are driven by the Weber beams in 3D motion. The motion and velocity of particles are recorded and analyzed along the beam parabolic main lobe in the transverse dimension, in order to demonstrate the special transportation functionality of the Weber beams for micro-particles under the joint action of scattering force and gradient force.

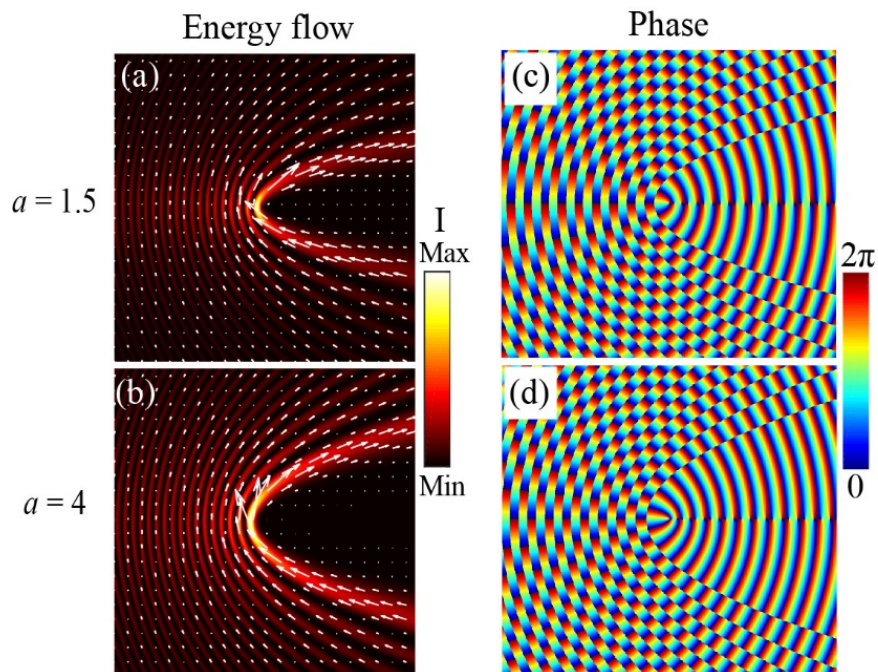


Figure 8: (a, b) Transverse intensity (color map), energy flow (white arrows), and (c, d) phase (color map) distributions for the non-diffracting Weber beams with different separation constants of $a = 1.5$ and 4 .

In order to reveal the particle manipulation mechanism with the Weber beam along the parabolic beam lobe, the transverse intensity and energy flow distributions are calculated for the Weber beams with a of 1.5 and 4, as shown in Figure 8 (a) and (b). The Weber beams consist of well-defined parabolic fringes with a parabolic dark region. It can be observed that the parameter a can modulate the bending of the beam parabolic shape, and the larger a gives the less beam bending for the parabolic profile. It is also seen that the energy flow follows the same direction along the parabolic fringes for the Weber beam, which indicates that the single-direction scattering force function will be applied on micro-particles along the transverse parabolic fringes. Concretely, the reason for energy flow in one direction is the existence of a large amount of in-line vortices with unitary charge rotating in the same direction in the phase profile, as shown in Figure 8 (c) and (d), resulting in the overall transverse energy flow along the parabolic intensity crest of the beam main lobe.

Now the Weber beam transportation experiment for large polystyrene particles with the size of $5 \mu\text{m}$ is conducted. The particle motion velocity and direction in the complex beam are usually determined by the radiation force function based on the special structure of the light field. However, in the current experiment, the gradient force function applied on particles from the

focusing structure at the beam transverse center cannot be neglected because the particle size is far larger than the laser wavelength. Thus, the particle transportation experiment will provide great insight into the combined effects of the radiation force and gradient force functions from the structured Weber beams. In order to implement the particle transportation, the optical tweezers setup based on a microscope is used to generate the non-diffracting Weber beam inside the sample chamber. The calculated phase hologram on the SLM for generating the Weber beam is shown in Figure 9 (a). Figure 9 (b) displays the measured transverse intensity profiles of the generated Weber beams with $a = 1.5$ and 4 inside the sample chamber.

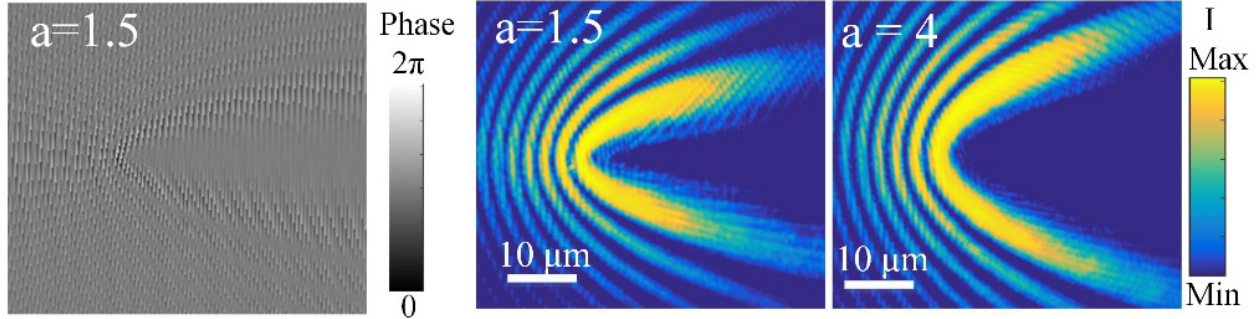


Figure 9: (a) Encoded phase profile to generate the Weber beam with complex field modulation method. (b) Experimental transverse intensity profiles for the Weber beams with $a = 1.5$ and 4.

Figure 10 presents the results of optical transportation for micrometer polystyrene spheres by the non-diffracting Weber beams, with the time-sequenced images taken from the recorded video clips to show the dynamic process of particle motion. The fixed laser power of 20 mW before entering the microscope objective lens is applied for both Weber beams. Polystyrene particles with the diameter of 5 μm are suspended in the water solution inside the sample chamber. It is observed that the main lobe of the Weber beam can transport particles stably in the parabolic trajectory due to the gradient force perpendicular to the beam trajectory. The parabolic coordinate along the main lobe of the Weber beam is defined as s . The particle motion directions along the lower ($s < 0 \mu\text{m}$) branch in Figure 10 (a)(a'), (d)(d') and the upper ($s > 8 \mu\text{m}$) branch in Figure 10 (c)(c'), (f)(f') of the main lobe are consistent with the energy flow direction in the transverse dimension. However, particles at the middle-upper ($0 < s < 8 \mu\text{m}$) region of the main lobe will move in the opposite direction toward the central region in Figure 10 (b), (e) and also have a transverse balance position close to the central region as shown in Figure 10 (b'), (e'), which is caused by the stronger gradient force applied on the particles than the scattering force in this region. It can also be found that by modifying the parameter a , the optical transportation of micro-particles will be constrained in the different parabolic beam tracks.

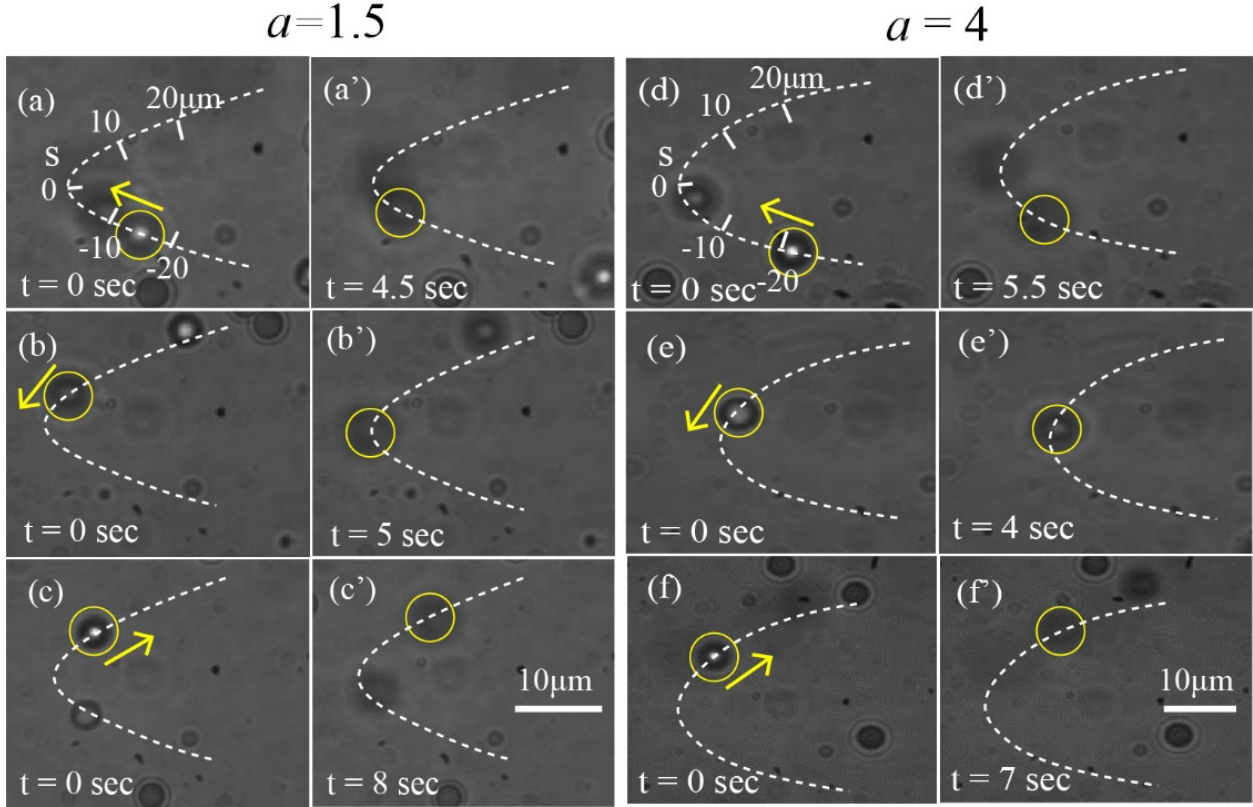


Figure 10: Optical transportation of micro-particles along the main-lobe of non-diffracting Weber beams with separation constants $a = 1.5$ and 4 . (a)(a'), (b)(b') and (c)(c') are the time-sequenced images to show single particle motion in lower ($s < 0 \mu\text{m}$), middle-upper ($0 < s < 8 \mu\text{m}$) and upper ($s > 8 \mu\text{m}$) branches of the main-lobe for the Weber beam with $a = 1.5$ (media 1). (d)(d'), (e)(e') and (f)(f') are results for particle motion in the Weber beam with $a = 4$ (media 2).

The transportation velocity of the particles is not invariant in the transverse dimension of the Weber beams. Figure 11 gives the average value and standard error of the particle's transverse transportation velocity along the parabolic fringes of the Weber beams with different separation constants $a = 1.5$ and 4 . There are five group data in each data point in Figure 11 and the direction of the parabolic coordinate s is consistent with the energy flow direction.

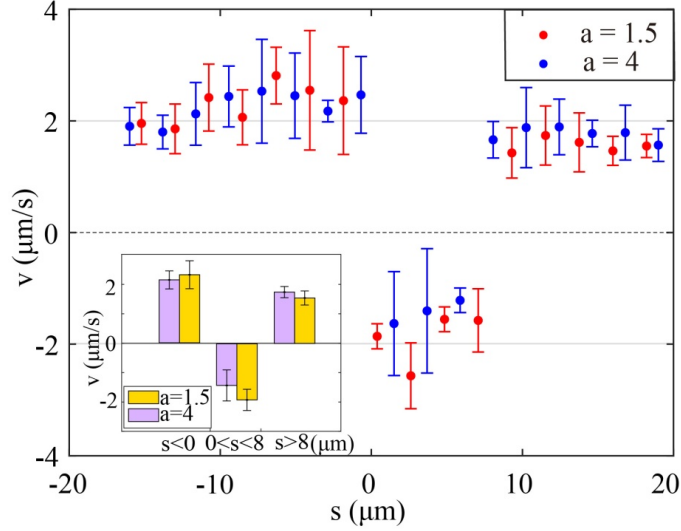


Figure 11: Transportation velocity of the particles along the parabolic main lobe of the Weber beams with different separation constants $a = 1.5$ (red) and 4 (blue). The inset shows the average velocity for the particle in the three regions of $s < 0 \mu\text{m}$, $0 < s < 8 \mu\text{m}$, and $s > 8 \mu\text{m}$.

Firstly, it can be seen that for the region of $s < 0 \mu\text{m}$ along the beam main lobe, the transportation velocity of particle as the particle approaches the center region of the beam is larger than the velocity as the particle leaves away from the center for both Weber beams. This is because the direction of the gradient force is towards the beams center with higher intensity, so that the gradient force will accelerate the particle when it approaches the center. On the contrary, for the region of $s > 8 \mu\text{m}$ the gradient force will decelerate the particle when it moves away from the center region. For the region of $0 < s < 8 \mu\text{m}$, the particle velocity is defined as negative as the particle travels towards the beam center in the opposite direction, where the gradient force is larger than the scattering force. Then we can see that the particle velocity in the region $0 < s < 8 \mu\text{m}$ of the Weber beam with $a = 1.5$ is larger than that of the Weber beam with $a = 4$. This phenomenon is caused by the stronger gradient force for the Weber beam with narrower parabolic shape ($a = 1.5$) than that for the Weber beam with wider parabolic shape ($a = 4$). For further demonstrating the gradient force function for the motion of large particles in the Weber beams, the inset in Figure 11 shows the average velocity of a polystyrene particle in the above three regions of $s < 0 \mu\text{m}$, $0 < s < 8 \mu\text{m}$, $s > 8 \mu\text{m}$. It is indicated that the stronger gradient force achieved in the more focused Weber beam with $a = 1.5$ will accelerate the particle more with higher average velocities of $2.3 \mu\text{m/s}$ and $-1.9 \mu\text{m/s}$ in the beam's regions of $s < 0 \mu\text{m}$, $0 < s < 8 \mu\text{m}$, compared to the average velocities of $2.1 \mu\text{m/s}$ and $-1.5 \mu\text{m/s}$ in these two regions of Weber beam with $a = 4$. On the other hand, the relative stronger gradient force will also obstruct the particle transportation further in the beam's region of $s > 8 \mu\text{m}$, leading to the average velocity in this region of Weber beam with $a = 1.5$ lower than that in the Weber beam with $a = 4$, with the average velocity of $1.54 \mu\text{m/s}$ and $1.74 \mu\text{m/s}$, respectively. Through the above analysis, we can see that the Weber beam with wider parabolic shape (larger a) can transport particles more smoothly.

2.1.4 Demonstration of optical transport of particles by using 3D cusp beams

We also demonstrated the optical transportation and accumulation of micrometer polystyrene particles by using the self-accelerating cusp beams with multi-channel bending structures. The cusp beams are generated through the phase modulation with the SLM and coupled into the microscope to conduct 3D optical manipulation. The cusp beams can transport particles within variable numbers of multi-channel bending structures by tuning the generating phase profile. Particularly, the transportation velocity and optical force profiles of the polystyrene micro-particles moving along the bending main lobes of cusp beams are analyzed. The parallel particle transportation and particle accumulation manipulation from all the bending channels are also demonstrated.

In Figure 12, the left figure shows the calculated optical intensity distribution of a 3D cusp beam with 4 curved channels, where the beam size is around $30\ \mu\text{m}$ by $30\ \mu\text{m}$ on the bottom and $5\ \mu\text{m}$ on the top. The laser light is coming from the bottom and the 3D cusp beam is generated with an SLM. The right figure shows the 3D structure of the cusp beam and its transport for particles, where the optical force applied on a particle will propel the particle to accelerate along the curved beam channel from the bottom 4 curved beams to the top beam due to the momentum transfer. We use this 3D beam as one example to demonstrate the particle transport in a water chamber.

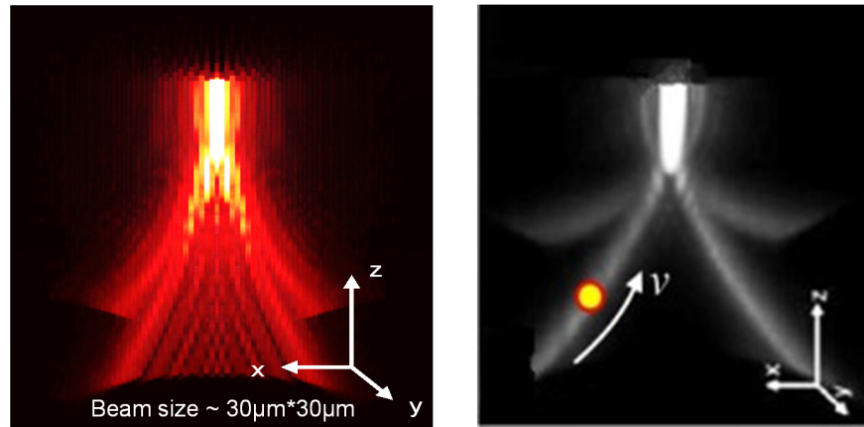


Figure 12: The left figure shows the calculated optical intensity distribution of a 3D cusp beam with 4 curved channels. The right figure shows the transport of particles moving upwards along the cusp beam channels.

Figure 13 (a)-(d) presents the results of optical transportation for a single polystyrene particle with the diameter of $2\ \mu\text{m}$ by the cusp beam with $m = 4$ along the self-accelerating channel in the fourth quadrant, with the time-sequenced images taken from the recorded video to show the dynamic process of particle motion. The laser power is 60 mW at the entrance pupil of the microscope objective lens. The particle is suspended in a water solution inside the sample chamber. It is observed that the single particle is transported stably by the bending channel towards the cusp beam center due to the radiation force along the channel. Meanwhile, the transported particle also involves the axial motion following the 3D bending channel structure, which is verified by the fact that the images of particles are out of focus during the transportation. Figure 13 (e)-(h) are the images showing the single particle transported by each channel of the cusp beam in every quadrant,

indicating the equal transportation capability for all the four self-accelerating channels of cusp beams.

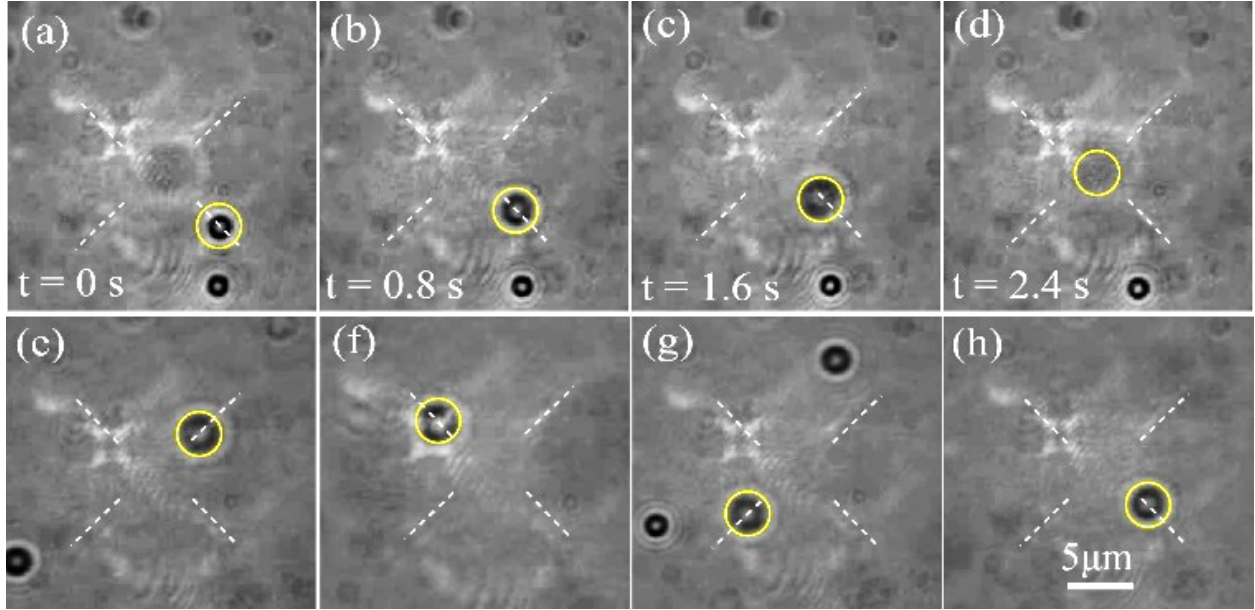


Figure 13: (a)-(d) The dynamic process of a single particle transported along the self-accelerating channel of a cusp beam with $m = 4$. (e)-(h) Single particle transportation along each channel of the cusp beam in every quadrant. The yellow circle shows the location of a particle transported along the channel of the cusp beam. The dashed lines indicate the transverse position of self-accelerating channels of the cusp beam.

The particle's transportation velocity by cusp beams along their self-accelerating channels can be controlled flexibly by the adjustment of beam energy. In order to quantitatively reflect such velocity regulation and the dynamic motion of transported particles, Figure 14 (a) and (b) show the variations of transverse velocity v_r and derived total velocity $v = \sqrt{v_r^2 + v_z^2}$ as functions of the radial distance by tuning the laser power at 40 mW and 60 mW, typically along the bending channel in the fourth quadrant of the cusp beam with $m = 4$.

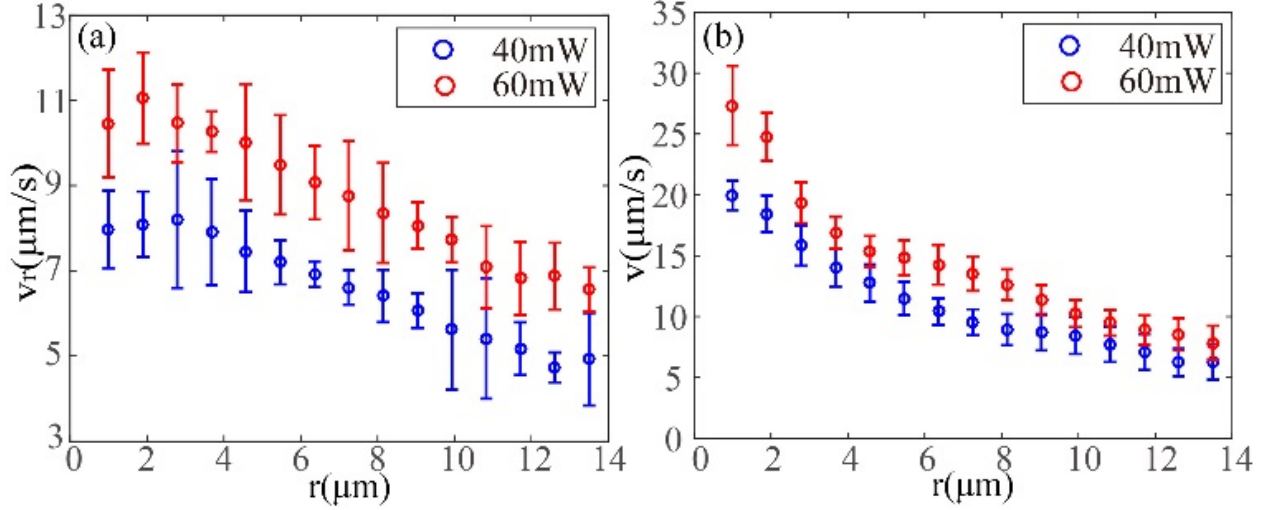


Figure 14: The variations of (a) transverse velocity in the radial direction and (b) total velocity along the 3D cusp beam channel for a single particle as functions of the radial distance by tuning the laser power at 40 mW and 60 mW.

v_r is measured based on the tracked transverse locations of the particle from the recorded video, while v_z is derived from the deflection curve which calibrates the 3D position information of the beam channel and thus the ratio between v_r and v_z . Here the particle is expected to move stably along the 3D bending channel of the cusp beam. It is observed that the motion of a single particle along the beam channel is an accelerating process on the whole. Furthermore, higher average transportation velocity along the self-accelerating channels can be achieved by increasing the laser power.

Stable particle transportation by the cusp beam results from the combination of the gradient force and radiation pressure within the self-accelerating beam channels. The gradient force will trap the particle and keep it inside the bending channel of the cusp beam, while the radiation force F_{opt} applied on the polystyrene particle will drive the particle to move along the channel based on Newton's second law of motion, $F_{opt} = ma + F_{vis}$, where m and a are the mass and acceleration of particle. F_{vis} is the viscous force of water for the moving particle as $F_{vis} = 6\pi\eta r_0 v$, where r_0 and v are the particle radius and the motion velocity, $\eta = 0.8926 \text{ mm}^2/\text{s}$ is the viscosity of water. In the calculation, the ma term is very small and can be neglected compared to the F_{vis} term, so that $F_{opt} \approx F_{vis}$. Figure 15 (a) and (b) show the variations of ma and F_{opt} as functions of the radial distance in 3D space. Figure 15 (a) clearly shows the dynamic accelerating process of the particle along the beam channel, with relatively constant acceleration at the initial stage and then rapidly increased acceleration close to the beam center. Figure 15 (b) shows that the optical radiation force for a single particle keeps increasing towards the beam center along the bending channel of the cusp beam. Then the average radiation force applied on the particle is proportional to the laser power. It is noted that the magnitude of the optical force for a single particle is around 1 pN, which indicates the exquisite transportation capability of cusp beams for microscale objects in optical manipulation.

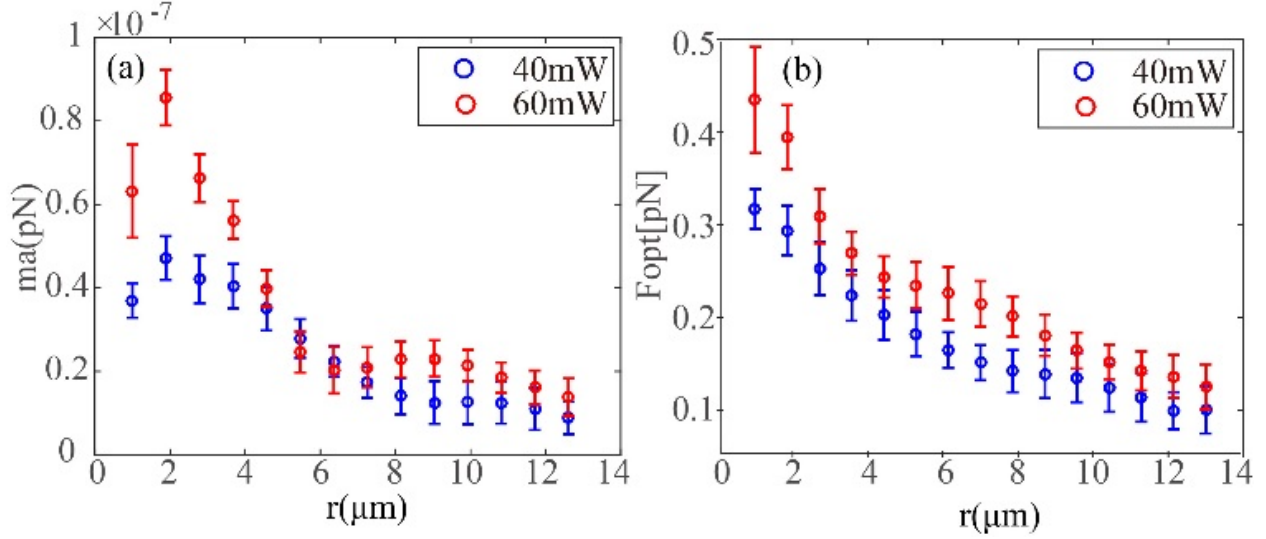


Figure 15: Variations of (a) ma and (b) F_{opt} as functions of the radial distance in 3D space applied on a single particle by the cusp beam with $m = 4$ at the laser power of 40 mW and 60 mW.

2.1.5 Experimental observation of the plasmonic force propulsion of particles

The optical force field produced by asymmetric plasmonic nanostructures for accelerating and expelling particles are investigated with an optical tweezer setup for the demonstration of plasmonic force propulsion of particles in aqueous solution. The fabricated sample, shown in Figure 5, is the asymmetric plasmonic triangle-hole array in a 50 nm thick gold film deposited on a quartz substrate. The fabricated plasmonic triangle-hole array is given with side-wall dimension of 145 nm and period of 290 nm. The asymmetric triangle-hole negative patterns will provide strong gradient optical fields for plasmonic propulsion. A strong plasmonic resonance mode around the visible wavelength of 600 nm has been observed in experiment.

The sample is put at the bottom plate of the water chamber in our optical tweezer setup. The laser beam is incident upward from an objective lens through the sample into the particle water solution. The green laser at 532 nm is used to focus on the sample area in the experiment for optical excitation of the plasmonic mode. Figure 16 displays the recorded CCD images of the water chamber for our experimental results of the plasmonic force propulsion of 2 μm -diameter polystyrene spherical particles. The orange square area is the asymmetric plasmonic triangle-hole array. Figure 16 (a) is the image of the triangle-hole array, and it can be seen that an elliptical focused laser spot on the sample is used and the laser spot size is about 2 μm x 3 μm . Figure 16 (b) is the image once the laser beam is focused onto the plasmonic triangle-hole array with 2 μm polystyrene particles in solution above the sample. The focused laser spot (marked as a cross) excites surface plasmons and there are several particles located in the sample area. The laser incidence power is just 5 mW. In Figure 16 (c), we move the sample stage to the left so that two targeted polystyrene particles (marked as red circles) are getting closer to the laser focused plasmonic spot (marked as a cross) on the sample. The reference particle without movement (marked as a blue circle) is used to judge the relative motion of the targeted particles. We then observe that both particle 1 and particle 2 are expelled to escape away quickly from the bright laser spot to the right, almost along the horizontal direction, as shown from Figure 16 (c) - (f). The particle propulsion distance is about 5 μm during one second. This indicates that high concentrated

plasmonic energy distribution on the sample is obtained to drive particle motion effectively with a 5 mW low-power laser beam.

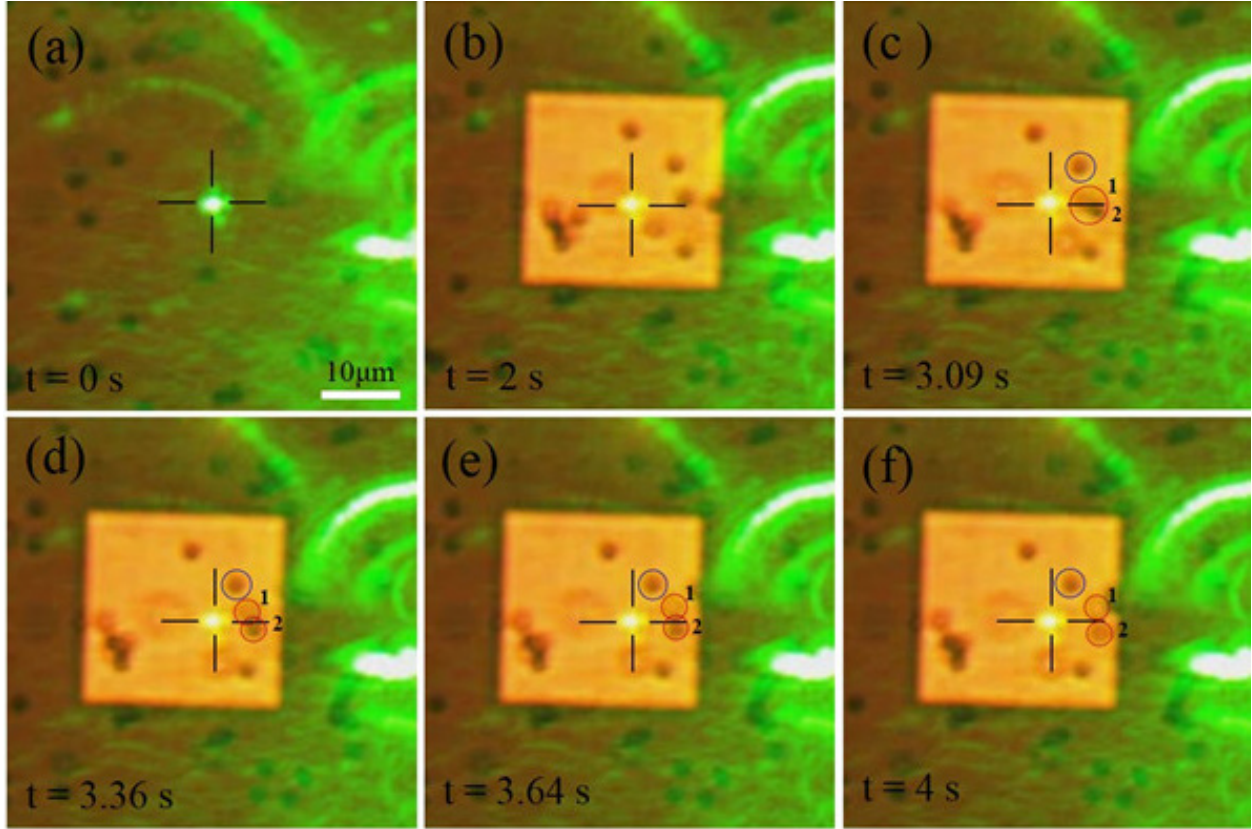


Figure 16: The CCD images of the water chamber to observe the plasmonic propulsion of the 2 μm -diameter polystyrene spherical particles, and the asymmetric plasmonic triangle-hole array is excited by a green laser spot (marked as a cross). Two targeted polystyrene particles (particle 1 and particle 2, marked as red circles) are expelled to escape away quickly from the bright laser spot in (c) - (f). The reference particle without movement (marked as a blue circle) is used to judge the relative motion of the targeted particles.

We use the recorded CCD video to determine the particle transverse velocity at different time steps. In Figure 17, the particle velocity is plotted as a function of time, giving the particle transverse transport speed in a range of 2 - 12 $\mu\text{m}/\text{s}$ in the water chamber. The time point $t' = 0$ is set at when the particles start to move from the focused laser spot. According to the video, the particle 1 is repulsed at the time of $t = 3.09$ s (Figure 16 c), but the particle 2 starts escaping at the time $t = 3.36$ s (Figure 16 d), thus they get different propulsion time durations. For comparing the motion of the two particles in the same time interval, we plot the velocity variation of the two particles at the initial propulsion stage $t' = [0, 0.5]$ second. It is noted that the vertical motion for the particles is also involved in three dimensions. Here in Figure 17, we only show the particle transverse velocity along the propulsion trajectory.

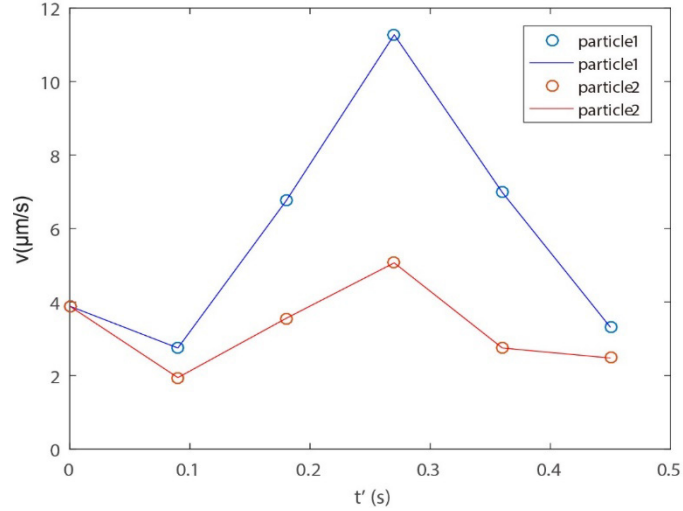


Figure 17: The particle transverse velocity analysis during the plasmonic propulsion process.

The optical driving force applied on the particle is further determined by the particle acceleration and the drag force in Figure 18, with the formula of $F_{opt} = m \cdot dv/dt + C_{drag} \cdot v$, where optical force F_{opt} for particle propulsion is related to the particle velocity v , stokes drag coefficient C_{drag} , particle mass m , and particle acceleration dv/dt . The observed optical forces on the particle 1 and the particle 2 are in a range of 0.03 ~ 0.18 pN with a 5 mW low-power laser beam.

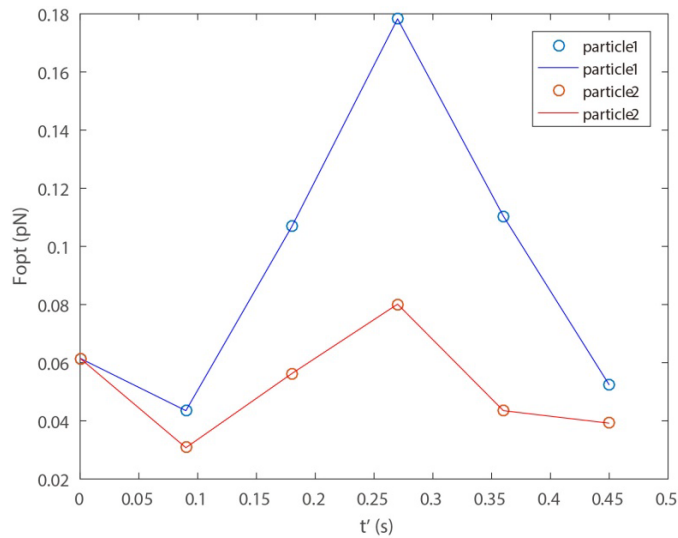


Figure 18: The optical force analysis during the plasmonic propulsion process.

We have successfully observed the plasmonic force propulsion of particles on top of an asymmetric plasmonic nanostructure sample.

2.2 Specific Objective 2: Off-axis Illumination and Equilibrium Temperature of the Nanostructures

Calculations to determine the equilibrium temperature of the nanostructures under incident light were also performed in order to ensure that the nanostructures would reach thermal stability without melting at the necessary operating conditions. Light power incident on the thruster is dependent on the incident light angle, Figure 19, and the focusing diameter of the collection lens (area, A_{lens}), Eq.(1).

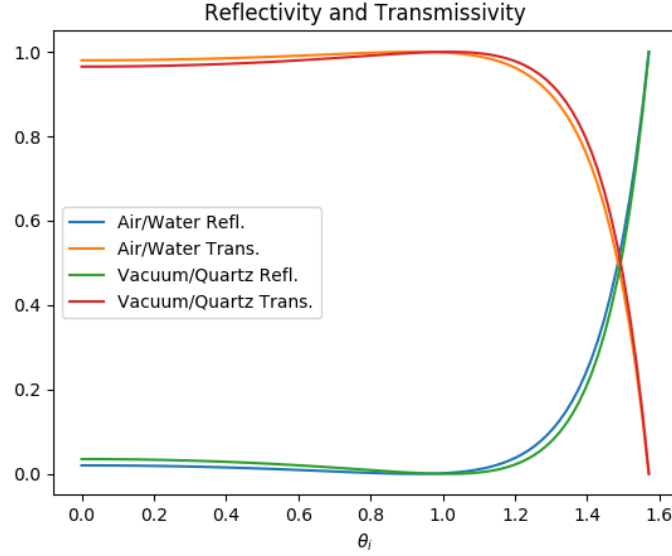


Figure 19: The reflected and transmitted light striking a flat surface as it depends on the incident angle, normalized to the incident radiation.

2.2.1 Thermal stability

The light power incident on a single nanostructure that makes up the thruster array is given by Eq.(2) It is clear from this relationship that maximizing the collection lens size increases the power incident on each individual nanostructure, which increases the accelerating plasmonic force on the nanoparticle propellant.

$$P_{thruster} = IA_{lens} \quad (1)$$

$$P_{nanostructure} = P_{thruster} \frac{A_{nanostructure}}{A_{thruster}} = I \frac{A_{lens} A_{nanostructure}}{A_{thruster}} \quad (2)$$

The nanostructure radiates and conducts energy in addition to absorbing it. Therefore, the Stefan-Boltzmann law can be used to calculate how much energy is radiated, Eq. (3)(a), and the conductive heat transfer can be calculated using Eq. (3)(b).

$$(a) P_{rad} = \varepsilon A_{ns} \sigma (T^4 - T_e^4) \quad (3)$$

$$(b) P_{cond} = \frac{(T-T_e)A_{ns}}{\frac{s_{ns}}{k_{ns}} + \frac{s_{sub}}{k_{sub}}}$$

where ϵ is the emissivity of the material, σ is the Stefan-Boltzmann constant, $s_{ns} = 50 \text{ nm}$ and $s_{sub} = 1500 \text{ nm}$ are the thickness of the nanostructure and substrate, respectively, and, k_{ns} and $k_{sub} = 1.4 \frac{W}{mK}$ are the thermal conductivities of the nanostructure and substrate, respectively. T_e is the temperature of the environment, taken to be 298.15 K and T is the temperature of the material. Light intensity ranging from 0 to 1 GW/m^2 is used to capture the effect of instances in which the nanostructures are shaded and in which an optical focusing lens is used and coupled with a laser. Setting the incident power equal to the sum of the Stefan-Boltzmann radiated power and the conductive heat transfer, we can find the equilibrium temperature of the nanostructures. We also took the opportunity, at this stage, to compare the thermal response of the nanostructures when composed of different materials. The materials tested were gold (Au), gallium arsenide (GaAs), indium tin oxide (ITO), and aluminum zinc oxide (AZO). We chose to compare Au to a variety of semiconductors because they experience lower losses¹² and increased tunability¹³ when compared to metals in the near infrared and optical frequency range. The material property values are listed in Table 1.

Table 1 The emissivity and thermal conductivity values for each material used in the equilibrium temperature analysis

	ϵ	k [W/m/K]	Melting point [K]
Au	0.47	310	1337
GaAs	0.648	0.201	1513
ITO	0.25	5.86	2800
AZO	0.6	7.5	2248 (ZnO)

Figure 20 shows how the equilibrium temperature is dependent upon the light intensity and material composition of the nanostructures. From this plot we see that the relationship is linear which implies most of the heat generated by absorbing the incident light is conducted away from the nanostructures through the substrate. We also see that GaAs conducts heat the least efficiently and therefore has a higher equilibrium temperature for all incident light intensities. With the provided melting point values (with ZnO in place of AZO) we see that Au and GaAs are at risk of melting for light intensities above 978 MW/m^2 and 593 MW/m^2 , respectively.

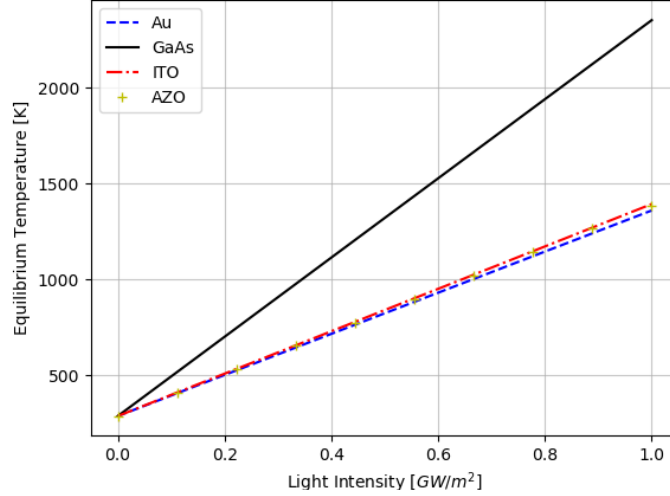


Figure 20: Equilibrium temperature of asymmetric nanostructures composed of different materials

2.2.2 Electromagnetic response for different materials

Semiconductors have been coupled with plasmonic antennas in configurations such as Abb, et al.'s Au-ITO hybrid system that enables ultrafast nanoplasmonic switching¹⁴ and more recently plasmonic semiconductors, such as ITO, have been used in ambient air as high-efficiency thermal emitters¹⁵. Therefore we explore the effects semiconductors such as GaAs, ITO, and AZO have on the electromagnetic response of a set of two asymmetric trapezoidal nanostructures as shown in Figure 21. Previously, we have optically characterized^{5,16} this nano-unit for a material composition of gold and the following dimensions: $w = 100 \text{ nm}$, $l = 400 \text{ nm}$, and $g = 50 \text{ nm}$.

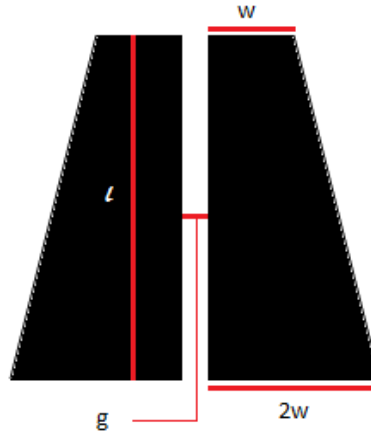


Figure 21: Nano-unit geometry for asymmetric trapezoidal nanostructures.

The dielectric function of a material governs how that material responds to incident electromagnetic radiation. Eldlio, et al. proposes¹⁷ that the combination Drude-Lorentz model works well to describe the dielectric function of a semiconductor. The Drude model is a classical description of the optical response of metals and treats the atomic valence electrons as freely moving (also known as the sea of electrons or free electron model). The Drude model, Eq. (4), is sufficient for metals but not semiconductors because it does not capture the bound electron and

hole attributes nor the spatial distribution of the dielectric constant that can be present in semiconductors. ϵ_∞ is the high frequency dielectric permittivity, ω_p is the plasma frequency, and γ is the damping factor. The plasma frequency is defined in Eq. (5), where ϵ_0 is the permittivity of free space, n is the charge carrier density, e is the electron charge, and m^* is the effective electron mass.

$$\epsilon_r = \epsilon_\infty - \frac{\omega_p^2}{\omega(\omega + j\gamma)}. \quad (4)$$

$$\omega_p = \sqrt{\frac{ne^2}{\epsilon_0 m^*}}. \quad (5)$$

The Lorentz model, Eq. (6), is valid for materials with bound electrons oscillating around their parent atom. Like the Drude model, the Lorentz model is insufficient to describe the optical response of semiconductors because of its strong dependence on the resonant frequency and that it is only valid in the frequency regime in which intraband transitions do not occur. ∇_ϵ is an amplitude factor, or oscillator strength, determined by the difference between the static permittivity, ϵ_{st} , and the high frequency permittivity, ϵ_∞ : $\nabla_\epsilon = \epsilon_{st} - \epsilon_\infty$. The static permittivity of a semiconductor is measurable when the material is undoped. ω_0 is the resonant frequency of the charge carriers and is equivalent to the band gap energy in a semiconductor. The Lorentz model makes use of the analogy that is present between a bound electron and an oscillator (Lorentz oscillator) to model the system with an associated resonant frequency.

$$\epsilon_r = \epsilon_\infty + \frac{\nabla_\epsilon \omega_p^2}{-\omega^2 + j\gamma\omega + \omega_0^2}. \quad (6)$$

The Drude-Lorentz model is a linear combination of the constituent models, as shown in Eq. (7), and provides a better description of the dielectric permittivity of a material because it can effectively couple the contributions from interband (bound-electron) and intraband (free electron) effects which are present in a semiconductor. This combined description was used to define material response in our computational models.

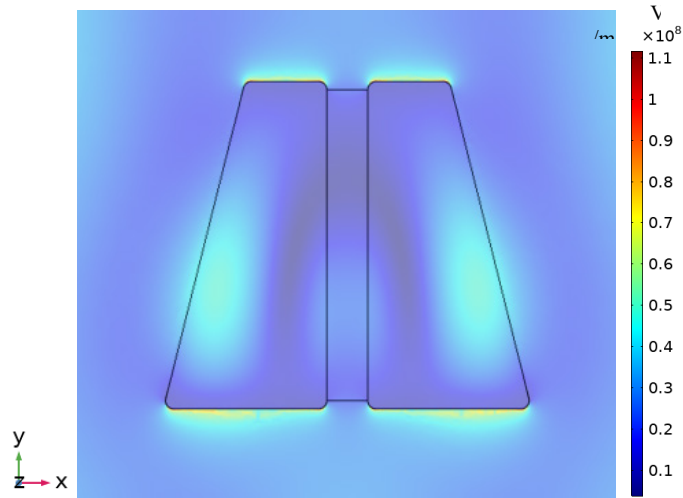
$$\epsilon_r = \epsilon_\infty - \frac{\omega_p^2}{\omega(\omega + j\gamma)} + \frac{\nabla_\epsilon \omega_p^2}{-\omega^2 + j\gamma\omega + \omega_0^2}. \quad (7)$$

COMSOL Multiphysics modeling software was used to develop a numerical three dimensional, finite element, full-wave analysis of the optical interaction between incident radiation and the trapezoidal nanostructures. Floquet periodic boundary conditions were applied on the four boundaries perpendicular to the plane of the structure in order to model a periodic distribution of the nano-unit structures. The top and bottom capping layers were set as perfectly matched layers (PML) to ensure no backscattering from the boundary. A port was specified above the nanostructures to indicate the inlet for the incident radiation and was polarized along the width, w , of the nanostructures. Material composition was controlled by specifying the variables in the Drude-Lorentz model. The parameters used in the model are tabulated below in Table 2.

Table 2: Specified parameters for the Drude-Lorentz model for each material studied

	Au ^{18,19}	GaAs ²⁰⁻²³	ITO ^{24,25}	AZO ²⁶⁻²⁸
Oscillator Strength, ∇_{ϵ}	0.94	2.01	3.781	7.93
Resonance Frequency, ω_0	4.03e15 rad/s	2.93e7 rad/s	7.02e15 rad/s	5.12e15 rad/s
Plasma Frequency, ω_p	2.15e15 rad/s	2.13e11 rad/s	1.14e15 rad/s	1.2e15 rad/s
High Frequency Permittivity, ϵ_{∞}	1.53	10.89	4.00	2.97
Static Permittivity, ϵ_{st}	2.47	12.9	7.78	10.9
Damping Term, γ	17.1e12 rad/s	2.60e13 rad/s	7.10e14 rad/s	6.25e13 rad/s
Charger Carrier Density, n	5.9e22 1/cm ³	1e18 1/cm ³	6.64e20 1/cm ³	1.13e20 1/cm ³

Figure 22 shows, as an example, the GaAs nanostructures in the COMSOL software interacting with light at a wavelength of 540 nm. The color plot indicates the profile of the magnitude of the electric field in the y-direction. The electric field in the gap between the two nanostructures is computed and used to compare the response of the different materials. A rectangular test area is drawn between the two nanostructures, visible in Figure 22, over which the average of the magnitude of the electric field in the y-direction is computed for each incident wavelength.

**Figure 22: Color plot of the magnitude of the electric field in the y-direction at a wavelength of 540 nm (material: GaAs).**

The averaged values calculated over the rectangular test area are plotted in Figure 23 versus wavelength for each material composition. The curve for Au shows a uniform response over the majority of the test wavelengths, leveling off at about 28 MV/m as wavelength increases. There is also a localized but distinct trough located at approximately 450 nm that coincides with a peak in the reflectance and absorbance curves (Figure 24). The GaAs curve displays an overall increasing

trend as the wavelength increases and contains two local peaks of 14.5 MV/m and 28.1 MV/m located at approximately 540 nm and 850 nm, respectively. The ITO and AZO curves show nearly identical responses with a small peak of 28.6 MV/m at about 850 nm and an overall arch-shaped increasing trend as wavelength increases. The AZO curve does indicate a slightly stronger field produced than ITO at lower wavelengths with an approximate increase of 700 kV/m at a wavelength of 600 nm from 24.4 MV/m (ITO) to 25.1 MV/m (AZO).

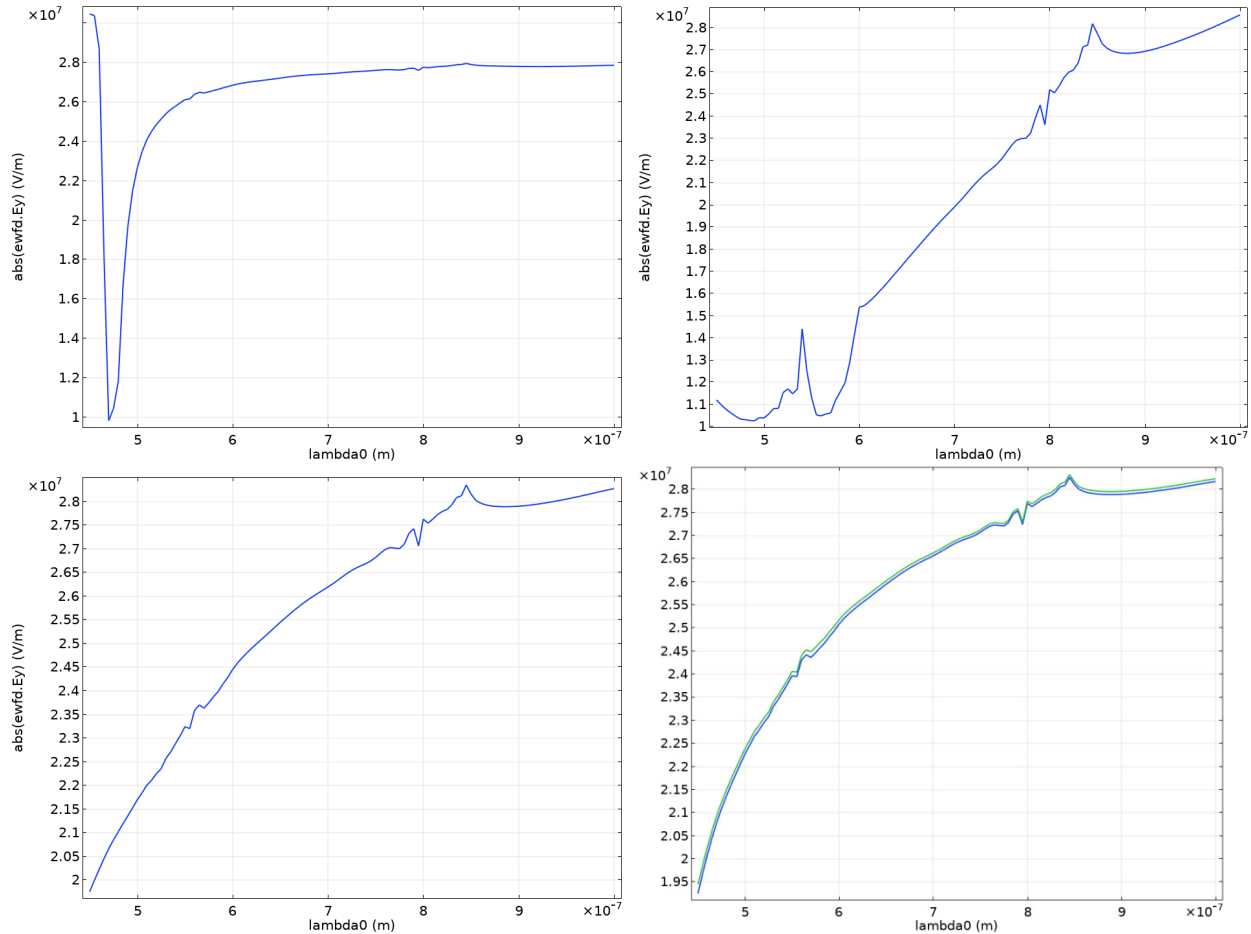


Figure 23: Magnitude of the electric field in the y-direction averaged over the space within the gap versus incident wavelength. (top left) Au; (top right) GaAs; (bottom left) ITO; (bottom right) AZO, also includes plot of average of the magnitude of E within the gap

Each curve contains an artifact in the data at 800 nm. 800 nm is also the period, or pitch, of the nanostructures therefore the artifact is likely a minor error resultant of the Floquet Boundary Conditions.

The reflected, transmitted, and absorbed light resulting from the interaction was also calculated and plotted as a fraction of the total incident light in Figure 24 (reflectance, transmittance, and absorptance; or RTA). There is a peak in the Au reflectance at about 440 nm and in the absorptance at about 460 nm that coincides with the resonance frequency value of 4.03×10^{15} rad/s or 467 nm used in the Lorentz piece of the numerical model. For GaAs, the transmittance increases and the reflectance decreases with increasing wavelength but at different

rates. The absorptance also increases which corresponds to the increasing electric field produced by the nanostructures and is evident in Figure 23. Finally, the range of values for each RTA curve for ITO and AZO is so small (i.e. 0.002 for ITO reflectance and 0.0018 for AZO reflectance) that the RTA curves are essentially uniform over the domain of the wavelengths.

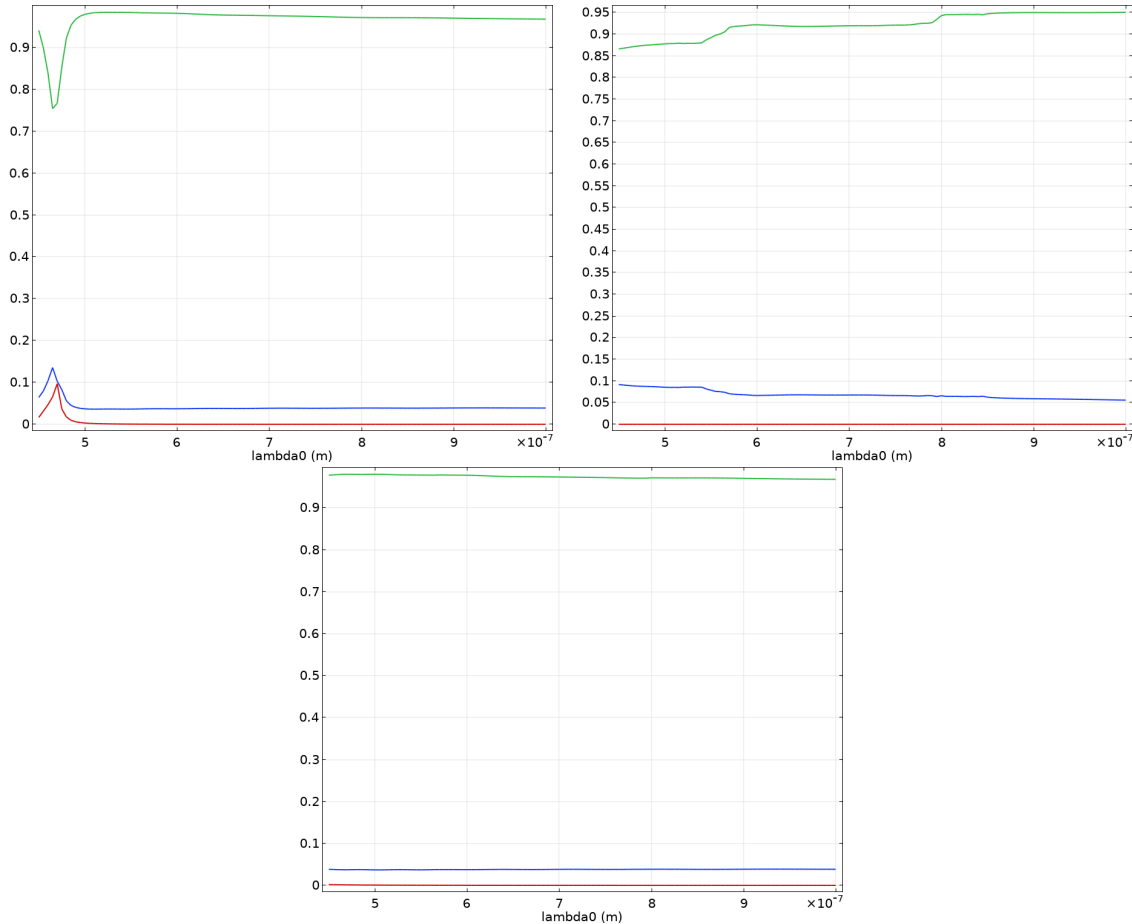


Figure 24: Reflectance (blue), transmittance (green), and absorptance (red) curves for each material versus wavelength. (top left) Au; (top right) GaAs; (bottom) ITO and AZO.

2.3 Specific Objective 3: Nanoparticle Propellant Injection using the Dielectrophoretic Forcing

The manipulation of micro/nanoparticles of solid or aqueous material by way of gradient electromagnetic fields is used extensively in the fields of photonics and microfluidics. One such action mechanism is that of the dielectrophoretic force. Dielectrophoresis is well known and has been utilized in the manipulation of liquid microflows and pico/nanoliter droplets for siphoning²⁹, separation and mixing³⁰ in chemical and biological experiments, and transport applications³¹. Liquid tendrils have been guided from a droplet along wall-less straight³² and curved³³ virtual microchannels by way of the dielectrophoretic force enabling enhanced flexibility for the aforementioned transport techniques. Additional nanoparticle manipulation schemes make use of plasmon generated gradient force fields which have been studied for the acceleration of net-neutral

nanoparticles via dielectrophoresis with applications in nanosatellite propulsion systems^{5,16,34}. We study a dielectrophoretic tilted plate geometry that enables variable injection of nanoparticles or microliter quantities of liquids into manipulation/acceleration schemes such as those mentioned above and can double as a mass storage reservoir when injection is inactive.

2.3.1 Theory of dielectrophoresis

Dielectrophoresis occurs when a net-neutral particle is placed in a non-uniform electric field. The electric field polarizes the particle and the polarized particle then feels a force due to the gradient in the magnitude of the field (Figure 25). The direction of the force depends on the difference between the permittivity of the particle and that of the surrounding medium. The dielectrophoretic (DEP) force is utilized in a variety of research fields but most commonly in microfluidics and biomedical applications³⁵. Its effectiveness in these areas is due, in part, to its ability to separate particles according to their polarizability and/or size. We desire to make use of its ability to precisely control the motion and flow of a concentration of net-neutral nanoparticles.

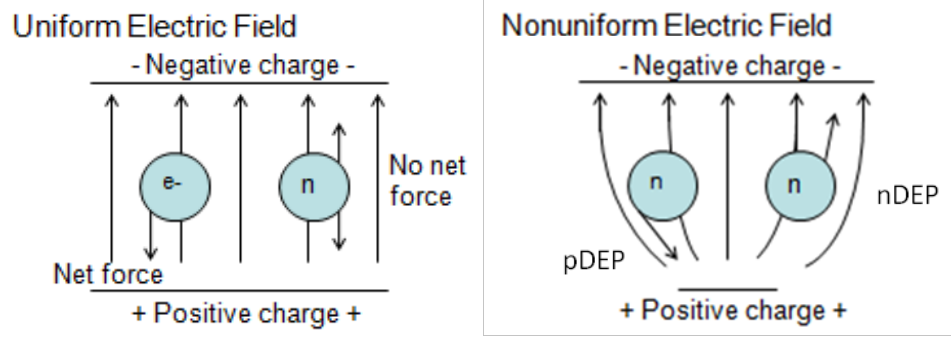


Figure 25: Particle motion in uniform and non-uniform electric fields

Research has shown that dielectrophoresis can be used to continuously pump particle-laden microfluidic flows through virtual (wall-less) channels using microstructured electrodes in a variety of configurations³¹. Research has also shown that dielectrophoresis can filter particles from a stream of gas; expanding the usability of the DEP mechanism³⁶. Further progress in this field has demonstrated that particulate matter can be separated by use of dielectrophoresis in a vacuum environment, known as vacuum dielectrophoresis³⁷. Vacuum dielectrophoresis eliminates certain interactions due to the particles moving in a medium/fluid, making the DEP force the only interaction with the particles in the plane perpendicular to the force of gravity.

The DEP-induced motion depends on the dielectric properties of the particles and the surrounding medium. Specifically, it depends on the effective polarization of the suspended particles. If the polarizability of a net-neutral nanoparticle is greater than the polarizability of the surrounding medium, then the nanoparticle will be pushed toward the stronger region of the electric field (pDEP) and vice-versa (nDEP) if the medium has higher polarizability. Equations (8) and (9) define the DEP force acting on a particle.

$$\vec{F}_{DEP} = 2\pi R^3 \epsilon_m k \nabla (|\vec{E}|)^2. \quad (8)$$

$$k = \frac{\epsilon_p - \epsilon_m}{\epsilon_p + 2\epsilon_m}. \quad (9)$$

R is the radius of the particle. ϵ_m is the permittivity of the surrounding medium in which the particles are suspended. k is the Clausius-Mossotti factor, defined in Equation (9), that relates the permittivity of the particle and medium and is positive when the particle permittivity is greater than the medium permittivity. \vec{E} is the electric field. From these equations we see that the DEP force is proportional to the cube of the radius of the suspended particles as well as the gradient of the magnitude of the electric field.

2.3.2 Dielectrophoretic injector design

The DEP force can be used to inject nanoparticles into a photonic particle manipulator. As described above, the DEP force is active in the presence of a non-uniform electric field. It acts on net-neutral particles along the direction of the gradient of the non-uniform field. Therefore, to harness the DEP force and use it to propel nanoparticles into particle manipulating platforms, we must design an electric field that is non-uniform and whose gradient tends to lie along a single direction. We investigate here a wedge-shaped prism, whose 2-D cross section is a simple tilted plate capacitor. This geometry creates a steady, non-uniform electric field when supplied with a DC voltage and the electric field can be easily solved analytically in 2-dimensions using the following equation derived from Coulomb's Law for the electric field due to a distributed charge.

$$\vec{E}(\vec{r}) = \frac{1}{4\pi\epsilon_0} \int \rho(\vec{r}') \frac{\vec{r}-\vec{r}'}{|\vec{r}-\vec{r}'|^3} d^3\vec{r}'. \quad (10)$$

For 2-dimensions, let the charge density $\rho(\vec{r}') \rightarrow \lambda(\vec{r}') = Q/L$ where Q is the charge on the plate and L is its length. With this reduction and the definitions in Equations (11), (12) and (13) that give the location of a test point and shape of the surfaces, we can define the total electric field between the surfaces as the sum of the electric fields produced by each surface, Equation (14).

$$\vec{r} = y_0\hat{j} + z_0\hat{k}. \quad (11)$$

$$\vec{r}'_L = y'\hat{j} + (my' - h)\hat{k}. \quad (12)$$

$$\vec{r}'_U = y'\hat{j} + (h - my')\hat{k}. \quad (13)$$

$$\vec{E}(\vec{r}) = \vec{E}_U(\vec{r}(y, z)) + \vec{E}_L(\vec{r}(y, z)). \quad (14)$$

Figure 26 illustrates the variables contained in Equations (11) - (13).

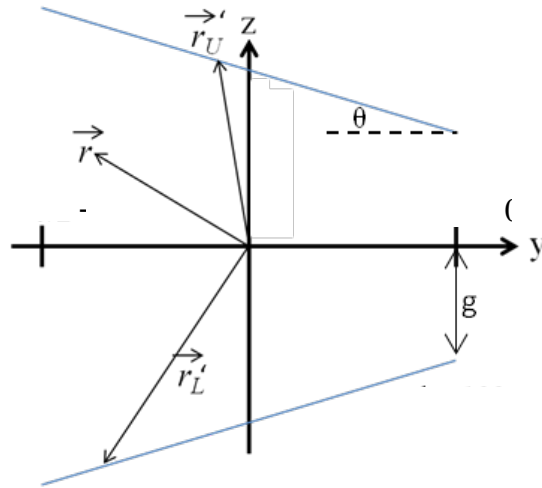


Figure 26: Visual definitions of variables in equations (11), (12), and (13). $b = 50 \mu\text{m}$, $g = 7 \mu\text{m}$, $\theta = \text{variable}$.

The tilted plate capacitor cross-section is shown in Figure 27, where the red lines show the silhouette of the injector, and the design is such that the particles will start in the injector (injector doubles as a storage tank) and then exit to the manipulation platform on the right. The upper and lower surfaces of the injector (red lines in the image) are electrically separated and a potential difference is maintained across them in order to produce the desired electric field. A dielectric, rectangular guide-sleeve (solid blue lines) is inserted along the axis of the injector between the charged surfaces with separation distance equal to the opening width, $2g$, of the injector exit. The dielectric guide sleeve keeps the particles away from the conducting plates where, in close proximity to the plates, the gradient of the electric field pointing toward the plate would act to trap them in pDEP.

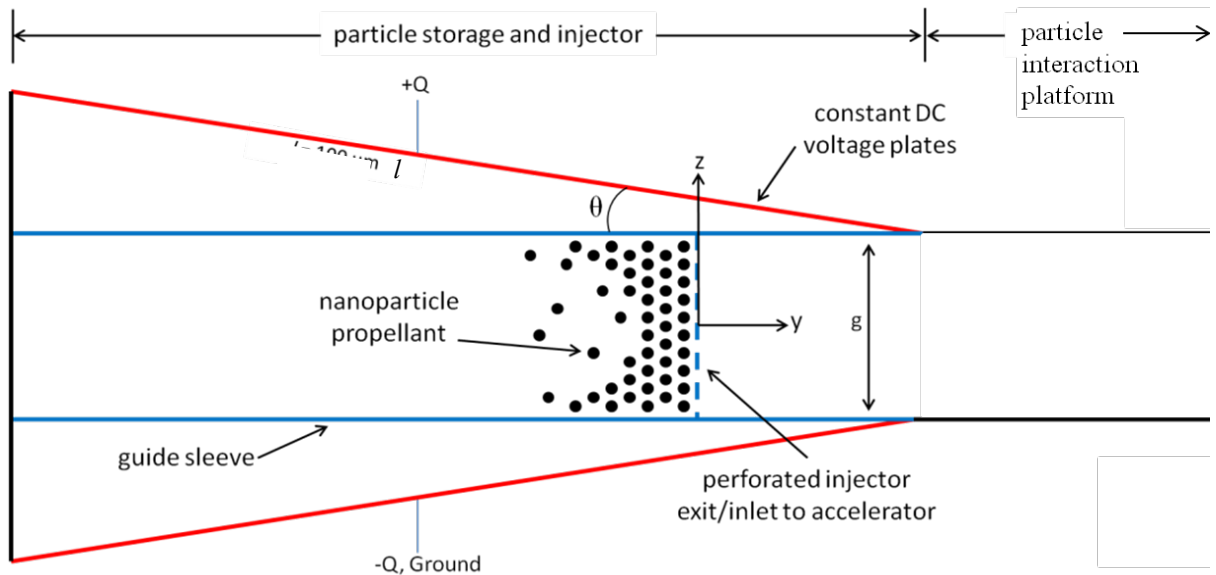


Figure 27: Geometry of tilted plate nanoparticle injector

Summing the electric fields due to the upper and lower plates allows the conversion of Equation (10) to Equation (14) with \vec{E}_L , the electric field produced by the lower plate, defined by Equation (15) and \vec{E}_U , the electric field produced by the upper plate, defined in Equation (16).

$$\vec{E}_L(\vec{r}(y, z)) = \frac{Q}{4\pi b \epsilon_0} \int_{-b}^0 \frac{(y_0 - y')\hat{j} + (z_0 - my' + h)\hat{k}}{((y_0 - y')^2 + (z_0 - my' + h)^2)^{3/2}} dy'. \quad (15)$$

$$\vec{E}_U(\vec{r}(y, z)) = \frac{-Q}{4\pi b \epsilon_0} \int_{-b}^0 \frac{(y_0 - y')\hat{j} + (z_0 + my' - h)\hat{k}}{((y_0 - y')^2 + (z_0 + my' - h)^2)^{3/2}} dy'. \quad (16)$$

The electric field produced by this setup is plotted in Figure 28 (a) for plate angle $\theta = 0.0^\circ$ and Figure 28 (b) for $\theta = 25^\circ$. For validation, the $\theta = 0^\circ$ case is compared to the electric field produced by a parallel plate capacitor, which assumes infinite electrodes, $E_{cap} = V/d$. E is the electric field, V the electric potential difference between the two electrodes, and d the separation distance between the two capacitor electrodes. With $V = 2.0 V$ and $d = 14 \mu m$, $E_{cap} \cong 142.9 kV/m$. Let $V = 2.0 V$ and $d = 14 \pm 0.16 \mu m$ for the analytical model solution with finite electrodes. The minor difference in plate separation values is an intentional offset for the analytical solution because the electric field derived from Coulomb's law is proportional to $1/r^2$, which means that as d approaches $14 \mu m$, the distance to the second plate approaches zero and the electric field contribution goes to infinity. The electric field produced by the plates in the analytical solution, at the point $y = -25 \mu m, z \cong 7 \mu m$ where the field is max, is $E_{analytical} \cong 143.5 kV/m$. The percent error between the finite plate analytical and infinite plate parallel capacitor solutions is 0.42% . The electric field distribution in Figure 28 (b) for the $\theta = 25^\circ$ plate angle is steady and non-uniform, increasing in strength from left to right. The solid, black, diagonal lines represent the edges, or silhouette, of the wedge-shaped injector while the short vector lines indicate the electric field produced between the electrodes. Along the centerline ($z = 0$), one can see that the electric field lines increase in strength with increasing y -position. These properties are plotted in Figure 29. We have disregarded the configuration of the electric field outside of the particle injection structure because it has no effect on the motion of the particles and is assumed to be shielded.

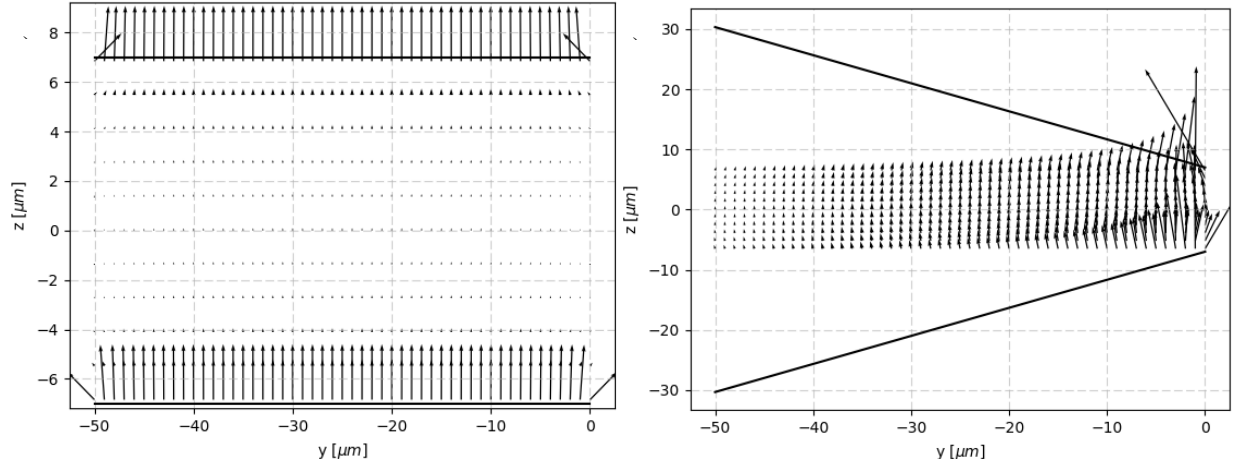


Figure 28: Electric field vectors between electrodes with plate angle (a) $\theta = 0^\circ$ and (b) $\theta = 25^\circ$

In Figure 29, contours of the electric field along the centerline and $3 \mu\text{m}$ above and below the centerline are plotted versus the distance along the axis of the injector. E_z and E_y are the electric field components in the z - and y -directions, respectively. The dotted red line in Figure 29 shows that the y -component of the electric field along the axis of the injector is zero for the whole axis. This is expected because as the electric field lines curve from one electrode to the other, they are perpendicular to the centerline axis of the injector at the centerline. The off-axis y -components of the electric field contour show that there is a transition region where the electric field reverses direction inside the injector (yellow dotted line and black dot-dash line at $y \approx -4.5 \mu\text{m}$). This phenomenon poses a potential problem because the gradient of the electric field also changes sign (observe the slope of the yellow dotted line and black dot-dashed line for $-15 \mu\text{m} < y < -5 \mu\text{m}$) which could indicate a trapping region for the nanoparticles if pDEP is utilized. The transition region is also visible in the slope of the off-axis contours of the z -component of the electric field (blue solid, red dot-dot, and cyan dash lines for $-7.5 \mu\text{m} < y < -2.5 \mu\text{m}$).

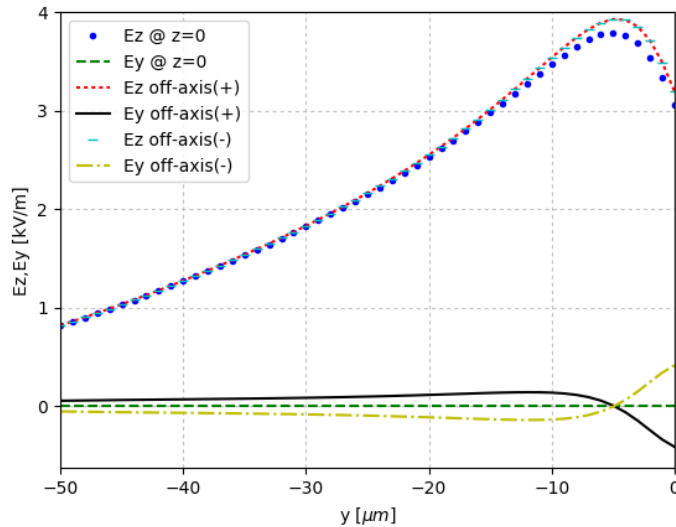


Figure 29: Axial and transverse electric field line contours between angled electrodes

As stated previously, the DEP force is calculated from the gradient of the magnitude of the electric field. Figure 30 contains contour plots of the gradient in the (a) y-direction and (b) z-direction (the signed natural logarithm is used to create a higher contrast visual of the data) and Figure 30(c) is a line contour of the characteristic force along the axis of the injector. The characteristic force is the DEP force divided by the cubed radius of the nanoparticles such that Equation (8) becomes Equation (17) with units of N/m^3 . ϵ_m , the dielectric permittivity of the surrounding medium, is set to $8.854 \times 10^{-12} \frac{s^4 A^2}{m^3 kg}$, the permittivity of free space. ϵ_p , the dielectric permittivity of the particles, $23 \times 10^{-12} \frac{s^4 A^2}{m^3 kg}$.

$$\frac{\vec{F}_{DEP}}{R^3} = 2\pi\epsilon_m k \nabla(|\vec{E}|)^2. \quad (17)$$

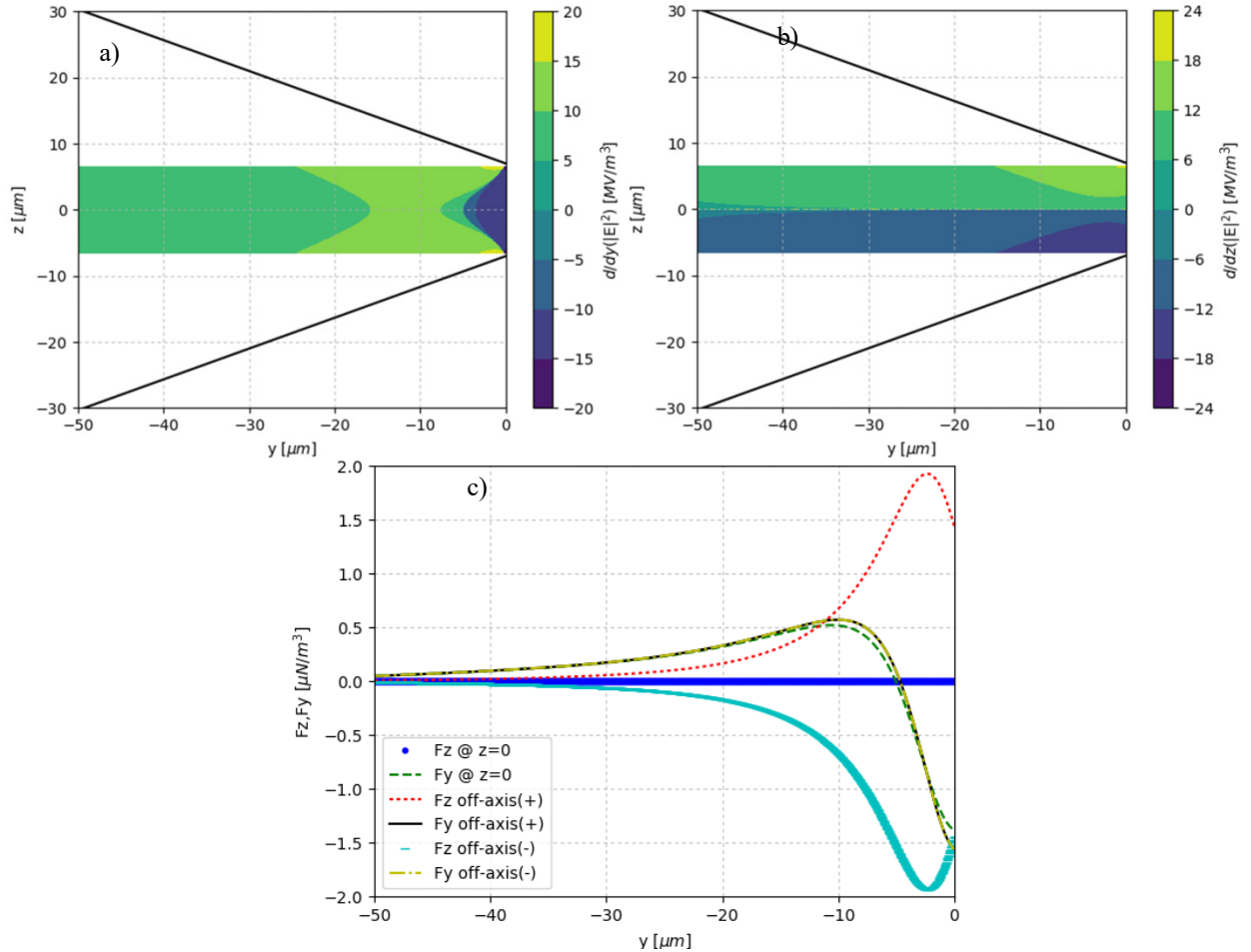


Figure 30: (a) Y-gradient of the magnitude of the electric field, (b) z-gradient of the magnitude of the electric field, (c) DEP force profile along axis of angled electrodes (at the centerline and $\pm 3 \mu m$ off the centerline) (plate angle 25°)

The force in the y - and z -directions at three values of $z = 0, 3, -3 \mu\text{m}$ are plotted in Figure 30 (c). F_y for all three z values begins positive and then goes negative near $y \cong -5 \mu\text{m}$. Studying the y -gradient of the electric field magnitude indicates that this behavior is expected because following the gradient from left to right in Figure 30 (a), along the axis, one sees that the gradient begins positive, increases, then decreases and goes negative. The force is proportional to this profile as shown in Equation (17). Contrary to F_y , F_z behaves differently for each z value. When $z = 0 \mu\text{m}$ the force in the z -direction is also zero along the entire axis because the z -gradient of the electric field magnitude crosses an inflection point in this location. When $z = 3 \mu\text{m}$ the z -gradient is positive which shows the electric field increasing toward the electrode as the $1/r^2$ dependence indicates it should. Increasing y position effectively brings the electrode closer to the $z = 3 \mu\text{m}$ line which also follows the $1/r^2$ dependence and we see a corresponding increase in F_z . When $z = -3 \mu\text{m}$, F_z mirrors the behavior of F_z when $z = 3 \mu\text{m}$. The force is negative, pointing along the gradient directed towards the lower electrode.

2.3.3 Parametric analysis of the dielectrophoretic injector

A parametric analysis was performed to develop a more comprehensive understanding of the dependence that the DEP force has on the plate angle, θ , of the charged plates as well as their separation distance, g . In Figure 31 (a) the largest force magnitude produced in the y -direction (positive or negative) within the guide sleeve is plotted for three electrode plate separation distances and various plate angles. This value is determined for each plate angle by calculating the maximum of the absolute value of the force in the y -direction then re-introducing the sign of the force value so as not to lose information regarding which direction the maximum force acts. Figure 31 (b) indicates the average force in the y -direction, calculated as the statistical mean of F_y within the entirety of the guide sleeve area, and (c) shows the associated standard deviation from that statistical average.

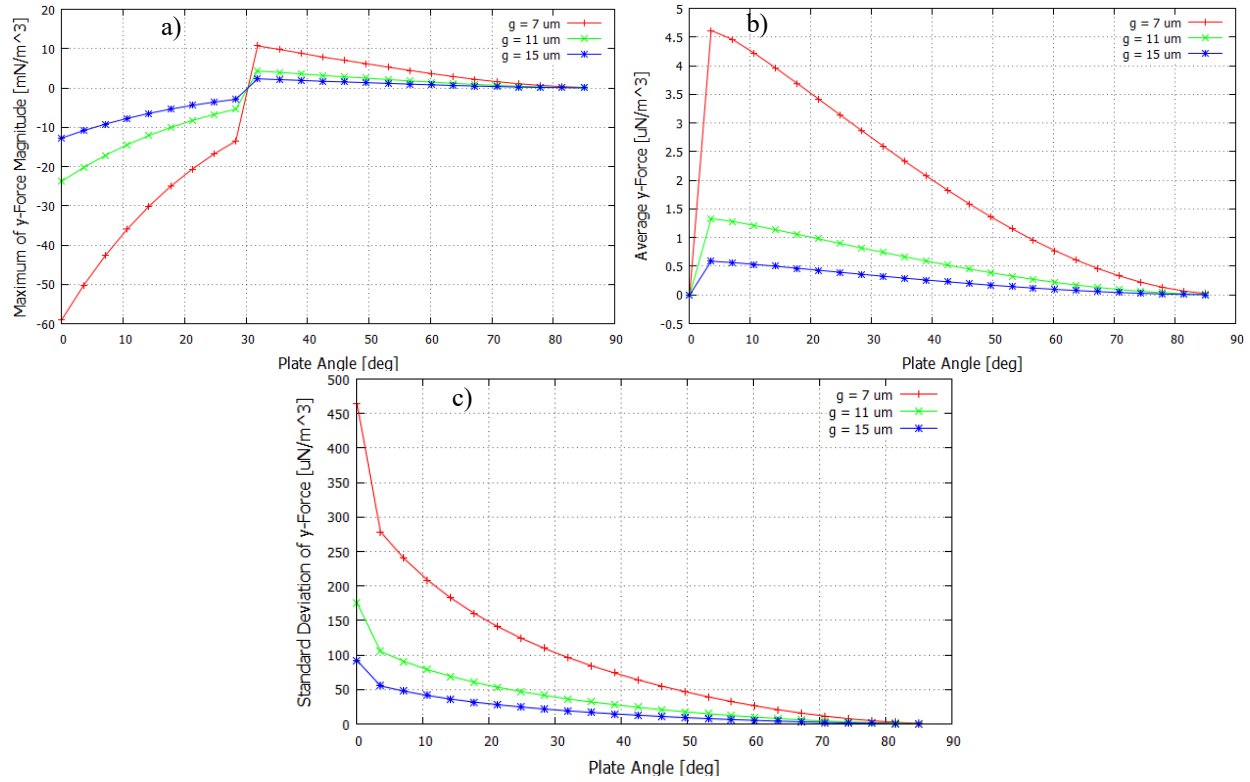


Figure 31: (a) Maximum force magnitude in the y-direction, (b) average force in the y-direction, (c) standard deviation of the force in the y-direction; (a), (b), and (c) each vs. plate angle and separation distance of the guide sleeve within the gap of the DEP injector

Addressing the separation distance, g , the maximum y-force magnitude plotted in Figure 31 (a) increases as g decreases. The discontinuity at 30° occurs when the positive values of the gradient of the electric field become stronger in magnitude than the negative gradient values, as explained later in this section. From Figure 30 (a), we expect the magnitude of the force to be greatest where the electric field gradient is strongest, such as in the region that y is between $-5 \mu\text{m}$ and $0 \mu\text{m}$. In this region the gradient is negative which means the force will also point along the negative y-direction as seen in Figure 31 (a) for plate angles less than 30° . For plate angles greater than 30° Figure 31 (a) indicates that the max force is positive in the y-direction. This can be explained by analyzing the field region of the example contour plot shown in Figure 32 (a), for plate angle 35° , near the electrode and at the narrow end of the particle injector where an increase in the strength of the positive gradient of the field occurs (annotated in Figure 32 (a)).

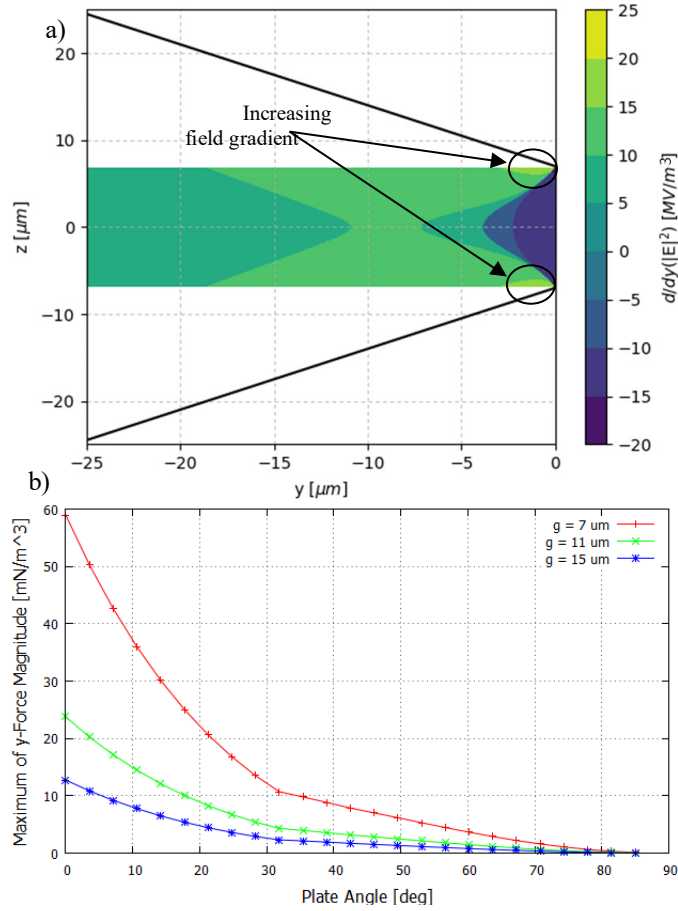


Figure 32: (a) Y-gradient of the magnitude of the electric field (plate angle 35°), (b) maximum force magnitude in the y-direction

The positive gradient values in the Figure 32 (a) contour increase by $\sim 5 MV/m^3$ when compared to the positive gradient values in the plot in Figure 30 (a). (The light green contour represents values $15-20 MV/m^3$ and the yellow contour $20-25 MV/m^3$ versus the previous plot of light green $10-15 MV/m^3$ and yellow $15-20 MV/m^3$). This makes the largest positive gradient greater than the smallest negative one such that the maximum force magnitude in the y-direction for plate angles greater than 30° is positive. The piece-wise step from negative to positive max force values, though interesting, is not the important information from Figure 31 (a). Converting the data from Figure 31 (a) into the simple, unsigned magnitude of the maximum y-force versus plate angle and plotting it in Figure 32 (b) indicates that, as the plate angle increases, the gradient, and thus the force in the y-direction, decreases in strength. The above analysis of the maximum y-force magnitude indicates that small plate angle and narrow plate separation distance are preferable in order to generate strong DEP force fields.

Analysis of the average y-force plotted in Figure 31 (b) indicates the same conclusion. As the plate angle increases, the regions where the electric field gradient is strongest decrease in size which can be seen by comparing Figure 30 (a) to Figure 32 (a). The strong positive gradient region between $y = -25 \mu m$ and $-2 \mu m$ in Figure 30 (a) decreases in size to a region between $y = -18 \mu m$ and $-2 \mu m$ in Figure 32 (a) while simultaneously maintaining strength at $\sim 10 MV/m^3$. This decrease in region size of the strong gradient brings down the overall average of the electric

field gradient and subsequently the force. We expect the average y-force to be zero, as seen in Figure 31 (b), when the plate angle is zero because any fringe effects at the ends of the charged plates will be equal and opposite when the injector structure is mirrored across the vertical line $y = -25 \mu\text{m}$. The $\theta = 0^\circ$ structure plotted in Figure 28 (a) exemplifies these mirrored fringe effects where it can be seen that the electric field points outward at both ends of the bottom plate and inward at both ends of the upper plate.

Analysis of the y-force deviation from the statistical average plotted in Figure 31 (b) indicates that choosing a larger plate separation distance and larger plate angle will produce a more consistent force field in the y-direction, although, an overall weaker force.

2.3.4 Finite Element Analysis

The analytical solution is used to study particle dynamics within the tilted plate injector. COMSOL Multiphysics numerical models were also developed in order to study more complex electrode geometries and electric field structures. The initial geometry used for the numerical models is composed of the tilted, charged plates and the dielectric guide sleeve that restricts the motion of the nanoparticles. Figure 33 shows a contour plot of the magnitude of the electric field between the two tilted plates. The field structure supports our understanding of the analytically obtained results in Figure 28 (b) wherein the field strength increases towards the narrow end of the injector and near the electrodes. The electric field magnitude at location

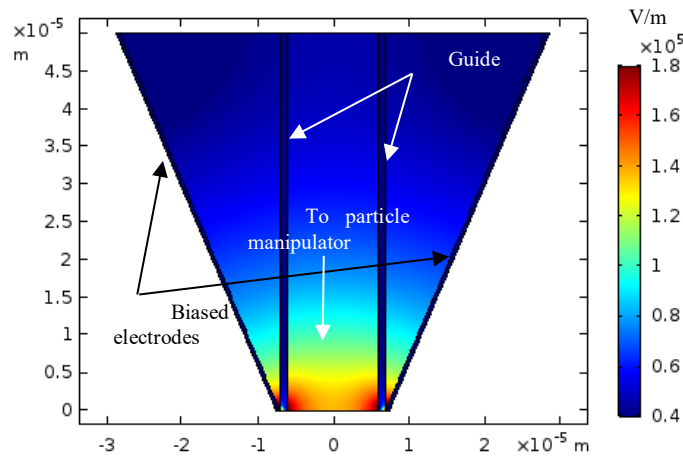


Figure 33: COMSOL Multiphysics model of electric field magnitude in tilted plate injector (injector in this image is rotated 90° clockwise and is pictured with the hollow dielectric guide sleeve)

The perforated exit/inlet membrane that guides the injection of the nanoparticles, indicated in Figure 27, was also included in COMSOL models to determine its affect on the electric field structure. Our design calls for a metallic membrane that acts as a floating potential and shields part of the dielectric guide sleeve from the applied electric field at the location where the electric field gradient changes direction as indicated in Figure 29. A concern we have with this membrane is that the electric field will reduce to zero too quickly at the location of the perforations and the resultant gradient will create a strong DEP force acting against the motion of the nanoparticles. Figure 34 shows the force field contours for the tilted plate injector with a perforated metallic membrane acting as a floating electrical ground. The perforations in the membrane are

perpendicular to the axis of the injector and act as a gate through which the nanoparticles pass. From this contour plot, we see that the presence of the metallic membrane does create force acting against the motion of the particles (the red/orange/yellow bulge in the center of the plot, focused at the perforated membrane).

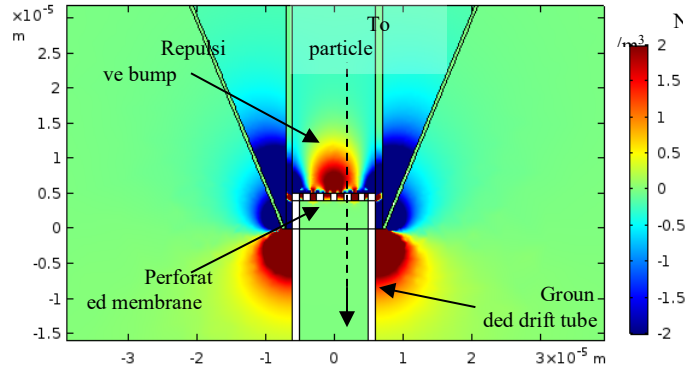


Figure 34: COMSOL Multiphysics model of force field in tilted plate injector with dielectric guide sleeve and metallic perforated membrane as floating ground

The DEP force depends on the relative polarizability of the nanoparticles to the surrounding medium which is vacuum, as stated earlier. This means that the dielectric constant of the nanoparticles is greater than the dielectric constant of the medium, vacuum, and the DEP force takes on the sign of the gradient of the electric field magnitude. If the medium had a dielectric constant that was greater than that of the nanoparticles then the DEP force would be the negative of the sign of the gradient in the electric field magnitude. Therefore, a possible solution to the strong negating force issue that the perforated membrane poses is to suspend the nanoparticles in a liquid such as water ($\epsilon_m = 710 \times 10^{-12} \frac{s^4 A^2}{m^3 kg}$) rather than vacuum ($\epsilon_m = 8.854 \times 10^{-12} \frac{s^4 A^2}{m^3 kg}$). The resulting force field contour of the tilted plate injector that is filled with water and has a dielectric guide sleeve and a metallic perforated membrane is plotted in Figure 35. This contour shows that the repulsive hump seen in Figure 34 now becomes an accelerating ramp that assists the motion of the nanoparticles.

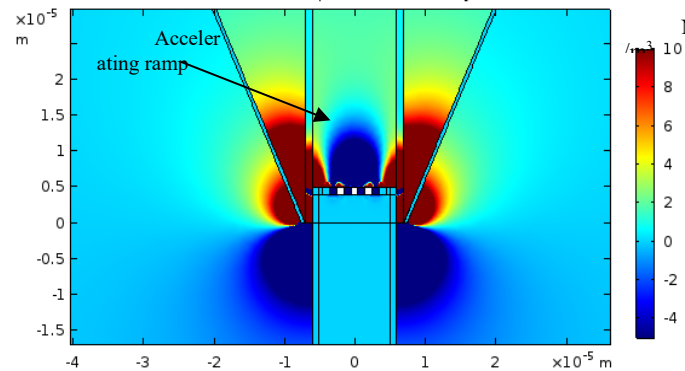


Figure 35: COMSOL Multiphysics model of force field in tilted plate injector with water as the suspension material, a dielectric guide sleeve, and a metallic perforated membrane as floating ground

2.3.5 Particle dynamics in the DEP injector

The injection rate, in particles per second, needs to be calculated in order to determine the thrust profile of the system. The propellant consists of nanoparticles whose motion can be analyzed by using a particle dynamics simulation. For simplicity and to reduce computation time, all simulations are performed on a 2-dimensional slice of the injector-thruster geometry, Figure 27. The motion of each particle is Newtonian in nature. All collisions are approximated as elastic with coefficients of restitution as $COR_w = 0.7$ and $COR_p = 0.65$ for particle-wall and particle-particle collisions, respectively.^{38,39} The coefficient of restitution approximates the kinetic energy that is lost to the wall or another particle during a collision. When a particle-particle collision occurs, the pre-collision state vectors of each particle are combined with the conservation of momentum and energy to define the post-collision state vectors such that the post-collision velocities can be determined, Equations (18) – (21). The subscripts 1 and 2 differentiate the particles involved in the collision. u indicates the pre-collision velocity whereas v indicates the post-collision velocity. θ defines the angle between a reference coordinate frame and a body-centered coordinate frame for which the x-axis is collinear with the center of mass of both colliding particles.

$$v_{1,x} = COR_p \left(u_{2,x} \cos^2 \theta + u_{1,x} \sin^2 \theta + \sin \theta \cos \theta (u_{1,y} - u_{2,y}) \right) \quad (18)$$

$$v_{1,y} = COR_p \left(u_{1,y} \cos^2 \theta + u_{2,y} \sin^2 \theta + \sin \theta \cos \theta (u_{1,x} - u_{2,x}) \right) \quad (19)$$

$$v_{2,x} = COR_p \left(u_{1,x} \cos^2 \theta + u_{2,x} \sin^2 \theta + \sin \theta \cos \theta (u_{2,y} - u_{1,y}) \right) \quad (20)$$

$$v_{2,y} = COR_p \left(u_{2,y} \cos^2 \theta + u_{1,y} \sin^2 \theta + \sin \theta \cos \theta (u_{2,x} - u_{1,x}) \right) \quad (21)$$

A particle-wall collision is defined by a basic recoil approximation where the particle velocity parallel to the wall is unchanged during the collision and the particle velocity perpendicular to the wall becomes negative of what it was and is reduced by the coefficient of restitution. Equation (22) gives an example of the final velocity components for a particle after a particle-wall collision for a wall perpendicular to the y-axis.

$$v_{y_f} = -COR_w (v_{y_i}); v_{x_f} = v_{x_i} \quad (22)$$

The particle locations and velocities are iteratively determined as time progresses in the simulation with time step equal to 100 ns as shown in Equations (23) - (26).

$$y_i = y_{i-1} + v_{y,i-1}t_{step} + \frac{1}{2}gt_{step}^2. \quad (23)$$

$$z_i = z_{i-1} + v_{z,i-1}t_{step}. \quad (24)$$

$$v_{y,i} = v_{y,i-1} + gt_{step}. \quad (25)$$

$$v_{z,i} = v_{z,i-1}t_{step}. \quad (26)$$

The step size is chosen small enough to prevent the occurrence of multiple particles occupying the same physical space after they move during an iteration. The nanoparticle propellant is considered to be settled when the mean velocity of all particles is less than 500 $\mu\text{m/s}$. This ensures that the location of each particle changes by less than $v_{par}t_{step} = 0.05 \text{ nm}$ on average between two time steps (this corresponds to a change in location of less than 0.1 % of the 50 nm radius of the nanoparticles). Simulating large systems of particles can be cumbersome and highly costly in terms of computation time. Therefore we track the motion of a small ($N_p \sim 10^2$) number of particles, which greatly reduces computation time, and then extrapolate the characteristics to a larger system. Figure 36 shows an example particle distribution where the randomly distributed initial positions are plotted in (a) and the final positions, after the particles have settled against the exit interface to the right of the plot, are in (b).

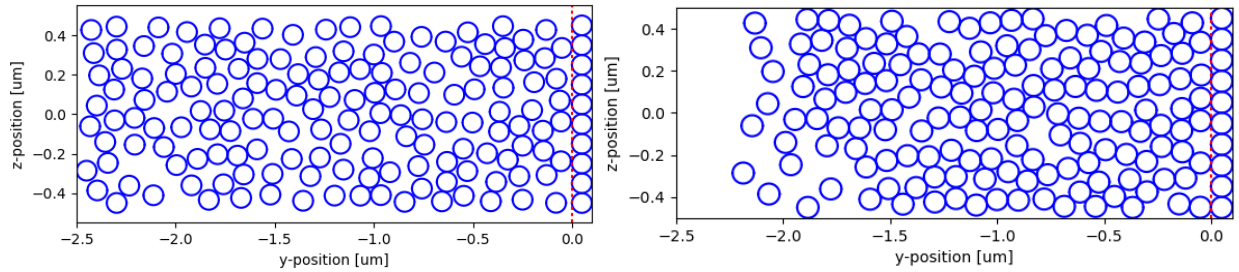


Figure 36: Initial (a) and final (b) positions of propellant particles for particle dynamics simulation.

Two tests cases were run in which the relative radius of the particle to holes was varied and the number of particles emitted per iteration were determined which should reflect that variation. If the radius of the particles is greater than the radius of the exit holes then we expect no propellant to leave the injector. As expected, no particles exit the injector, Figure 37 (a). For the second test, we set the entire face of the exit plane as open, therefore if a particle would “strike” this plane it *will* exit the injector. As shown in Figure 37 (b), the maximum number of particles, five (based on the width of the exit and the size of the particles for this simulation), exit per time step for the entire operating time until the number of particles decreases. All further simulations are conducted with a hole radius set to five times that of the particle radius. (This value is determined by the critical radius which defines the ratio of hole radius to particle radius for which clogging does not

occur due to arch structures developing in the granular material above a hole location. To prevent clogging the hole radius should be approximately 4.94 times that of an individual particle, for spherical particles.⁴⁰⁻⁴²⁾

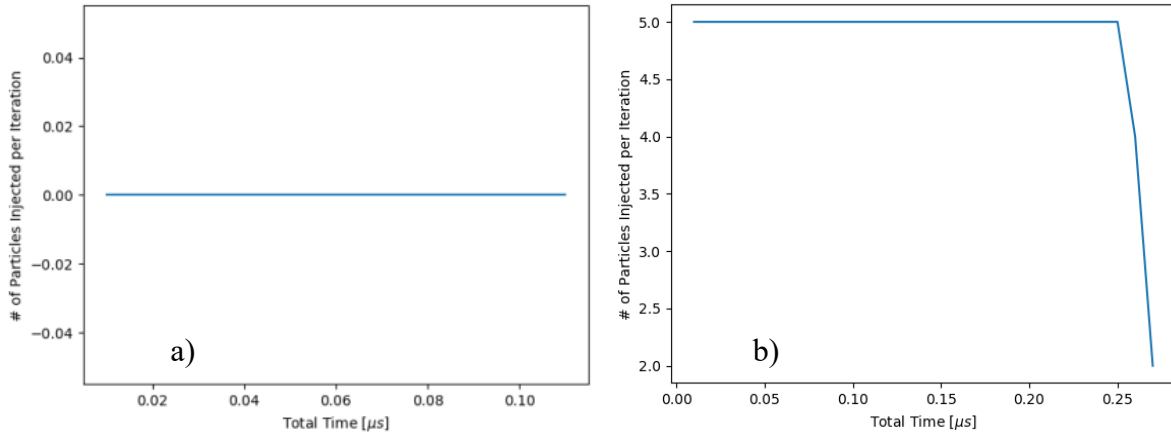


Figure 37: Number of particles exiting versus time. (a) radius of particles greater than radius of exit holes. (b) exit interface completely open

When the propellant exits the injector, the velocity (specifically in the axial/y- direction) is recorded so that the thrust generated by the injector can be calculated. Once the propellant exits the injector it drifts for a short distance through a guide tube until it reaches the plasmonic thruster where it undergoes propulsive acceleration.

Figure 38 shows the average exit velocity that a particle has when it exits the injector and begins drifting toward the thruster versus the time step/iteration at which the particle exited. We assume that the velocity perpendicular to the axis is negligible compared to the velocity in the direction of the axis.

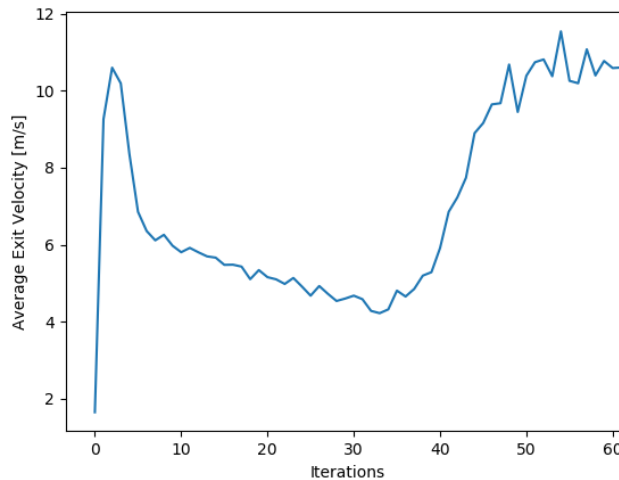


Figure 38: Average exit velocity in y-direction for each iteration in the simulation

Studying Figure 38 shows that the first particles to exit start from rest (a required condition), then after an initial spike in the exit velocity, there is a semi-steady state region between iteration 5 and 25 where the particles move, on average, in unison toward the exit plane. After this, at high iterations, we see that the exit velocity increases drastically. We think this is due to a decreased number of collisions in the propellant as the number of propellant particles has greatly diminished by this time as shown in Figure 39. With so few particles left in the injector, the remaining particles are able to build up high velocities before they interact with the exit plane and exit to the thruster or rebound.

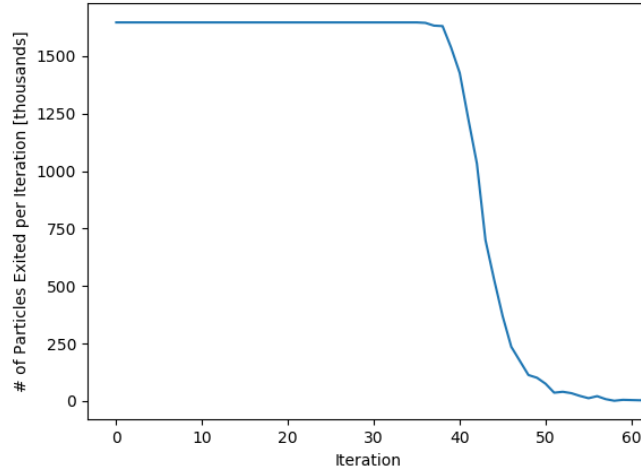


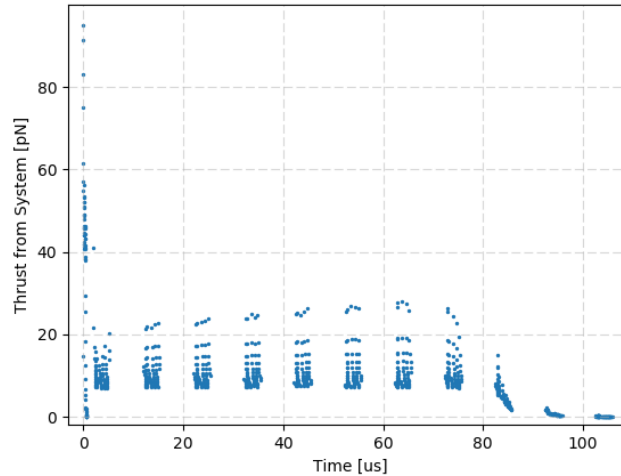
Figure 39: Number of propellant particles exiting the injector per iteration in simulation

The system thrust is defined as the time-dependent thrust produced by the coupled dielectrophoretic injector and plasmonic thruster. We have found that simulating a system with few particles (to reduce computation time) leads to a fast depletion of the propellant reserves. The thrust profile from the plasmonic thruster is calculated by iteratively determining the velocity for the propellant at each acceleration stage of the thruster as the propellant travels through the thruster. By iteratively determining the velocity of the propellant, we can calculate the thrust produced by each stage of the thruster assembly and record it as a function of time by multiplying the mass flow rate times the difference between the velocity of the propellant as it exits one nano-unit stage with the velocity it had when entering the stage. During this iterative process, we assume that the propellant is in-phase with the pulsed light source that dynamically excites the plasmonic thruster. This method produces an upper estimate of the thrust generated by the thruster because it does not account for propellant that may be out-of-phase with the pulsed light.

The thrust profile for an example system is given below in Table 3 and Figure 40. We see the initial impulse from the injector that occurs between 0 and 0.5 μs followed by the short region of zero thrust that indicates the particles are drifting to the thruster. After this we observe the spikes in the thrust profile that define the propellant motion through the thruster.

Table 3: Particle system attributes to determine the generated thrust

Simulated Particles:	72,050
Mass of Propellant:	2.8035e-18 kg
Shutter Speed of Pulsed Light:	10 μ s
Length of Plasmonic Thruster:	2 mm

**Figure 40: Thrust profile of the coupled injector-plasmonic thruster system.**

2.3.6 DEP Injector Conclusions

We have investigated a dielectrophoretic nanoparticle injection mechanism that can couple with a photonic acceleration/manipulation platform. The injector consists of tilted plates that are electrically isolated and charged to maintain a steady, nonuniform electric field across a vacuum or liquid-filled gap. We have analytically and numerically modeled the electric field and dielectrophoretic force within the space between the tilted plates. Our results indicate that an injector with small plate angle, $\theta = 3.5^\circ$, and narrow plate separation distance, $g = 7.0 \mu m$, will produce stronger DEP force fields than an injector with large plate angle, $\theta \cong 82^\circ$, and wide separation distance, $g = 15 \mu m$. This selection will provide a maximum y-force magnitude of $50 mN/m^3$ and an average y-force of $4.6 \mu N/m^3$. We also conclude that choosing small $\theta = 3.5^\circ$ and $g = 7.0 \mu m$ will increase the amount by which the fields vary and deviate from the average within the guide sleeve such that the standard deviation of the y-force is $280 \mu N/m^3$. We conclude that the nanoparticles must be suspended in a medium with dielectric constant greater than that of the nanoparticles so that the metallic membrane acting as a floating potential and gate will aid their motion and not hinder it. Furthermore, we developed a particle dynamics model to calculate the thrust produced by the system and found that the thrust was non-uniform over the acceleration period. It produced a total amount of thrust on the order of 550 pN over a time period of 100 μ s for a simulated system of 72,050 particles.

2.4 Specific Objective 4: Precision Pointing Capabilities Applied to the Control of Microsatellite Swarms

This work can be found in the appendix document.

3 Conclusions

Results for the experimental observation of the plasmonic force acting on nanoparticles are very exciting. A big step has been taken in realizing the plasmonic force propulsion concept with the measurement of particles driven away from an illuminated plasmonic triangle hole array. With this experiment we have successfully observed the acceleration and manipulation of particles using an asymmetric nanostructure sample via strong gradient optical forces. Additionally, we measured the optical forces acting on the particles within the range of 0.03 to 0.18 pN using a 5 mW laser beam.

The dielectrophoretic injector which can couple to the plasmonic force propulsion thruster consists of electrically isolated tilted plates, charged to maintain a steady, nonuniform electric field across a vacuum or liquid-filled gap. Our numerical modeling results indicate that a narrowly spaced injector with a shallow tilt angle will produce stronger DEP force fields than wide and/or sharply angled plates. Optimization of the dielectrophoretic injector enables us to better prepare for the development of a laboratory sample and testing apparatus to gather experimental data for the propellant feed system. Results indicate that the system will work best if the nanoparticle propellant is carried in a high dielectric medium.

Furthermore, our particle dynamics model which determined the thrust produced by the system for a small sample size of propellant indicated that thrust of approximately 550 pN over a time period of 100 μ s is achievable. This supports our previous results that plasmonic force propulsion can significantly enhance the state-of-the-art in small spacecraft position and attitude control by 1-2 orders of magnitude.

Using a set of mission concepts which require swarm formation in a deep space environment, we demonstrated through extensive orbital dynamics calculations that plasmonic force thrusters are feasible as propulsion systems for small satellite clusters. They successfully control attitude in both regulation and tracking cases. With additional modifications to the controller and as a better understanding of the capabilities of the thruster is developed, an overall improved performance can be achieved.

4 Future Work

Future efforts should focus on 1) developing a standalone array of asymmetric nanostructures that can effectively interact with a stream or reservoir of particles or 2) experimentally evaluate a dielectrophoretic injector for nanoparticle propellant. The combination of these future activities would raise the TRL to 4.

The mission specific applications for this concept should be further analyzed with improved controller functionality, better position coordinate formulation, and a general increase in the fidelity of the study. Example missions chosen in the realm of swarm formations in the deep space environment should remain a focus of this concept application.

The evaluation of thrust noise, throttleability, plasmonic sensitivity, and thermal effects on precision pointing capabilities should be expanded by conducting laboratory based experiments on manufactured components and investigating the resultant plasmonic forces acting on nanoparticles. Additionally, more exhaustive testing of nanoparticle manipulation using focused Solar or white light should ensue to better characterize the plasmonic force with uncollimated light.

Lastly, a roadmap should be created for future development of supporting technologies. Supporting technologies necessary for plasmonic propulsion have been investigated here, but a roadmap for future development is necessary. Important supporting technologies include large-

scale nanostructure manufacturing, optical switching technologies (shutters, microblinds with electronic glass), propellant feed system switching (mechanical gate, electro-optical gate).

5 List of Publications Related to this Work

5.1 Journal

- J1. W. Liu, X. Yang, and J. Gao, "Optical transportation and accumulation of micro-particles by self-accelerating cusp beams," *Physical Review A*, 99, 043839 (2019)
- J2. Maser, J.N.* and Rovey, J.L., "Nanoparticle Injector for Photonic Manipulators using Dielectrophoresis," *AIP Advances*, Vol. 9, No. 6, pp. 065109, June 2019.
- J3. W. Liu, J. Gao, and X. Yang, "Optical transportation of micro-particles by non-diffracting Weber beams," *Journal of Optics*, 20, 125401 (2018)
- J4. Maser, J.N.*, Ling, L., Deng, H., Yang, X., and Rovey, J.L., "Transmission Spectrum of Asymmetric Nanostructures for Plasmonic Space Propulsion," *Journal of Spacecraft and Rockets*, Vol. 53, No. 5, pp. 998-1000, Sept. – Oct. 2016.
- J5. Rovey, J.L., Yang, X., Friz, P.D.*, Hu, C., Glascock, M.S.*, "Plasmonic Force Space Propulsion," *Journal of Spacecraft and Rockets*, Vol. 52, No. 4, pp. 1163-1168, July 2015.

5.2 Conference

- C1. Maser, J.N.* and Rovey, J.L., "Dielectrophoretic Nanoparticle Injector for Photonic Manipulator System," *SPIE Defense and Commercial Sensing*, Baltimore, MD, April 14-18, 2019.
- C2. Maser, J.N.* and Rovey, J.L., "Dielectrophoretic Nanoparticle Propellant Injection with Plasmonic Acceleration," *IEEE Research and Applications of Photonics in Defense (RAPID)*, Miramar Beach, FL., Aug. 22-24, 2018 (invited presentation and paper).
- C3. Galchenko, P. and Pernicka, H. J., "Precision Control of Microsatellite Swarms Using Plasmonic Force Propulsion," presented as paper AAS 18-472 at the 2018 AAS/AIAA Astrodynamics Specialist Conference, Snowbird, UT, August 19-23, 2018
- C4. Galchenko, P. and Pernicka, H. J., "Precision Formation Flying and Spacecraft Pointing Using Plasmonic Force Propulsion," presented as paper AAS 17-831 at the AAS/AIAA Astrodynamics Specialists Conference, Stevenson, WA, August 20-24, 2017
- C5. Maser, J.N.*, Rovey, J.L., Yang, X., Li, L., and Deng, H., "Fabrication of Asymmetric Nanostructures for Plasmonic Space Propulsion," AIAA-2016-0696, *54th Aerospace Sciences Meeting*, San Diego, CA., Jan. 4-8, 2016.
- C6. Rovey, J.L., Yang, X., Friz, P.D.*, Hu, C., Glascock, M.S.*, "Plasmonic Force Propulsion for Small Spacecraft," AIAA-2014-3757, *50th Joint Propulsion Conference*, Cleveland, OH., July 28-30, 2014.

6 References

- 1 Juan, M. L., Righini, M. & Quidant, R. Plasmon nano-optical tweezers. *Nature Photonics* **5**, 349-356 (2011).
- 2 Shoji, T. & Tsuboi, Y. Plasmonic optical tweezers toward molecular manipulation: tailoring plasmonic nanostructure, light source, and resonant trapping. *Journal of Physical Chemistry Letters* **5**, 2957-2967 (2014).
- 3 Shalin, A. & Sukhov, S. Plasmonic nanostructures as accelerators for nanoparticles: optical nanocannon. *Plasmonics* **8**, 625-629 (2012).

- 4 Shalin, A. S. Optical accelerator of nanoparticles. *Journal of Communications Technology and Electronics* **56**, 976-984 (2011).
- 5 Maser, J. N., Li, L., Deng, H., Yang, X. & Rovey, J. L. Transmission spectrum of asymmetric nanostructures for plasmonic space propulsion. *Journal of Spacecraft and Rockets* **53**, 998-1000 (2016).
- 6 Bradford, J. in *SpaceWorks*.
- 7 Williams, C., Doncaster, B. & Shulman, J. (SpaceWorks Enterprises, Inc., 2018).
- 8 DelPozzo, S., Williams, C. & Doncaster, B. (SpaceWorks Enterprises, Inc., 2019).
- 9 Micci, M. M. & Ketsdever, A. D. in *Progress in Aeronautics and Astronautics* Vol. 187 (ed Paul Zarchan) (American Institute of Aeronautics and Astronautics, Inc., Reston, VA, 2000).
- 10 NASA. (2011).
- 11 Trauger, J. *et al.* in *SPIE Proceedings, Space Telescopes and Instrumentation 2010: Optical, Infrared, and Millimeter Wave*. 773128.
- 12 Naik, G. V. & Boltasseva, A. Semiconductors for plasmonics and metamaterials. *physica status solidi rapid research letters* **4**, 295-297 (2010).
- 13 Wang, Y., Capretti, A. & Negro, L. D. Wide tuning of the optical and structural properties of alternative plasmonic materials. *Optical Materials Express* **5**, 2415-2430 (2015).
- 14 Abb, M., Albella, P., Aizpurua, J. & Muskens, O. L. All-optical control of a single plasmonic nanoantenna -ITO hybrid. *Nano Lett.* **11**, 2457-2463 (2011).
- 15 Dao, T. D. *et al.* Selective thermal emitters with infrared plasmonic indium tin oxide working in the atmosphere. *Optical Materials Express* **9**, 2534-2544 (2019).
- 16 Maser, J. N., Rovey, J. L., Yang, X., Li, L., Deng, H. in *54th Aerospace Sciences Meeting*. AIAA-2016-0696 edn.
- 17 Eldlio, M., Che, F. & Cada, M. Drude-Lorentz Model of Semiconductor Optical Plasmons. (Springer Science+Business Media, Dordrecht, 2014).
- 18 Zeman, E. J. & Schatz, G. C. An accurate electromagnetic theory study of surface enhancement factors for silver, gold, copper, lithium, sodium, aluminum, gallium, indium, zinc, and cadmium. *Journal of Physical Chemistry* **91**, 634-643 (1987).
- 19 Etchegoin, P. G., Le Ru, E. C. & Meyer, M. An analytic model for the optical properties of gold. *The Journal of Chemical Physics* **125** (2006).
- 20 *Basic Parameters of Gallium Arsenide (GaAs)*, <<http://www.ioffe.ru/SVA/NSM/Semicond/GaAs/basic.html>> (
- 21 *Energy band gap Eg of GaAs*, <https://www.batop.de/information/Eg_GaAs.html> (
- 22 Raymond, A., Robert, J. L. & Bernard, C. The electron effective mass in heavily doped GaAs. *Journal of Physics C: Solid State Physics* **12** (1979).
- 23 Huggard, P. G., Cluff, J. A., Moore, G. P., Shaw, C. J. & Andrews, S. R. Drude conductivity of highly doped GaAs at terahertz frequencies. *Journal of Applied Physics* **87** (2000).
- 24 Askari, H., Fallah, H., Askari, M. & Mohmmadiyeh, M. C. Electrical and optical properties of ITO thin films prepared by DC magnetron sputtering for low-emitting coatings. (2014).
- 25 D'Elia, S. *et al.* Ellipsometry investigation of the effects of annealing temperature on the optical properties of indium tin oxide thin films studied by Drude-Lorentz model. *Applied Surface Science* **255**, 7203-7211 (2009).
- 26 Galca, A. C., Secu, M., Vlad, A. & Pedarnig, J. D. Optical properties of zinc oxide thin films doped with aluminum and lithium. *Thin Solid Films* **518**, 4603-4606 (2010).

- 27 Lai, W.-E., Zhu, Y.-H., Zhang, H.-W. & Wen, Q.-Y. A novel reflector of AZO thin films applicable for terahertz devices. *Optical Materials* **35**, 1218-1221 (2013).
- 28 Hsu, J.-C. & Chen, Y.-Y. Comparison of the optical and electrical properties of Al-doped ZnO films using a Lorentz model. *Coatings* **9** (2019).
- 29 Kaler, K. V. I. S., Prakash, R. & Chugh, D. Liquid dielectrophoresis and surface microfluidics. *Biomicrofluidics* **4** (2010).
- 30 Park, S.-Y., Kalim, S., Callahan, C., Teitell, M. & Chiou, E. A light-induced dielectrophoretic droplet manipulation platform. *Lab on a chip* **9**, 3228-3235 (2009).
- 31 Fan, S. K., Chen, W. J., Lin, T. H., Wang, T. T. & Lin, Y. C. Reconfigurable liquid pumping in electric-field-defined virtual microchannels by dielectrophoresis. *Lab on a chip* **9**, 1590-1595, doi:10.1039/b900790c (2009).
- 32 Wang, K.-L., Jones, T. B. & Raisanen, A. Dynamic control of DEP actuation and droplet dispensing. *J. Micromech. Microeng.* **17**, 76-80 (2007).
- 33 Gunji, M., Jones, T. B. & Washizu, M. Dielectrophoretic microfluidic devices.
- 34 Rovey, J. L., Friz, P. D., Hu, C., Glascock, M. S. & Yang, X. Plasmonic force space propulsion. *Journal of Spacecraft and Rockets* **52**, 1163-1168 (2015).
- 35 Pethig, R. Review article—dielectrophoresis: status of the theory, technology, and applications. *Biomicrofluidics* **4**, 022811, doi:10.1063/1.3456626 (2010).
- 36 Duff, J. D. *Dielectrophoretic precipitation of airborne particles* M. Eng. thesis, University of Louisville, (2013).
- 37 Sagar, A. & Rose, R. in *26th Aerospace Sciences Meeting Aerospace Sciences Meetings* (American Institute of Aeronautics and Astronautics, 1988).
- 38 Constantinides, G. *et al.* Quantifying deformation and energy dissipation of polymeric surfaces under localized impact. *Materials Science and Engineering A* **489**, 403-412 (2008).
- 39 Whitaker, S. M., Sacco, C. & Bons, J. P. in *AIAA SciTech Forum* (AIAA, National Harbor, MD, 2014).
- 40 Wen, P., Zheng, N., Nian, J., Li, L. & Shi, Q. Flux of granular particles through a shaken sieve plate. *Scientific Reports* **5** (2015).
- 41 Chen, K. *et al.* Flux through a hole from a shaken granular medium. *Physical Review E* **74** (2006).
- 42 Zuriguel, I., Garcimartin, A., Maza, D., Punaloni, L. & Pastor, J. Jamming during the discharge of granular matter from a silo. *Physical Review E* **71** (2005).

Appendix: Specific Objective 4

Application of Plasmonic Force Propulsion for Precision Control of Microsatellite Swarms

INTRODUCTION

Swarm formation missions provide the opportunity to develop and execute advanced mission concepts that can be realized through the microsatellite platform. Through coordination, individual microsatellites perform specific functions to execute advanced mission concepts by the swarm. The advancement and rapid growth of the microsatellite platform have greatly expanded hardware capabilities, allowing for the development and application of the microsatellite architecture to deep space missions.

A number of advanced mission concepts have been studied that require swarms with precision formation flight in a deep space environment. Planet finding missions such as the Terrestrial Planet Finder (TPF)¹ and Darwin² seek to create infrared interferometers using a swarm of spacecraft with individual telescopes to emulate a larger and more powerful telescope. Missions like the Micro-Arcsecond X-Ray Interferometry Mission (MAXIM)³ seek to gain a better understanding of the universe by observing and studying black hole phenomena. The Laser Interferometer Space Antenna (LISA) mission, a collaboration between ESA and NASA, will use three spacecraft in a triangular formation flight, separated from each other by approximately 2.5 million kilometers, to create an interferometer to study gravitational waves by measuring the stretching and squeezing of space-time.⁴ Another advanced mission concept that could benefit from the microsatellite platform is the NASA Stellar Imager. The mission proposes to use a swarm of 20 to 30 microsatellites, each fitted with individual mirrors, to fly in a virtual parabolic structure to enable stellar observations.⁵ Through precision formation flying, the swarm of microsatellites in the virtual structure can emulate varied optical focal lengths, providing the opportunity to observe stellar surfaces and interiors. By utilizing the microsatellite architecture, large apertures can be achieved that typical monolithic spacecraft cannot due to Size, Weight, and Power (SWaP) limitations. Each of these unique missions seek to utilize swarms of spacecraft in precision formation flight to enable advanced missions that would otherwise be unfeasible using large monolithic spacecraft.

To execute the scientific objectives of these advanced mission concepts, precision formation flying and pointing are required. For example, missions such as MAXIM require submillimeter⁶ position control, while the Stellar Imager swarm formation requires relative position and pointing control on the order of micrometers and tens of microarcseconds, respectively.⁵ The LISA Pathfinder mission, which successfully completed its flight operations on July 18, 2017, was designed and flown to test some of the key technologies, such as the Space Technology 7 Disturbance Reduction System (ST7-DRS), needed for the upcoming LISA mission.⁷ The ST7-DRS is a propulsion system designed to maintain inertial spacecraft position within two nanometers of nominal, producing up to 30 micronewtons of thrust in increments of 0.1 micronewtons.^{8,9} Work by Marchand and Howell studied a variety of control strategies to quantify propulsion requirements for advanced missions like MAXIM and TPF,¹⁰ showing that thrust levels ranged from nano- to millinewtons for large monolithic spacecraft to achieve submillimeter control. The precise position and pointing criteria required by advanced deep space missions such as Stellar Imager and LISA require micropropulsion with thrust values in the micronewton range, however, as microsatellite capabilities are rapidly progressing, these required micropropulsion technologies are becoming available.^{7,11-13}

Plasmonic Force Propulsion

With the maturity of the microsatellite platform and the rapid development of micropropulsion systems designed for that platform, it is critical that robust and precise guidance and control solutions be developed to enable the use of these technologies in precision formation flying and pointing. This study considers the feasibility of providing precision formation and pointing control using plasmonic force thrusters within the constraints of system-level design requirements of the microsatellite platform. The primary focus of this effort is to evaluate guidance and control solutions using plasmonic force propulsion to provide precision formation and attitude control in a deep space environment such that missions such as LISA and the Stellar Imager can be realized.

Previous Work Related to Plasmonic Force Propulsion

In the first phase of the NIAC research on plasmonic force propulsion, studies showed that layered arrays of nanostructures could generate a total system thrust of 1.6 micronewton.¹⁵ A bang-bang controller was simulated for a 2 kg CubeSat with the PFP system operating at a 1 kHz control rate. The Phase 1 study showed that a pointing accuracy of 10 milliarcseconds could be realized using this propulsion system for attitude control while the spacecraft was subjected to solar radiation pressure perturbations.

In the second phase of the NIAC research,¹⁶ the fidelity of the Phase 1 dynamics and control analysis was increased and the simulation was updated to consider both translational and attitude control, accounting for all six degrees of freedom (DOF). Several mission case studies were analyzed and perturbations were applied to the orbit and spacecraft, testing the developed regulatory and tracking controllers' ability to maintain required position and pointing. It was found that with both controllers, the spacecraft's attitude could be maintained under solar radiation pressure perturbations to within a steady-state error on the order of tens of microarcseconds.

When the regulation and tracking controllers were first selected for the Phase 2 study, integral control action was not considered. It was found, however, that while the controllers were able to rapidly counteract the SRP torque perturbations, the error bounds were about some non-zero steady-state error value. This type of behavior is common among PD-type controllers when unmodeled dynamics or disturbances are present. In Phase 2, it was assumed that the solar radiation perturbation dynamics were unknown to the controller. An integrator term was added to both controllers that bounded the error about zero. While this significantly improved the pointing accuracy of the PFP thrusters, it was found that noise in the system would occasionally lead to unbounded motion after the controller was operating for several hours. It was determined that this was related to integrator windup and that more advanced techniques would need to be used to improve the controller performance.

Previous Work Related to Precision Formation Flying

Libration points, which are derived from three-body dynamics, are of particular interest to advanced deep space missions. These points are locations where, relative to two primary bodies, dynamic forces and acceleration on a spacecraft are at equilibrium as described by the circular restricted three-body problem. Libration points offer many advantages to deep space missions as spacecraft can remain in orbits about these locations with only modest stationkeeping effort. This can facilitate long duration scientific studies of the Earth, Moon, and Sun and allow for enhanced astronomical observation for missions such as the Stellar Imager. While precision formation flight at

these points has been studied, the majority of previous research has been focused on Earth-orbiting spacecraft.

Previous studies of formation flying at libration points have explored impulsive and continuous controllers through the application of linear and nonlinear control techniques, as well as adaptive controllers. Work by Xin showed that by using an optimal nonlinear controller technique, “ θ - D ,” relative position error could be brought to within the sub-millimeter range,^{17,18} while Li used a combination of a linear quadratic regulator and neural network learning to achieve control in the tens of millimeters range.¹⁹ Work by Xu kept formation errors in the subkilometer range, but was also able to estimate the spacecraft mass and bounds of system disturbances using nonlinear adaptive control techniques.²⁰ Queiroz was able to reduce relative errors to the sub-meter range using similar adaptive techniques.²¹ Studies by Gurfil showed that using nonlinear control with neural networks could reduce relative errors to the submillimeter range.²² Impulsive formation control techniques were also studied by Qi, which demonstrated an impulsive control strategy that was able to keep the spacecraft in a bounded relative position error corridor of 100 centimeters.²³

PROPOSED METHOD OF SOLUTION

Three case studies were used to evaluate the performance of PFP thrusters in a deep space environment. The LISA Pathfinder successfully operated in a halo orbit at the L_1 point, while the Stellar Imager mission was designed for an orbit at the L_2 point, both in the Sun-Earth/Moon system. The LISA mission, which was selected for the third large-class mission in ESA’s science program, will operate in a heliocentric orbit trailing behind Earth. By studying the guidance and path planning, it is possible to define nominal orbits that fit within the capabilities of the microsatellite platform while achieving the mission objectives. Robust and precise control techniques allow the individual microsatellites within the swarm to meet the precision relative position formation flight and pointing requirements.

For each of these case studies, the spacecraft are modeled as 12U CubeSats with an array of 24 PFP thrusters. Individual thrusters are capable of producing up to 250 nanonewtons of thrust in 10 nanonewton increments. Multiple control strategies were then applied, assessed, and modified to allow for the implementation of PFP thrusters to maintain the precision position formation flying while providing attitude control. Finally, perturbations were applied to the system along with noise in the performance of the PFP thrusters to assess the robustness of the guidance and control methods.

Case 1

The first case study considered a single microsatellite at the Sun-Earth/Moon L_1 point with the intent of emulating the LISA Pathfinder mission, which provided two nanometers of relative position control. A regulatory attitude controller was used to keep the attitude fixed with respect to the rotating barycentric frame. A desired halo orbit was generated, which can be maintained using standard libration point stationkeeping strategies. A virtual node was placed along the reference trajectory about which the spacecraft maintains its position and attitude. This case study determined if PFP thrusters are capable of maintaining the reference trajectory while regulating attitude under system perturbations and noise.

Case 2

The second case study considered a swarm of multiple microsatellites flying in formation with the intent of emulating the LISA reference orbit. The mission requires a swarm of three spacecraft flying in a triangular formation in an Earth-trailing heliocentric orbit lagging up to 65 million kilometers behind Earth to create a virtual interferometer. A desired trajectory was generated as a reference and propagated forward in time. A virtual triangular structure was placed such that the centroid of the structure lags behind Earth while the three corner nodes of the virtual triangle follow the reference trajectory. Spacecraft are placed at the corner nodes and use a configuration of PFP thrusters to maintain their position and a fixed attitude with respect to the rotating barycentric frame. This case study evaluated the relative position control between the individual microsatellites as well as the ability to track a guidance path while regulating attitude under system perturbations and noise.

Case 3

The final case study considered a swarm of multiple microsatellites flying in formation at the Sun-Earth/Moon L_2 point with the intent of emulating the Stellar Imager mission. The overall design of the system is similar to the second case study, with some modifications to the virtual structure. The mission requires a swarm of up to 30 spacecraft flying in a virtual parabolic structure to create a virtual deep space telescope. The central node of the the virtual parabolic structure was placed on the reference halo orbit trajectory while multiple nodes were generated along the body of the parabolic structure. The spacecraft at these nodes must provide an inertially fixed pointing direction, so the attitude of the spacecraft are time varying with respect to the three-body rotating reference frame, requiring tracking attitude control. This final case study evaluated the relative position control between the individual microsatellites and reference trajectory, while in addition introducing the need for tracking attitude control.

DYNAMIC MODELS

Orbit Dynamics Model

For deep space mission analysis, three-body dynamics is often used, where the primaries are the two dominate gravitational masses and the third mass is the spacecraft of interest. The general three-body problem remains unsolved analytically, and as such simplifying assumptions are typically made. First, it is assumed that the (infinitesimal) mass of the spacecraft does not produce a gravitational force sufficient to affect the motion of the primary gravitational bodies. Second, the two primary gravitational bodies are in circular orbits about the center of mass, the barycenter, lying between the two primary bodies. By defining a rotating frame with the origin at the barycenter such that the \hat{x}_s axis always points toward the secondary body and the \hat{y}_s axis is within the orbital plane, a synodic coordinate frame is formed. By analyzing the dynamics in this way, the classic Circular Restricted Three-Body Problem (CR3BP) is formulated,²⁴ where the equations of motion (EOMs)

are given as

$$\begin{aligned}\ddot{x} - 2\omega_s \dot{y} - \omega_s^2 x &= -\frac{\mu_1(x + r_{B1})}{r_1^3} - \frac{\mu_2(x - r_{B2})}{r_2^3} \\ \ddot{y} + 2\omega_s \dot{x} - \omega_s^2 y &= -\frac{\mu_1 y}{r_1^3} - \frac{\mu_2 y}{r_2^3} \\ \ddot{z} &= -\frac{\mu_1 z}{r_1^3} - \frac{\mu_2 z}{r_2^3}\end{aligned}$$

$$\text{where } r_1 = \left[(x + r_{B1})^2 + y^2 + z^2 \right]^{\frac{1}{2}} \quad \text{and} \quad r_2 = \left[(x - r_{B2})^2 + y^2 + z^2 \right]^{\frac{1}{2}}$$

and where μ_1 and μ_2 are the gravitational parameters of the Sun and Earth/Moon, respectively, r_{B1} is the distance from the barycenter to the Sun, r_{B2} is the distance from the barycenter to the Earth/Moon, and ω_s is the angular velocity of the rotating frame. A graphical representation of the CR3BP is shown in Figure 1.

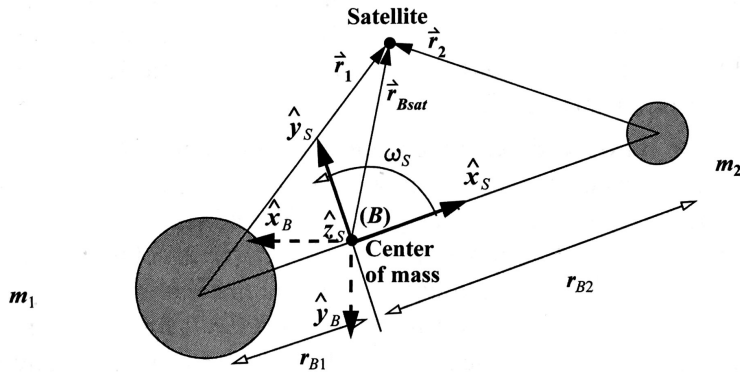


Figure 1: The rotating synodic coordinate frame, $[\hat{x}_s \hat{y}_s \hat{z}_s]$ is defined such that it rotates about the inertially fixed barycenter frame, $[\hat{x}_B \hat{y}_B \hat{z}_B]$, which allows for the simplification of the equations of motion for the spacecraft (image credit Vallado²⁴).

The system is rewritten into first-order form with the addition of translational control and some disturbance such that

$$\dot{\mathbf{x}} = f(\mathbf{x}) + g(\mathbf{x})\mathbf{u} + \delta(\mathbf{x})$$

where

$$f(\mathbf{x}) = \begin{bmatrix} \dot{x} \\ \dot{y} \\ \dot{z} \\ 2\omega_s \dot{y} + \omega_s^2 x - \frac{\mu_1(x+r_{B1})}{r_1^3} - \frac{\mu_2(x-r_{B2})}{r_2^3} \\ -2\omega_s \dot{x} + \omega_s^2 y - \frac{\mu_1 y}{r_1^3} - \frac{\mu_2 y}{r_2^3} \\ -\frac{\mu_1 z}{r_1^3} - \frac{\mu_2 z}{r_2^3} \end{bmatrix} \quad g(\mathbf{x}) = \begin{bmatrix} 0 & 0 & 0 \\ 0 & 0 & 0 \\ 0 & 0 & 0 \\ 1 & 0 & 0 \\ 0 & 1 & 0 \\ 0 & 0 & 1 \end{bmatrix} \quad \mathbf{u} = \begin{bmatrix} u_x \\ u_y \\ u_z \end{bmatrix} \quad \mathbf{x} = \begin{bmatrix} x \\ y \\ z \\ \dot{x} \\ \dot{y} \\ \dot{z} \end{bmatrix}$$

and where \mathbf{u} is the control acceleration from the PFP thrusters and $\delta(\mathbf{x})$ is some disturbance that will perturb the system.

Attitude Dynamics Model

A three-DOF quaternion-based attitude dynamics model was developed for this study that simulates a spacecraft in a deep space orbit. The attitude dynamics are given by

$$\dot{\mathbf{q}} = \frac{1}{2}\Omega(\omega)\mathbf{q}, \quad \Omega(\omega) = \begin{bmatrix} -[\omega \times] & \omega \\ -\omega^T & 0 \end{bmatrix}, \quad J\dot{\omega} = \mathbf{L}_{\text{SRP}} + \mathbf{L}_{\text{control}} - [\omega \times]J\omega$$

where J is the inertia matrix (assumed constant) of the (rigid) spacecraft with respect to the center of mass and in terms of the body-fixed axes, ω is the angular velocity of the spacecraft with respect to the inertial frame, \mathbf{q} is the vector-first quaternion representing the inertially-referenced attitude of the spacecraft, \mathbf{L}_{SRP} is the solar radiation torque perturbation, and $\mathbf{L}_{\text{control}}$ is the applied torque, i.e. the control input.²⁵

Solar Radiation Pressure Dynamics Model

For a spacecraft in a deep space orbit, a significant perturbation may result from solar radiation pressure (SRP). The pressure is modeled with^{24,25}

$$P_{\text{sun}} = \frac{\mathfrak{S}_{\text{sun}}}{c r_{\text{cs}}}$$

where $\mathfrak{S}_{\text{sun}}$ is the solar constant at one astronomical unit, which ranges between 1,361 W/m² and 1,363 W/m² based on the solar cycle, c is the speed of light, and r_{cs} is the distance between the spacecraft and Sun in astronomical units. The spacecraft is modeled as having six uniform sides and the force generated by SRP on the i^{th} side is quantified by

$$\mathbf{F}_{\text{SRP}}^i = -P_{\text{sun}}A^i \left[2 \left(\frac{R_{\text{diff}}^i}{3} + R_{\text{spec}}^i \cos \theta_{\text{SRP}}^i \right) \mathbf{n}_B^i + (1 - R_{\text{spec}}^i) \mathbf{s} \right] \max(\cos \theta_{\text{SRP}}^i, 0)$$

where A^i is the area of the i^{th} side, R_{diff}^i is the coefficient of diffuse reflection, R_{spec}^i is the coefficient of spectral reflection, \mathbf{n}_B^i is the normal outward unit vector of the i^{th} side, \mathbf{s} is the spacecraft-to-Sun unit vector expressed in terms of the body frame, and $\cos \theta_{\text{SRP}}^i = \mathbf{n}_B^i \cdot \mathbf{s}$.^{24,25} The addition of the $\max(\cos \theta_{\text{SRP}}^i, 0)$ term eliminates forces generated on the sides where the normal vector is orientated away from the Sun.

The disturbance forces acting on the sides of the spacecraft from the SRP perturbations are then summed and the disturbance acceleration is given as

$$\delta(\mathbf{x}) = \left[0 \quad 0 \quad 0 \quad \sum_{i=1}^N F_{\text{SRP},x}^i \quad \sum_{i=1}^N F_{\text{SRP},y}^i \quad \sum_{i=1}^N F_{\text{SRP},z}^i \right]^T M_{s/c}^{-1}$$

where N is the number of sides modeled on the spacecraft and $M_{s/c}$ is the mass of the spacecraft. For this study, the spacecraft is modeled as a rectangular prism where $N = 6$.

To quantify how SRP perturbs the attitude dynamics of the spacecraft, the torque generated by SRP is calculated as

$$\mathbf{L}_{\text{SRP}} = \sum_{i=1}^6 \mathbf{r}_{\text{press}}^i \times \mathbf{F}_{\text{SRP}}^i$$

where $\mathbf{r}_{\text{press}}^i$ is the vector from the spacecraft center of mass to the center of pressure of the i^{th} side of the spacecraft.²⁵ This model was simplified by assuming that the center of pressure was on the farthest corner from the geometrical center of the i^{th} spacecraft's side. This generates a *very* conservative worst-case scenario torque about the spacecraft's axes to demonstrate the efficacy of PFP. Of course, in a typical spacecraft, the center of pressure is generally much closer to the geometrical centroid.

CONTROL DESIGN

It is desired that a controller be designed that will allow a spacecraft to maintain its position about some reference, which in this formulation has been defined as a node on a virtual structure that follows some reference trajectory. The original CR3BP system, assuming no perturbations are present, can be written as a simplified two-vector state system as

$$\begin{aligned} \dot{\mathbf{x}}_1 &= \mathbf{x}_2 \\ \dot{\mathbf{x}}_2 &= f_2(\mathbf{x}_1, \mathbf{x}_2) + \mathbf{u} \end{aligned} \quad \text{where} \quad \mathbf{x}_1 = \begin{bmatrix} x \\ y \\ z \end{bmatrix} \quad \mathbf{x}_2 = \begin{bmatrix} \dot{x} \\ \dot{y} \\ \dot{z} \end{bmatrix} \quad \mathbf{u} = \begin{bmatrix} u_x \\ u_y \\ u_z \end{bmatrix}$$

$$\text{and} \quad f_2(\mathbf{x}_1, \mathbf{x}_2) = \begin{bmatrix} 2\omega_s \dot{y} + \omega_s^2 x - \frac{\mu_1(x+r_{B1})}{r_1^3} - \frac{\mu_2(x-r_{B2})}{r_2^3} \\ -2\omega_s \dot{x} + \omega_s^2 y - \frac{\mu_1 y}{r_1^3} - \frac{\mu_2 y}{r_2^3} \\ -\frac{\mu_1 z}{r_1^3} - \frac{\mu_2 z}{r_2^3} \end{bmatrix}$$

while the reference orbit is given by

$$\dot{\mathbf{x}}_{r_1} = \mathbf{x}_{r_2} \quad \text{and} \quad \dot{\mathbf{x}}_{r_2} = f_r(\mathbf{x}_{r_1}, \mathbf{x}_{r_2})$$

where \mathbf{x}_{r_1} and \mathbf{x}_{r_2} are the reference states and f_r represents the desired reference dynamics of the particular case study being considered. The states of the system are then rewritten in terms of the state error as

$$\mathbf{e}_1 = \mathbf{x}_1 - \mathbf{x}_{r_1} \quad \text{and} \quad \mathbf{e}_2 = \mathbf{x}_2 - \mathbf{x}_{r_2}$$

where \mathbf{e} represents the error between the true (simulated) state, \mathbf{x} , and the reference state, \mathbf{x}_r . Using this representation, the error dynamics are then given by

$$\dot{\mathbf{e}}_1 = \mathbf{e}_2 \quad \text{and} \quad \dot{\mathbf{e}}_2 = f_2(\mathbf{x}_1, \mathbf{x}_2) - f_r(\mathbf{x}_{r_1}, \mathbf{x}_{r_2}) + \mathbf{u}$$

which forms the basis for the design of the control methods used in this study.

State Feedback Stabilization

For a linear system described by

$$\dot{\mathbf{x}} = A\mathbf{x} + B\mathbf{u} \quad \text{and} \quad \mathbf{u} = -K\mathbf{x}$$

where A and B are known constant matrices and \mathbf{u} is the state feedback controller, the closed-loop system dynamics of the system are given by

$$\dot{\mathbf{x}} = (A - BK)\mathbf{x}$$

where K is some gain matrix. The origin of the closed-loop system can be shown to be asymptotically stable if the matrix $(A - BK)$ is Hurwitz.²⁶ This is done by choosing the gain matrix K such that the eigenvalues of the closed-loop system lie in the left-half of the complex s-plane. By carefully designing the nonlinear controller, it is possible to make the nonlinear system behave in a similar manner.

For the unperturbed nonlinear system described, a controller is chosen such that

$$\mathbf{u} = -f_2(\mathbf{x}_1, \mathbf{x}_2) + f_r(\mathbf{x}_{r_1}, \mathbf{x}_{r_2}) - \mathbf{k}_1\mathbf{e}_1 - \mathbf{k}_2\mathbf{e}_2$$

where \mathbf{k}_1 and \mathbf{k}_2 are position and derivative controller gain vectors, respectively. The closed-loop system can be reduced to

$$\begin{bmatrix} \dot{\mathbf{e}}_1 \\ \dot{\mathbf{e}}_2 \end{bmatrix} = A_{cl} \begin{bmatrix} \mathbf{e}_1 \\ \mathbf{e}_2 \end{bmatrix} \quad \text{where} \quad A_{cl} = \begin{bmatrix} 0 & 1 \\ -\mathbf{k}_1 & -\mathbf{k}_2 \end{bmatrix}$$

such that if A_{cl} is Hurwitz, then the origin of the unperturbed system will be asymptotically stable. While this method of nonlinear state feedback linearization is used in the initial design of the controller, disturbances and model uncertainties lead to undesired performance in the system. To mitigate this, a robust-adaptive component was added to the control design.

Robust-Adaptive State Feedback Stabilization

While solar radiation pressure perturbations are present in the system, they are unaccounted for in the previous controller formulation, which could result in under performance of the controller. By utilizing Lyapunov redesign and neural networks, an additional robust-adaptive component can be added to the controller that can make the design more robust with bounded uncertainties.

Lyapunov Redesign: For the translational controller, the Lyapunov redesign method was used, which is further elaborated on with proofs in the work by Khalil.²⁶ Given the original first-order form of the system, $\dot{\mathbf{x}} = f(\mathbf{x}) + g(\mathbf{x})\mathbf{u} + \delta(\mathbf{x})$, where $\mathbf{u} = \phi(\mathbf{x})$ is the stabilizing controller determined from the nominal system without disturbances, assume that with $\mathbf{u} = \phi(\mathbf{x}) + \nu$ the uncertain term $\delta(\mathbf{x})$ satisfies the bound

$$\|\delta(t, \mathbf{x}, \phi(\mathbf{x}) + \nu)\| \leq \varrho(\mathbf{x}) + \kappa_0\|\nu\|$$

where ϱ in effect measures the size of the system disturbance. The origin of the perturbed system can then be stabilized by designing ν such that

$$\nu = -\beta(\mathbf{x})\text{Sat}\left(\frac{\beta(\mathbf{x})\omega}{\mu}\right) = \begin{cases} -\beta(\mathbf{x}) \cdot \left(\frac{\omega}{\|\omega\|}\right), & \text{if } \beta(\mathbf{x})\|\omega\| > \mu \\ -\beta^2(\mathbf{x}) \cdot \left(\frac{\omega}{\mu}\right), & \text{if } \beta(\mathbf{x})\|\omega\| \leq \mu \end{cases}$$

$$\text{where } \beta(\mathbf{x}) \geq \frac{\varrho(\mathbf{x})}{1 - \kappa_0} \quad \text{and} \quad \omega^T = 2[\mathbf{e}_1; \mathbf{e}_2]^T P g(\mathbf{x});$$

and where P is calculated from the nominal error system dynamics such that

$$PA + A^T P = -I \quad \text{where} \quad A = \begin{bmatrix} 0 & 0 & 0 & 1 & 0 & 0 \\ 0 & 0 & 0 & 0 & 1 & 0 \\ 0 & 0 & 0 & 0 & 0 & 1 \\ -k_1 & 0 & 0 & -k_4 & 0 & 0 \\ 0 & -k_2 & 0 & 0 & -k_5 & 0 \\ 0 & 0 & -k_3 & 0 & 0 & -k_6 \end{bmatrix}$$

and I is the identity matrix and k_1 through k_6 are the individual controller tuning gains.

To determine the disturbance bounds of $\delta(\mathbf{x})$, a simplified version of the SRP perturbation model²⁴ was used to define an upper bound. Assuming that the largest area, A_m , of the spacecraft is orientated such that the normal is directed toward the Sun and that the surface properties are perfectly reflective to the solar radiation, the acceleration generated by SRP is given by

$$\mathbf{A}_{\text{SRP}} = -2 \frac{P_{\text{sun}} A_m}{M_{s/c}} \frac{\mathbf{x}_s}{\|\mathbf{x}_s\|} = \varrho(\mathbf{x}) \quad \text{such that} \quad \delta(\mathbf{x}) \leq \|\varrho(\mathbf{x})\|$$

where \mathbf{x}_s is the vector from the spacecraft to the Sun. Using this upper bound for the disturbance, the translational controller becomes

$$\mathbf{u} = \phi(\mathbf{x}) + \nu \quad \text{where} \quad \nu = -\beta(\mathbf{x})\text{Sat}\left(\frac{\beta(\mathbf{x})\omega}{\mu}\right) \quad \text{and} \quad \beta(\mathbf{x}) = \|\varrho(\mathbf{x})\|$$

such that the perturbed system can be stabilized. Once $\phi(\mathbf{x})$ was found from the nominal system, the simulation was run and controller gains were tuned. After tuning, the robust component was added and the gains further tuned until desired system performance was achieved.

Neural Network Control: For the attitude dynamics, a neural network (NN) controller was used to demonstrate a robust-adaptive component that can be added to the control design. Considering the unperturbed attitude dynamics given by

$$\dot{\mathbf{q}} = \frac{1}{2}\Omega(\omega)\mathbf{q} \quad \text{and} \quad J\dot{\omega} = \mathbf{L}_{\text{control}} - [\omega \times]J\omega$$

the nonlinear state feedback controller that would regulate the error dynamics of the system can be given through the modification of the well-known regulation controller²⁵ such that

$$\mathbf{L}_{\text{control}} = -k_p \text{sign}(\delta q_4) \delta \mathbf{q}_{1:3} - k_d \omega + [\omega \times]J\omega \quad \text{where} \quad \delta \mathbf{q} = \mathbf{q} \otimes \mathbf{q}_c^{-1}$$

where \mathbf{q}_c is the desired quaternion, $\delta\mathbf{q}$ is the error quaternion, k_p is the proportional gain, and k_d is the derivative gain. As before, because disturbances have not been accounted for in this controller, the unmodeled uncertainties can lead to undesired performance in the system.

Neural networks provide a method of adaptive control with which unmodeled dynamics and disturbances can be estimated and accounted for in the designed controller. A two-layer neural network and controller were chosen with

$$\mathbf{L}_{\text{control}} = -K\mathbf{e} + [\omega \times]J\omega - \hat{f}(\mathbf{z}) \quad \text{where} \quad \mathbf{e} = \omega + \text{sign}(\delta q_4)\delta\mathbf{q}_{1:3}$$

and where K is a gain matrix and $\hat{f}(\mathbf{z})$ is an estimate of the nonlinear dynamics and is determined by

$$\hat{f}(\mathbf{z}) = \hat{W}^T \sigma(\hat{V}^T \mathbf{z})$$

where \hat{W}^T and \hat{V}^T are the weights of the neural network and σ is a basis function. To update the weights of the neural network, an adaptive control algorithm was modified to give

$$\begin{aligned} \dot{\hat{W}} &= M \left(\sigma(\hat{V}^T \mathbf{z}) - \sigma'(\hat{V}^T \mathbf{z}) \hat{V}^T \mathbf{z} \right) \mathbf{e}^T - \kappa M \|\mathbf{e}\| \hat{W} \\ \dot{\hat{V}} &= L \mathbf{z} \mathbf{e}^T \hat{W}^T \sigma'(\hat{V}^T \mathbf{z}) - \kappa L \|\mathbf{e}\| \hat{V} \end{aligned}$$

where M and L are positive definite matrices, κ is a tuning parameter between zero and one, and where the vector of inputs, \mathbf{z} , and activation function, $\sigma(x)$, are given by

$$\mathbf{z} = [q_1 \quad q_2 \quad q_3 \quad q_4 \quad w_1 \quad w_2 \quad w_3]^T \quad \text{and} \quad \sigma(x) = \frac{1}{1 + \exp^{-x}}$$

where the input, x , to the activation function is given as $V^T \mathbf{z}$.

Ensuring the stability of the system, which is not included here for brevity, can be demonstrated through a candidate Lyapunov function and its derivatives such that the error states and weights are bounded.²⁷ This formulation allows the neural network to estimate the perturbations caused by solar radiation pressure even when the SRP dynamics are unmodeled.

REFERENCE TRAJECTORY DESIGN

For each of the case studies, identical translational controller methodologies were used with only modifications to the design of the desired reference trajectory leading to the error dynamics.

Case 1

The halo orbit is a natural orbit that exists within the context of the CR3BP, with stationkeeping methods needing to be applied occasionally to maintain the orbit. While the orbit is “unnatural” in higher fidelity models such as the elliptic restricted three-body problem or an ephemeris-based model, a separate dynamical representation of the reference trajectory is not needed in this study because the system dynamics are modeled as “truth” in the CR3BP. As such, the reference trajectory

is determined using the CR3BP EOMs given by

$$\begin{aligned} \dot{\mathbf{x}}_{r_1} &= \mathbf{x}_{r_2} \\ \dot{\mathbf{x}}_{r_2} &= f_r(\mathbf{x}_{r_1}, \mathbf{x}_{r_2}) \end{aligned} \quad \text{where} \quad \mathbf{x}_{r_1} = \begin{bmatrix} x_r \\ y_r \\ z_r \end{bmatrix} \quad \mathbf{x}_{r_2} = \begin{bmatrix} \dot{x}_r \\ \dot{y}_r \\ \dot{z}_r \end{bmatrix}$$

$$\text{and} \quad f_r(\mathbf{x}_{r_1}, \mathbf{x}_{r_2}) = \begin{bmatrix} 2\omega_s \dot{y}_r + \omega_s^2 x_r - \frac{\mu_1(x_r + r_{B1})}{r_{r_1}^3} - \frac{\mu_2(x_r - r_{B2})}{r_{r_2}^3} \\ -2\omega_s \dot{x}_r + \omega_s^2 y_r - \frac{\mu_1 y_r}{r_{r_1}^3} - \frac{\mu_2 y_r}{r_{r_2}^3} \\ -\frac{\mu_1 z_r}{r_{r_1}^3} - \frac{\mu_2 z_r}{r_{r_2}^3} \end{bmatrix}$$

such that the propagated dynamics of the spacecraft only differ in the addition of a control input and using the true state instead of the reference. The initial conditions for the reference trajectory are numerically computed using the well-known differential corrector approach that generates a halo orbit when propagated forward in time.

Case 2

The LISA mission will use a natural formation orbit determined from the two-body problem. Unlike the CR3BP formulation in this study, the two-body problem only considers a primary gravitational body about which a spacecraft is orbiting. If no perturbing forces are considered in this model, a natural formation can be created by placing spacecraft in a heliocentric orbit with the formation defined on a relatively small unit circle that is inclined 60° to the ecliptic plane, where the orbits are separated from each other by slightly different RAAN values. The LISA mission considers such an orbit where a swarm of three spacecraft is placed in a heliocentric orbit lagging behind Earth.

To generate the reference trajectories, a virtual structure is defined with four nodes: one at the center of an equilateral triangle and three at equidistant locations, separated by 120° on a unit circle. As shown in Figure 2, the three spacecraft are located at each vertex of the triangle with the centroid virtual node orbiting in the ecliptic plane (lagging Earth). This equilateral triangle rotates about its normal axis at the same rate as the Earth orbits the Sun. By inclining the equilateral triangle by 60° to the ecliptic plane, a natural formation occurs in the two-body problem where spacecraft placed at equidistant points about the circle circumscribed by the equilateral triangle remain at a constant separation through time. If the spacecraft kinematics of just the equilateral triangle motion are considered, then the relative velocity and acceleration are given as

$$\dot{\mathbf{r}}_i = \omega_t \times \mathbf{r}_i \quad \text{and} \quad \ddot{\mathbf{r}}_i = \omega_t \times \dot{\mathbf{r}}_i$$

where \mathbf{r}_i is the vector to the i^{th} spacecraft from the triangle centroid and ω_t is the angular velocity about the triangle normal. It should be noted that the simplicity of this formulation is due to the magnitude of the relative position vector being constant with time, the rate of rotation being constant, and being within the reference frame of the equilateral triangle with the origin located at the center of the triangle.

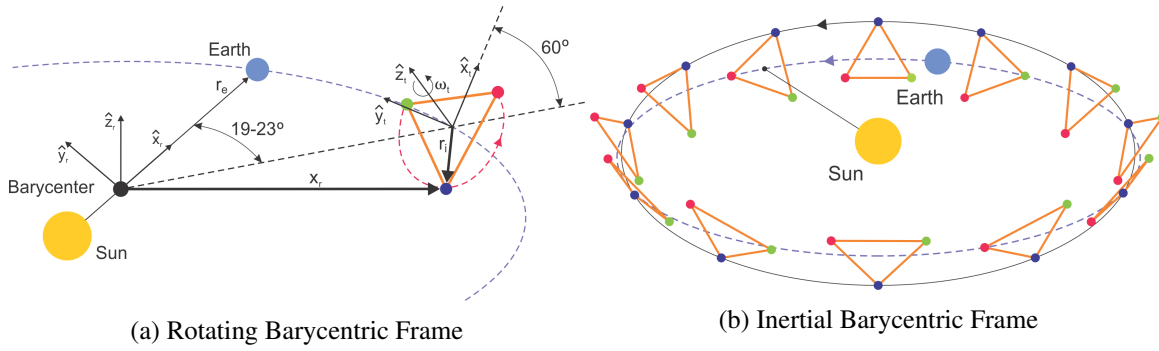


Figure 2: The desired reference orbits of the three spacecraft are given within the framework of the CR3BP and its associated reference frames.

Because the reference trajectory is generated in terms of a different reference frame from that of the system dynamics, a direction cosine matrix (DCM) is used to represent the reference trajectory in terms of the barycentric frame used in the CR3BP, giving the reference trajectory as

$$\mathbf{x}_{r_i} = {}^1[M]^r \left(\mathbf{r}_e + {}^r[N]^t \mathbf{r}_i \right) \quad \dot{\mathbf{x}}_{r_i} = {}^1[M]^r \left({}^r[N]^t \left[\boldsymbol{\omega}_t \times \mathbf{r}_i \right] \right) \quad \ddot{\mathbf{x}}_{r_i} = {}^1[M]^r \left({}^r[N]^t \left[\boldsymbol{\omega}_t \times (\boldsymbol{\omega}_t \times \mathbf{r}_i) \right] \right)$$

where \mathbf{x}_{r_i} is the position of the i^{th} spacecraft in terms of the rotating barycentric frame, \mathbf{r}_e is the position of the Earth in terms of the rotating barycentric reference frame, ${}^r[N]^t$ is the DCM that rotates the equilateral triangle reference frame, $[\hat{x}_t \hat{y}_t \hat{z}_t]$, to the barycentric reference frame, $[\hat{x}_r \hat{y}_r \hat{z}_r]$, and ${}^1[M]^r$ is the DCM that rotates the reference trajectory such that it is lagging behind Earth by 19-23° about the \hat{z}_r axis (such that the centroid remains in the ecliptic plane).

By rewriting this system into first-order form and substituting these reference kinematics into the error dynamics defined for the CR3BP used in this study, the error dynamics become

$$\begin{bmatrix} \dot{\mathbf{e}}_{1_i} \\ \dot{\mathbf{e}}_{2_i} \end{bmatrix} = \begin{bmatrix} \mathbf{e}_{2_i} \\ f_2(\mathbf{x}_{1_i}, \mathbf{x}_{2_i}) - f_r(\mathbf{x}_{r_{1_i}}, \mathbf{x}_{r_{2_i}}) + \mathbf{u} \end{bmatrix} \quad \text{where} \quad \mathbf{e}_{1_i} = \mathbf{x}_{1_i} - \mathbf{x}_{r_{1_i}} \quad \text{and} \quad \mathbf{x}_{r_{1_i}} = \mathbf{x}_{r_i} \\ \mathbf{e}_{2_i} = \mathbf{x}_{2_i} - \mathbf{x}_{r_{2_i}} \quad \mathbf{x}_{r_{2_i}} = \dot{\mathbf{x}}_{r_i}$$

$$\text{and} \quad f_2(\mathbf{x}_{1_i}, \mathbf{x}_{2_i}) = \begin{bmatrix} 2\omega_s \dot{y}_i + \omega_s^2 x_i - \frac{\mu_1(x_i + r_{B1_i})}{r_{1_i}^3} - \frac{\mu_2(x_i - r_{B2_i})}{r_{2_i}^3} \\ -2\omega_s \dot{x}_i + \omega_s^2 y_i - \frac{\mu_1 y_i}{r_{1_i}^3} - \frac{\mu_2 y_i}{r_{2_i}^3} \\ -\frac{\mu_1 z_i}{r_{1_i}^3} - \frac{\mu_2 z_i}{r_{2_i}^3} \end{bmatrix}$$

$$\text{and} \quad f_r(\mathbf{x}_{r_{1_i}}, \mathbf{x}_{r_{2_i}}) = {}^1[M]^r \left({}^r[N]^t \left[\boldsymbol{\omega}_t \times (\boldsymbol{\omega}_t \times \mathbf{r}_i) \right] \right)$$

and thereby allow for the regulation of the spacecraft motion to that of the reference trajectory.

Case 3

Similar to the first case, this study considers a naturally occurring halo orbit in the CR3BP but instead at the Sun-Earth/Moon L_2 point. The virtual structure is expanded to a large number of

spacecraft nodes such that they can be arranged into a virtual parabolic mirror arrangement along with a node defining the centroid of the structure. This central node is placed onto the reference halo orbit, with the orientation of the structure fixed with respect to the rotating barycentric frame. The remaining nodes within the virtual structure are then given some displacement from the centroid, representing the desired placement of spacecraft within the structure. In the case of the Stellar Imager, 20 to 30 spacecraft would be used to create a virtual parabolic mirror. While the reference trajectory for the virtual structure is given as in the first case study, the i^{th} spacecraft error is defined as

$$\mathbf{e}_1^i = \mathbf{x}_1^i - \mathbf{x}_{r_1} - \mathbf{r}_{r_1}^i \quad \text{and} \quad \mathbf{e}_2^i = \mathbf{x}_2^i - \mathbf{x}_{r_2}$$

where \mathbf{x}_r is the state of the central node of the virtual structure in terms of the rotating barycentric reference frame and $\mathbf{r}_{r_1}^i$ is the constant position vector from the central node to the i^{th} node of the structure. As this vector is constant, the error dynamics of the system remain unchanged in the controller formulation and is the same as in the first case study.

RESULTS

For each of the case studies considered, spacecraft were placed at their respective nodes within a virtual structure. To simulate injection noise in the desired position, velocity, and attitude, a random vector taken from the standard normal distribution was applied such that the 3σ value was arbitrarily selected as one meter for position, 100 millimeters per second for velocity, and five degrees for attitude. It was assumed that the initial angular velocity error was zero. These injection errors help demonstrate the PFP thrusters' ability to provide repositioning and reorientation within the virtual structure in addition to counteracting unmodeled disturbances. Finally, noise in the thrusters was modeled, allowing for precision in the ~ 10 s of nanonewtons per single PFP thruster, generating errors up to 4% of the desired thrust values per thruster.

After tuning gains, the performance of the controller using PFP thrusters was determined, which operated at 0.1 Hz, and ΔV budgets were quantified. It should be noted that no stationkeeping methods were applied to the reference halo orbit trajectories of Case 1 and Case 3. Long-term missions will require that stationkeeping methods be used to maintain the reference trajectory, which would incur addition ΔV costs (a large body of literature exists regarding such methods). All translational ΔV budgets given here would be in addition to such stationkeeping strategies applied to the reference orbit.

Case 1

The first and relatively simple case study, a single spacecraft in a halo orbit about Sun-Earth/Moon L_1 , was analyzed to determine the general capabilities of a CubeSat equipped with PFP thrusters. A simple one-node virtual structure was generated such that the node followed a halo reference trajectory and a single 12U CubeSat was placed at the node. With the spacecraft orbit initialized, the system was propagated for a period of several days and the controller gains were tuned until the desired steady state performance was achieved under a range of injection errors.

The performances of the attitude and translational controllers are shown in Figure 3. From these results, it can be seen that both the translational and attitude states reach steady state in several hours. Steady state errors in attitude reached ~ 10 s of microarcseconds, while attitude rate errors were under one microarcsecond per second, with an equivalent total ΔV budget of only 2 meters

per second over a one year period. Steady state errors in translational control were reduced to ~ 10 s of micrometers for position and ~ 100 s of nanometers per second for velocity with a ΔV budget of approximately 1 meter per second for a one year period. It should be noted that limitations in simulation numerics were reached using this controller and it is likely that improved performance is possible, as discussed in the Conclusion section.

Not only was this control method able to regulate the trajectory and attitude of the spacecraft to the desired states, it was also able to regulate it to within the requirements of the advanced mission concepts presented in this study.

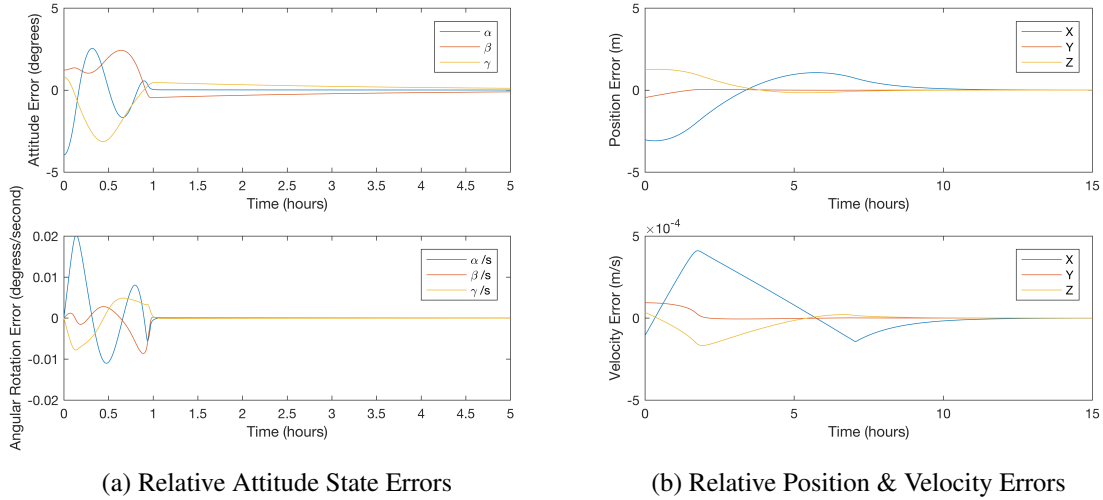


Figure 3: Results show that for Case 1, the robust-adaptive control methods used were able to regulate the spacecraft motion to the desired relative and attitude states under SRP perturbations. Translational errors are defined as deviations from the reference node, and the error angles α , β , and γ are deviations from the desired yaw, pitch, and roll of the spacecraft.

Case 2

The second case study considers a swarm of three spacecraft in a heliocentric orbit lagging behind Earth. A virtual structure is generated with four nodes, one at the center of the triangle and three at equidistant locations, separated by 120° on a unit circle forming an equilateral triangle. A single 12U CubeSat is placed at each of the three corner nodes of the virtual structure, such that the separation between each spacecraft is 2.5 million kilometers.

It was found that the PFP thrusters were unable to provide sufficient thrust to maintain the desired reference trajectory for the 2.5 million kilometer spacecraft separation desired by the LISA mission. The attitude controller however was able to regulate the attitude as desired, as shown in Figure 4. From these results, it can be seen that attitude states reach steady state in several hours. Steady state attitude errors and ΔV are very similar to those of the first case study.

Only by reducing the separation between the spacecraft to 500 km and lowering the injection error by two orders of magnitude could the desired reference trajectory be maintained by the PFP thrusters. The results for translational control at this separation distance are shown in Figure 5. It can be seen that while the reference trajectory is maintained, some chatter is observed in the system.

It was found that while chatter could be reduced through fine tuning of the controller gains, it came with the penalty of larger steady state errors.

The issues encountered in implementing translational control using PFP thrusters stems from the large forces that are required to maintain the orbit. The reference trajectory was designed using a natural formation that is defined in the two-body problem, and as such does not exist naturally in higher fidelity models (i.e., the CR3BP model used here). Furthermore, additional perturbations make it even more difficult to maintain the orbit.

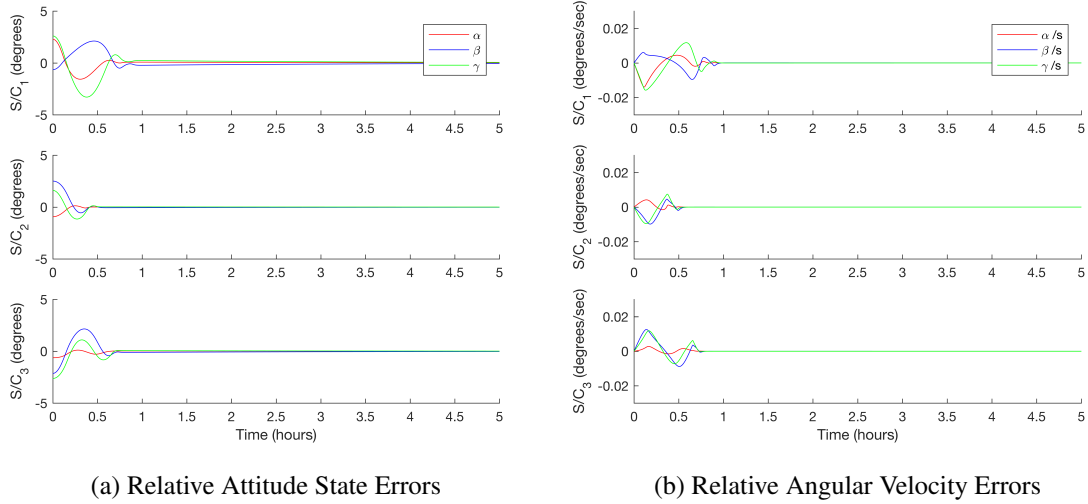


Figure 4: The error in attitude states is quickly regulated by the NN attitude controller for all three spacecraft within the swarm formation needed for the LISA mission.

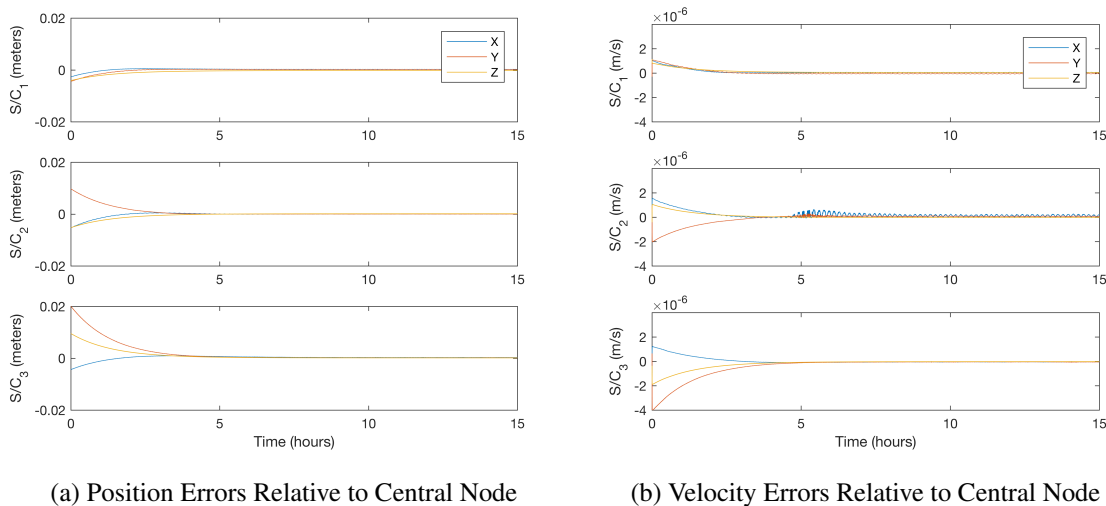


Figure 5: While the reference orbit is maintained using PFP thrusters when the separation is reduced to 500 km, steady state errors are outside the requirements of current mission concepts.

Case 3

The last case study considers a swarm of three spacecraft in an L_2 halo orbit in the Sun-Earth/Moon system. A virtual structure is generated with four nodes, one at the center of the structure and three at 100 meter separation distances from the central node, simulating a portion of a virtual parabolic mirror formation needed for missions such as Stellar Imager. A single 12U CubeSat is placed at each of the three external nodes and injection errors are applied to both translational and attitude states. The spacecraft are commanded to maintain the translational formation while tracking a time varying pointing direction toward the Earth/Moon barycenter throughout the reference orbit. The system was propagated for several days and controller gains tuned to determine the steady state response.

The performance of the attitude and translational controllers is shown in Figure 6 and Figure 7, respectively. Steady state errors were reduced to ~ 100 s of micrometers for position and ~ 100 s of nanometers per second for velocity with a similar ΔV as in Case 1. Steady state errors in attitude reached ~ 10 s of arcseconds, while attitude rate errors were under 10 arcseconds per second. While the performance of the translational controller is similar to that of Case 1, the attitude controller becomes less precise due to the time varying attitude needed to maintain an Earth/Moon pointing orientation throughout the reference trajectory.

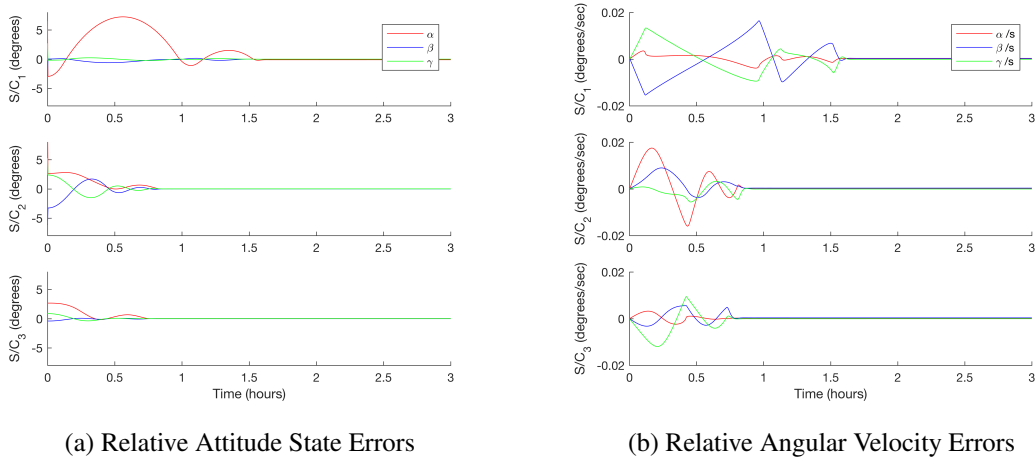


Figure 6: The NN attitude controller is able to point the individual spacecraft toward the Earth/Moon.

To improve the performance of the attitude controller, a reformulation of the attitude error dynamics would be required. In the original formulation, a regulatory controller was used that rotates the attitude toward a desired orientation while reducing the angular velocities to zero. While this is effective in the first two case studies, where the desired attitude orientation does not change, a nonzero angular velocity is desired in the third case where the desired attitude changes throughout the orbit. A desired zero angular velocity was also used for Case 3 because a halo orbit in the Sun-Earth/Moon system takes approximately 180 days to complete one orbit, making the overall angular velocity very small throughout the orbit. However, because the Earth/Moon barycenter is relatively close to the desired halo orbit, the overall change in attitude states is significant as compared to focusing on a distant star, for example, making the desired zero angular velocity approximation error

significant enough to reduce the precision of the controller. While adding a nonzero desired angular velocity to the controller is straightforward, quantifying the desired angular velocity becomes complicated due to the complex geometry of the halo orbit. Defining this geometry and improving the attitude controller is thus a topic for future studies.

It was found that as the virtual structure increased in size, such that the separation from the individual spacecraft nodes to the central node increased, the PFP thrusters began reaching their limitation in providing sufficient control authority for the formation. While the PFP thrusters were able to maintain the virtual structure formation at separation distances of up to 500 meters from the central node, meeting the design specifications of the Stellar Imager mission, the PFP thrusters could not maintain the formation at a one kilometer separation. This is related to the natural motion of the halo orbit in the CR3BP, where as the initial deviation from the reference orbit increases, the separation rapidly diverges as the orbit is propagated due to the chaotic nature of halo orbits and the instability of libration points.

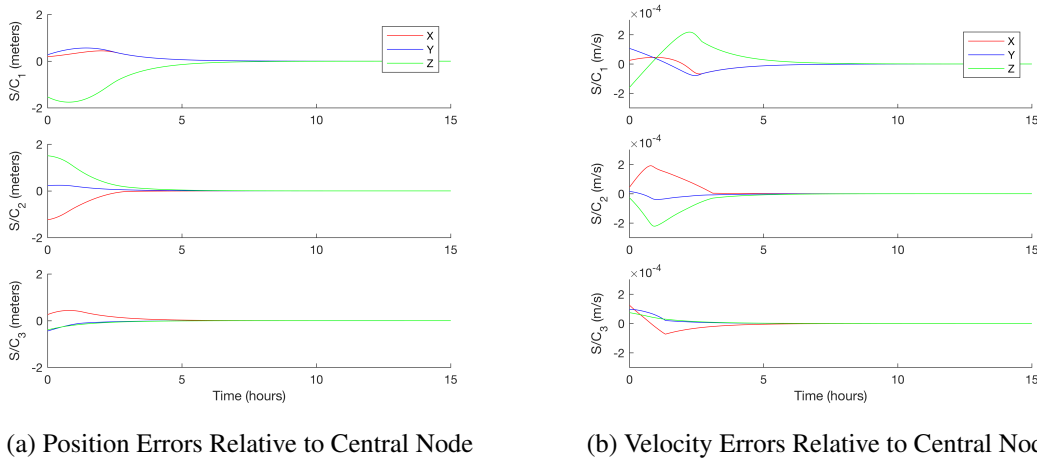


Figure 7: The performance of the translational controller using the PFP thrusters closely resembles the results from the Case 1 study.

CONCLUSIONS AND FUTURE WORK

This study demonstrated the feasibility of using plasmonic force thrusters for a range of advanced mission concepts requiring swarm formations in a deep space environment. While the thrusters had some difficulty in tracking reference trajectories that greatly differed from the natural motion of bodies in the CR3BP, it was found that through refinement of such reference trajectories along with tuning controller gains it was possible to provide some level of formation control. In all three case studies, it was found that attitude could be successfully controlled in both regulation and tracking cases. The attitude tracking case does require further work, however, in better defining the nominal desired angular velocities to improve the controller performance, and is the focus of future work.

It was found that as error levels were lowered into the micrometers range, the simulation encountered numerical limitations of the computer’s operating system. This is related to the manner in which the dynamics are defined in the CR3BP, where the origin of the reference frame is defined at the barycenter of the system of interest. When a halo orbit is the desired reference trajectory,

and errors are defined as deviations from this trajectory, then the measurable precision of the error along the \hat{y} and \hat{z} axes are significantly higher than that along the \hat{x} axis. This is because while the location of any point along the halo orbit is only on the order of hundreds of thousands of kilometers from the reference frame along the \hat{y} and \hat{z} axes, it is on the order of tens of millions of kilometers along the \hat{x} axis. As such, the ability to measure the error along the \hat{x} axis becomes limited in this formulation. To mitigate this, it is advisable to rewrite the system dynamics and reference trajectories in terms of a reference frame where the origin is located at the respective libration point. In this formulation, the position coordinates along the halo orbit would all be of the same order of magnitude along all axes. This formulation will be studied in future work.

While the nonlinear control techniques (along with the robust-adaptive components) were shown to work well in the CR3BP where SRP perturbations were present but unaccounted for, the performance is not guaranteed when moving to higher fidelity models. For example, it is possible to use the elliptical restricted three-body problem (ER3BP), where the eccentricity of Earth's orbit is no longer zero. Similarly, it is also possible to consider additional third-body perturbations such as Jupiter and Saturn. By moving to higher fidelity models such as the ER3BP or an n-body ephemeris model, the fidelity of this study can be further improved and will be a topic of future work.

Along with improving the fidelity and numerical abilities of the simulation, it is also important to continue the refinement of the controller design. As further disturbances are modeled, additional robust-adaptive control elements can be added. Similarly, scheduled gains can be incorporated into the controller to give improved performance of the controller in different error bounds. Such scheduled gains would allow for steady reduction of large deviations from the reference trajectory, such as large injection errors, and then to switch to more refined gains that would maintain a low error about the reference trajectory. The addition of an integrator component to the controller could also further reduce steady state errors, though mitigation methods for integrator windup would need to be considered. Such improvements to the controller will lead to overall improved performance such that the desired performance metrics of advanced mission concepts could be met.

Plasmonic force propulsion offers a unique and exciting technological advancement in the field of micropropulsion for the microsatellite architecture. As the technology is developed, the capabilities and limitations of the thruster will be better defined and the application towards advanced mission concepts requiring swarm formations in a deep space environment can be further established.

REFERENCES

- [1] "Proposed Missions - Terrestrial Planet Finder," www2.jpl.nasa.gov/missions/proposed/tpf.html. Accessed: 2018-07-19.
- [2] "Darwin Overview," http://www.esa.int/Our_Activities/Space_Science/Darwin_overview. Accessed: 2018-07-19.
- [3] "The MAXIM Mission," <https://www.elisascience.org/articles/elisa-mission/mission-concept>. Accessed: 2018-07-19.
- [4] "LISA: Mission Concept," <https://www.elisascience.org/articles/elisa-mission/mission-concept>. Accessed: 2018-07-19.
- [5] K. G. Carpenter, C. J. Schrijver, and M. Karovska, "SI - The Stellar Imager," AIAA Summary Paper, <https://hires.gsfc.nasa.gov/si/documents.html>, 2005.
- [6] "MAXIM Pathfinder," bhi.gsfc.nasa.gov/docs/pathfinder/pathfinder.html. Accessed: 2018-07-19.
- [7] "LISA Pathfinder: Results Show LISA Pathfinder Exceeds Expectations," <https://www.elisascience.org/articles/lisa-pathfinder/results-show-lisa-pathfinder-exceeds-expectations>. Accessed: 2017-04-23.
- [8] "LISA Pathfinder: Testing Key Technologies," <https://www.elisascience.org/articles/lisa-pathfinder/lpf-technology>. Accessed: 2017-04-23.

- [9] “JPL: NASA Microthrusters Achieve Success on ESA’s LISA Pathfinder,” <https://www.jpl.nasa.gov/news/news.php?feature=6676>. Accessed: 2017-04-23.
- [10] B. G. Marchand and K. C. Howell, “Control Strategies for Formation Flight in the Vicinity of the Libration Points,” *Journal of Guidance, Control, and Dynamics*, Vol. 28, No. 6, 2005, pp. 1210–1219.
- [11] M. Leomanni, A. Garulli, A. Giannitrapani, and F. Scortecchi, “Precise Attitude Control of All-Electric GEO Spacecraft Using Xenon Microthrusters,” 33rd International Electric Propulsion Conference, Washington, D.C., October 2013.
- [12] J. Asakawa, H. Koizumi, K. Nishii, N. Takeda, R. Funase, and K. Komurasaki, “Development of the Water Resistojet Propulsion System for Deep Space Exploration by the CubeSat: EQUULEUS,” Small-Sat Conference, Logan Utah, August 2017.
- [13] E. Agasid, R. Hunter, C. Baker, J. Marmie, D. Foreman, J. Hanson, and M. Hill, “NASAs Pathfinder Technology Demonstrator,” SmallSat Conference, Logan Utah, August 2017.
- [14] J. L. Rovey, P. D. Friz, C. Hu, M. S. Glascock, and X. Yang, “Plasmonic Force Space Propulsion,” *Journal of Spacecraft and Rockets*, Vol. 52, 2015, pp. 1163–1168.
- [15] J. L. Rovey, X. Yang, P. D. Friz, C. Hu, and M. S. Glascock, “Plasmonic Force Propulsion Revolutionizes Nano/Picosatellite Capability,” NASA Innovative Advanced Concepts Phase I Final Report, May 2014.
- [16] P. Galchenko and H. J. Pernicka, “Precision Formation Flying and Spacecraft Pointing Using Plasmonic Force Propulsion,” 2017 AAS/AIAA Astrodynamics Specialist Conference, Stevenson, WA, August 2017.
- [17] M. Xin, S. N. Balakrishnan, and H. J. Pernicka, “Multiple Spacecraft Formation Control with θ -D Method,” *IET Control Theory & Applications*, Vol. 1, No. 2, 2007, pp. 485–493.
- [18] M. Xin, S. N. Balakrishnan, and H. J. Pernicka, “Position and Attitude Control of Deep-Space Spacecraft Formation Flying Via Virtual Structure and θ -D Technique,” *Journal of Dynamic Systems, Measurement, and Control*, Vol. 129, No. 5, 2007, pp. 689–698.
- [19] P. Li, P. Cui, and H. Cui, “An Improved Nonlinear Control Strategy for Deep Space Formation Flying Spacecraft,” *Acta Mechanica Sinica*, Vol. 25, No. 6, 2009, pp. 847–856.
- [20] M. Xu, N. Zhou, and J. Wang, “Robust Adaptive Strategy for Stationkeeping of Halo Orbit,” *Proceedings of the 2012 24th Chinese Control and Decision Conference, CCDC 2012*, 2012, pp. 3086–3091.
- [21] M. S. De Queiroz, V. Kapila, and Q. Yan, “Adaptive Nonlinear Control of Multiple Spacecraft Formation Flying,” *Journal of Guidance, Control, and Dynamics*, Vol. 23, No. 3, 2000, pp. 385–390.
- [22] P. Gurfil, M. Idan, and N. Kasdin, “Neurocontrol of Spacecraft Formation Flying in the Elliptic Restricted Three-Body Problem,” *AIAA Guidance, Navigation, and Control Conference and Exhibit*, No. August, 2002, pp. 1–11.
- [23] R. Qi, S. Xu, and M. Xu, “Impulsive Control for Formation Flight About Libration Points,” *Journal of Guidance, Control, and Dynamics*, Vol. 35, No. 2, 2012, pp. 484–496.
- [24] D. A. Vallado, *Fundamentals of Astrodynamics and Applications*. Microcosm Press, Fourth Edition, 2013.
- [25] F. L. Markley and J. L. Crassidis, *Fundamentals of Spacecraft Attitude Determination and Control*. Springer, First Edition, 2014.
- [26] H. K. Kahlil, *Nonlinear Control*. Pearson, First Edition, 2015.
- [27] H. Leeghim, Y. Choi, and H. Bang, “Adaptive Attitude Control of Spacecraft Using Neural Networks,” *Acta Astronautica*, Vol. 64, No. 7, 2009, pp. 778 – 786.